Study of Backgrounds in CANDLES to Search for Double Beta Decays of ^{48}Ca

Hidekazu Kakubata

Dissertation in Physics

Graduate School of Science,
Osaka University

August 2015

Abstract

We perform the CANDLES experiment to search for neutrinoless double beta decay ($0\nu\beta\beta$) of ^{48}Ca. Currently, the CANDLES III(U.G.) detector is running. The purpose of this study is to show origins of backgrounds in the energy region around $Q_{\beta\beta}$ (4.27 MeV) and to estimate the amount of backgrounds. In $Q_{\beta\beta}$ region, Th-chain backgrounds are expected and can be excluded by analysis. However, backgrounds that were out of expectation at the $Q_{\beta\beta}$ region existed in the observed spectra. The current sensitivity of CANDLES for $0\nu\beta\beta$ half-life is $> 0.8 \times 10^{22}$ yr. In order to improve the sensitivity, backgrounds should be reduced. Therefore, we studied the origin of backgrounds. For this investigation, experimental runs using ^{252}Cf neutron source were performed and we found that these backgrounds are mainly caused by γ-rays from (n,γ) reactions in materials around the detector. This means that additional outer shields against γ-rays and neutrons are necessary. We aim to reduce backgrounds of less than 1 event per year at $Q_{\beta\beta}$ region with additional shielding. By achieving ultra low background condition, half-life sensitivity of the detector is expected to be $\sim 10^{24}$ yr, which will be the most stringent experimental limit for $0\nu\beta\beta$ of ^{48}Ca.

Contents

Chapter 1

Double Beta Decay

1.1 Neutrino properties

Neutrino is one of the most important particle in subatomic physics [1]. Especially, the greatest interest about neutrino is whether it is Majorana particle or Dirac particle.

The Standard Model (SM) of particle physics assumed that neutrinos are massless. In fact, neutrino mass have not been measured directly experimentally. On the contrary, the discovery of neutrino oscillations (solar, atmospheric, reactor and accelarator) provided us that neutrinos should be massive [2]. These results suggest that each flavor of neutrinos ν_e, ν_μ, ν_τ has its own mass $m_{\nu_e}, m_{\nu_\mu}, m_{\nu_\tau}$, and these flavor eigenstates are mixtures of different three mass eigenstates ν_1, ν_2, ν_3,

$$\begin{pmatrix} m_{\nu_e} \\ m_{\nu_\mu} \\ m_{\nu_\tau} \end{pmatrix} = U_{\mathrm{MNS}} \begin{pmatrix} m_1 \\ m_2 \\ m_3 \end{pmatrix} = \begin{pmatrix} U_{e1} & U_{e2} & U_{e3} \\ U_{\mu 1} & U_{\mu 2} & U_{\mu 3} \\ U_{\tau 1} & U_{\tau 2} & U_{\tau 3} \end{pmatrix} \begin{pmatrix} m_1 \\ m_2 \\ m_3 \end{pmatrix}$$

$$= \begin{pmatrix} c_{12}c_{13} & s_{12}c_{13} & s_{13}e^{-i\delta} \\ -s_{12}c_{23} - c_{12}s_{23}s_{13}e^{i\delta} & c_{12}c_{23} - s_{12}s_{23}s_{13}e^{i\delta} & s_{23}c_{13} \\ s_{12}s_{23} - c_{12}c_{23}s_{13}e^{i\delta} & c_{12}s_{23} - s_{12}c_{23}s_{13}e^{i\delta} & c_{23}c_{13} \end{pmatrix} \begin{pmatrix} m_1 \\ m_2 \\ m_3 \end{pmatrix}, \qquad (1.1)$$

where U_{MNS} is the lepton mixing matrix, called MNS(Maki-Nakagawa-Sakata)-matrix, m_i $(i = 1,2,3)$ is mass eigenvalue of ν_i, δ is the phase and $s(c)_{ij} = \sin(\cos)\theta_{ij}$ with mixing angles $\theta_{12}, \theta_{23}, \theta_{13}$. Observed parameters are listed in Table 1.1.

Table 1.1: Neutrino oscillation parameters summary [2].

parameter		best fit
Δm^2_{21} [10^{-5} eV^2]		$7.62^{+0.19}_{-0.19}$
$\lvert\Delta m^2_{31}\rvert$ [10^{-5} eV^2]	(normal)	$2.55^{+0.06}_{-0.09}$
	(inverted)	$2.43^{+0.07}_{-0.06}$
$\sin^2\theta_{12}$		$0.320^{+0.016}_{-0.017}$
$\sin^2\theta_{23}$	(normal)	$0.613^{+0.022}_{-0.040}$
	(inverted)	$0.600^{+0.026}_{-0.031}$
$\sin^2\theta_{13}$	(normal)	$0.0246^{+0.0029}_{-0.028}$
	(inverted)	$0.0250^{+0.0026}_{-0.027}$
δ	(normal)	0.80π
	(inverted)	-0.03π

Although the evidences of non-zero neutrino mass are found, absolute mass values have not been measured yet. Furthermore, oscillation experiments have not shown the neutrino mass hierarchy completely yet. According to the delta mass squares (Δm^2_{21} and $|\Delta m^2_{31}|$[1]) obtained from oscillation experiments, normal ($m_3 >> m_1, m_2$) and inverted ($m_1, m_2 >> m_3$) hierarchy candidates remain (Fig. 1.1). The other possibility is that these masses are degenerated ($m_1 \sim m_2 \sim m_3 >> \Delta m$).

Neutrino masses are expected to be considerably smaller than other leptons (e.g. electron mass $m_e = 511$ keV). We need a mechanism that can explain reasonably such small masses. Moreover, there is another problem that observed neutrinos (anti-neutrinos) are only left-handed (right-handed). This fact suggests that there are essential differences in left-handed neutrino and right-handed one, and can be explained by introducing Majorana mass. In the case of Majorana neutrino, a mass of left-handed neutrino (m_L) can be different from one of right-handed(m_R). A Lagrangian of Majorana neutrino shows how m_L

[1]Only an absolute value of Δm^2_{31} is established.

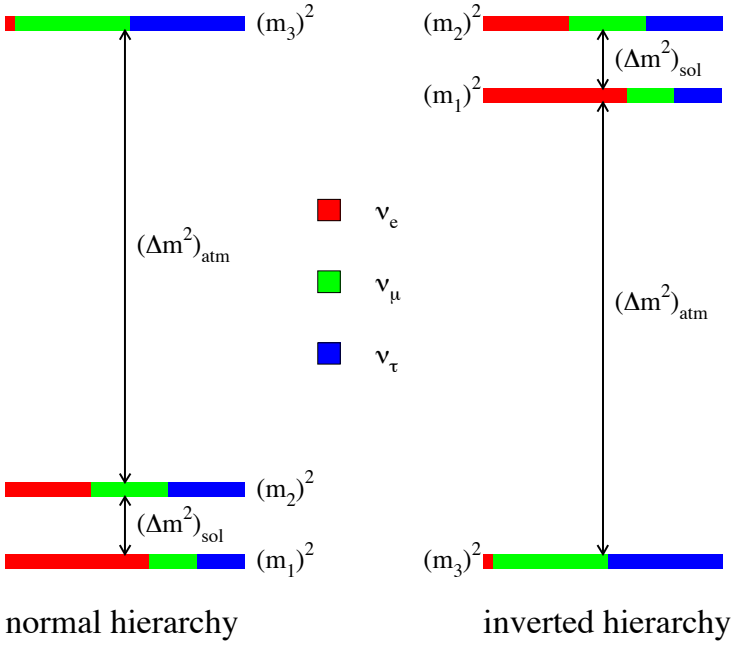

Figure 1.1: Illustration of the current state of neutrino mass and mixing measurements [4]. The colors in states represent the flavor eigenstates; red is ν_e, green is ν_μ and blue is ν_τ. This figure shows two versions of the hierarchy, normal and inverted.

and m_R can be different (1.2) [1].

$$L_{\nu\text{mass}} = -m_D\{\bar{\nu}_R\nu_L + \bar{\nu}_L^c\nu_R^c\} - \frac{m_L}{2}\{\bar{\nu}_L^c\nu_L + \bar{\nu}_L\nu_L^c\} - \frac{m_R}{2}\{\bar{\nu}_R^c\nu_R + \bar{\nu}_R\nu_R^c\} \quad (1.2)$$

where m_D in this expression is a Dirac mass, $\nu_{L,R}$ are wavefunctions of left-handed and right-handed neutrinos, and an index c is a charge conjugation, a bar($\bar{}$) is an index of antiparticle. Here first term is the Dirac mass term and the others are the Majorana mass terms. A Lagrangian of an ordinary Dirac particle has only the Dirac term. The Dirac mass term is complicated in the term involving left-handed and right-handed function. As a result, two-handed particles have same mass.

On the other hand, in Majorana case, a Lagrangian has two mass eigenvalues m_L, m_R which make left(right)-handed term independently each other. This makes left-handed and right-handed particles to have their own masses ($m_L \neq m_R$). From a form of this Lagrangian, a relation between three mass eigenvalues

is explained as

$$m_L = \frac{m_D^2}{m_R}. \tag{1.3}$$

This relation is called the seesaw mechanism [5]. With m_D of the order of MeV-GeV,

$$m_L m_R \approx 10^{12\sim18}\ \mathrm{eV}^2. \tag{1.4}$$

Assuming that m_R is a large value exceeding an observation limit, very small m_L value can be explained by this mechanism. This explain a problem of a sub-eV mass value of left-handed neutrino. As stated above, various studies make a expectation that neutrino is Majorana fermion.

1.2 Double Beta Decay

Observation of neutrinoless double beta decay provides important informations about neutrino property. Double beta decay ($\beta\beta$) is a rare kind of radioactive decay which happens in even-even isotopes. Weizäcker mass formula [6] shows isobar's (mass number A = constant) description as

$$m(A,Z) \propto \alpha Z + \beta Z^2 + \delta_P + \text{constant} \tag{1.5}$$

where Z is an atomic number, α, β are arbitrary coefficients, δ_P is called pairing energy and parametrized as

$$\delta_P = \begin{cases} -a_P A^{1/2} & \text{even-even nuclei} \\ 0 & \text{even-odd, odd-even nuclei} \\ +a_P A^{1/2} & \text{odd-odd nuclei.} \end{cases} \tag{1.6}$$

Odd A makes zero δ_P that results mass function in one parabola. If A is an even number, this function is separated into two parabolas by $2\delta_P$ (Fig. 1.2). For even-even nuclei, single beta decay is forbidden by energy conservation, and consequently $\beta\beta$ decay can be observed.

The types of decays are below (and Fig. 1.3),

$$(A,Z) \rightarrow (A,Z+2) + 2e^- + 2\bar{\nu}_e\ (2\nu\beta\beta), \tag{1.7}$$

$$(A,Z) \rightarrow (A,Z+2) + 2e^-(0\nu\beta\beta). \tag{1.8}$$

Two neutrino double beta decay $2\nu\beta\beta$ conserves lepton number and is allowed within the SM, regardless of whether neutrino is the Majorana particle or not. This decay has been observed for several isotopes.

On the other hand, neutrinoless double beta decay $0\nu\beta\beta$ violates lepton number and is forbidden in the SM. In $0\nu\beta\beta$ mechanism, an antineutrino, which is emitted when a neutron decays, is absorbed by another neutron in the same nucleus as a right-handed neutrino (See Fig. 1.3). This decay occurs only when a neutrino is a Majorana fermion. The search for $0\nu\beta\beta$ is the only experimental way to determine whether a neutrino is a Majorana fermion or a Dirac fermion.

Moreover, $0\nu\beta\beta$ observation provides information about neutrino mass. Decay rate of $0\nu\beta\beta$ ($(T^{0\nu}_{1/2})^{-1}$) is explained as a function related with effective Majorana mass $\langle m_{\beta\beta}\rangle$ [8],

$$(T^{0\nu}_{1/2})^{-1} = G^{0\nu}(Q_{\beta\beta}, Z)|M^{0\nu}|^2\langle m_{\beta\beta}\rangle^2 \tag{1.9}$$

where $G^{0\nu}(Q_{\beta\beta}, Z)$ is the function of Q-value and the quantity of protons (or atomic number), called the phase space factor and $|M^{0\nu}|$ is the nuclear matrix element (NME) that varies with $\beta\beta$ isotope, and $\langle m_{\beta\beta}\rangle$ is effective Majorana neutrino mass which is given in equation below,

$$|\langle m_{\beta\beta}\rangle| = |\sum_i m_i U^2_{ei}| \tag{1.10}$$

where m_i and U_{ei} ($i = 1, 2, 3$) are same expression as equation (1.1) [8]. Effective Majorana mass imposes restrictions on neutrino mass and hierarchy (Fig. 1.4).

1.3 Experiments for Double Beta Decays

As described above, $0\nu\beta\beta$ observation is essential to neutrino physics, and many experiments have been performed with several isotopes(Table 1.2). Recent experiments mainly measure the sum energy of two electrons emitted by $\beta\beta$ decay. In $2\nu\beta\beta$, the sum kinetic energy of two electrons forms continuous spectrum because neutrinos also carry parts of the kinetic energy. In $0\nu\beta\beta$, two electrons carry the full kinetic energy which makes that the sum kinetic energy of electrons forms a single peak at $Q_{\beta\beta}$ (Fig. 1.6). For this reason, measurement of the sum energy of electrons is the key to observe $0\nu\beta\beta$ events.

Observation systems are devided into two types according to setup of $\beta\beta$ emitter (source) and emission detector (target).

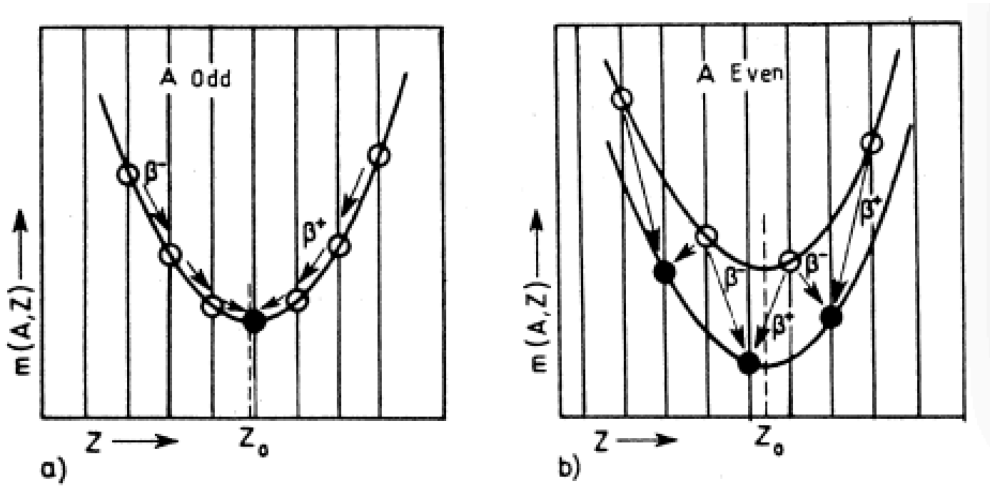

Figure 1.2: Dependence of energy on Z for nuclei with the same mass number A. (Left) nuclei with odd mass number A. (Right) nuclei with even mass number A [1].

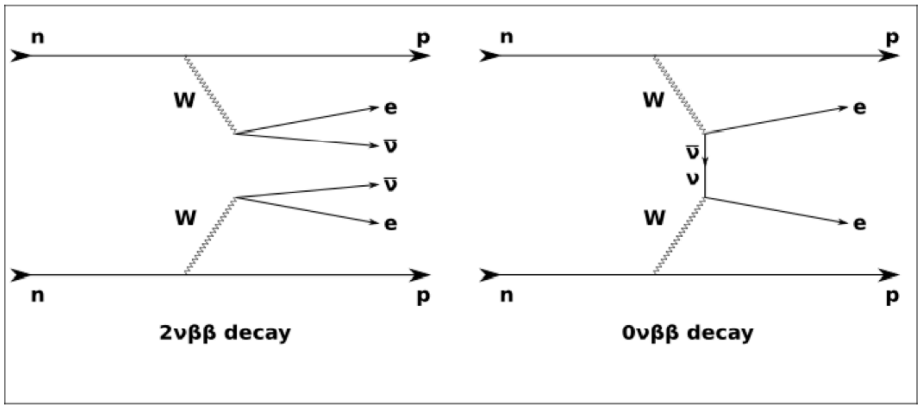

Figure 1.3: Diagrams of double beta decays.

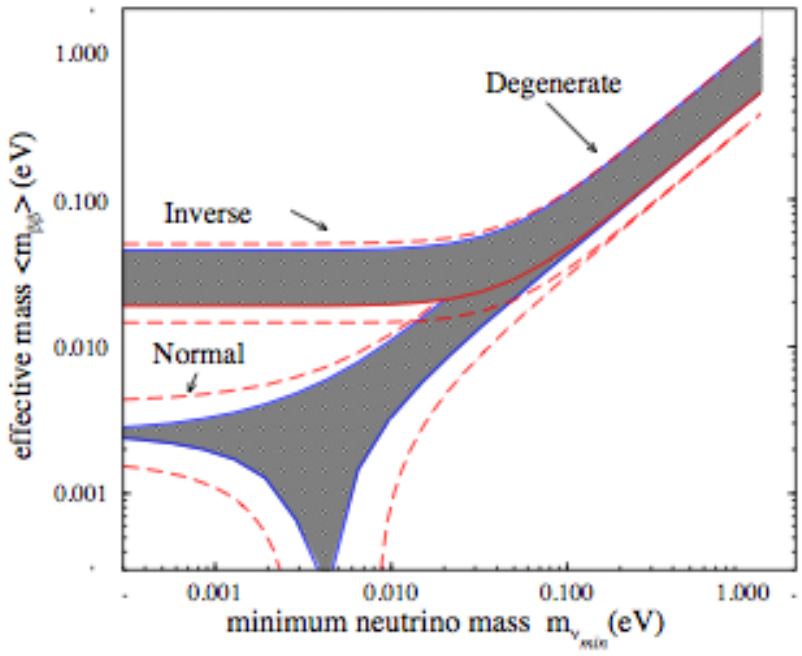

Figure 1.4: The parameter space for $m_{\beta\beta}$ as a function of the minimum neutrino mass. The vertical axis means effective Majorana mass estimated by $0\nu\beta\beta$ search and the horizontal means minimum neutrino mass predicted from candidates of mass hierarchy. The shaded area is for central values for neutrino mixing parameters and the dashed lines indicate 1σ errors on neutrino mixing parameters [7].

Table 1.2: A list of $\beta\beta$ isotopes with high Q-value and experiments [8].

isotope	$G^{0\nu}$ (yr^{-1})	$Q_{\beta\beta}$ (keV)	nat. ab. (%)	$T^{2\nu}_{1/2}$ (y)	Experiments
^{48}Ca	6.3×10^{-14}	4274	0.187	0.44×10^{20}	ELEGANT VI, CANDLES
^{76}Ge	0.63×10^{-14}	2039	7.8	15×10^{20}	GERDA, MAJORANA
^{82}Se	2.7×10^{-14}	2996	9.2	0.92×10^{20}	SuperNEMO, LUCIFER
^{100}Mo	4.4×10^{-14}	3035	9.6	0.07×10^{20}	NEMO-3, MOON, AMoRe
^{116}Cd	4.6×10^{-14}	2809	7.6	0.29×10^{20}	COBRA
^{130}Te	4.1×10^{-14}	2530	34.5	9.1×10^{20}	CUORE, SNO+
^{136}Xe	4.3×10^{-14}	2458	8.9	21×10^{20}	KamLAND-Zen, EXO, NEXT
^{150}Nd	19.2×10^{-14}	3367	5.6	0.08×10^{20}	SNO+, DCBA/MTD

- The passive, "source≠target" or tracking method is the detector that the source and counter are separated. Merits of the method are good reduction for background and ability of observation with several isotopes in one detector system.
- The active, "source=target" or calorimatoric method is the type that the source and detector are identical. This method has advantages of easy increasing in size and high detection efficiency of β decay.

Backgrounds

Since $0\nu\beta\beta$ decays are considerably rare events whose $T^{0\nu}_{1/2}$ is expected to be larger than 10^{26}yr, background reduction is one of the most important measures. For long measuring time, if background is negligible,

$$\langle m_{\beta\beta}\rangle \propto \Big[\frac{W}{f x \epsilon G^{0\nu}|M^{0\nu}|^2}\Big]^{1/2}\frac{1}{\sqrt{MT}}, \tag{1.11}$$

yet if backgrounds exist,

$$\langle m_{\beta\beta}\rangle \propto \Big[\frac{W}{f x \epsilon G^{0\nu}|M^{0\nu}|^2}\Big]^{1/2}\Big[\frac{b\Delta E}{MT}\Big]^{1/4}, \tag{1.12}$$

where W is the weight of the source material, f is the isotopical abundance, x is the proportion of $\beta\beta$ candidates atoms in material, ϵ is the detector efficiency, M is the mass of isotope, T is the live time of the experiment, b is the number of background counts/kg/yrs/keV, and ΔE is the energy window for $0\nu\beta\beta$ search. These equations shows that mass sensitivity depends on the existence of backgrounds drastically.

Possible backgrounds are as follows.

1. Cosmic muons

   Cosmic ray interactions in the atmosphere produce secondary particles like muons, which become backgrounds of electron detection. To a large extent, cosmic muons can be reduced in underground observatories. For example, underground situation of Kamioka Observatory (1km in depth) reduces muon intensity by 1/200,000. Vertical muon flux in some representative underground laboratories is shown in Fig. 1.3.

2. Natural radiation in U,Th chain

   The highest end point of environmental "single pulse" γ-ray energy is 2.6 MeV which ^{208}Tl emits. Therefore, the target $\beta\beta$ isotope should have Q-value which is higher than 2.6 MeV. Table 1.2 shows $\beta\beta$ isotopes of high $Q_{\beta\beta}$ and experiment using these isotopes. On the other hand, other events can reach the energy region above 4 MeV (for example, double pulse events of Bi-Po serial decays and $\beta + \gamma$ events of ^{208}Tl decays). Those backgrounds have to be reduced with material purification and analytical method on experiments.

3. $2\nu\beta\beta$ event (Fig. 1.6)

   $0\nu\beta\beta$ events have a monochromatic energy of $Q_{\beta\beta}$ that forms a peak and $2\nu\beta\beta$ events make a continous spectrum below $Q_{\beta\beta}$. To separate these types of $\beta\beta$ events on the spectral shapes, good energy resolution is necessary.

1.3.1 Experiments

Although some $\beta\beta$ experiments could measure $2\nu\beta\beta$ half-lives, $0\nu\beta\beta$ had not been observed yet. This section shows some projects reporting results with stringent limits for $\beta\beta$ of ^{136}Xe, ^{76}Ge and ^{48}Ca.

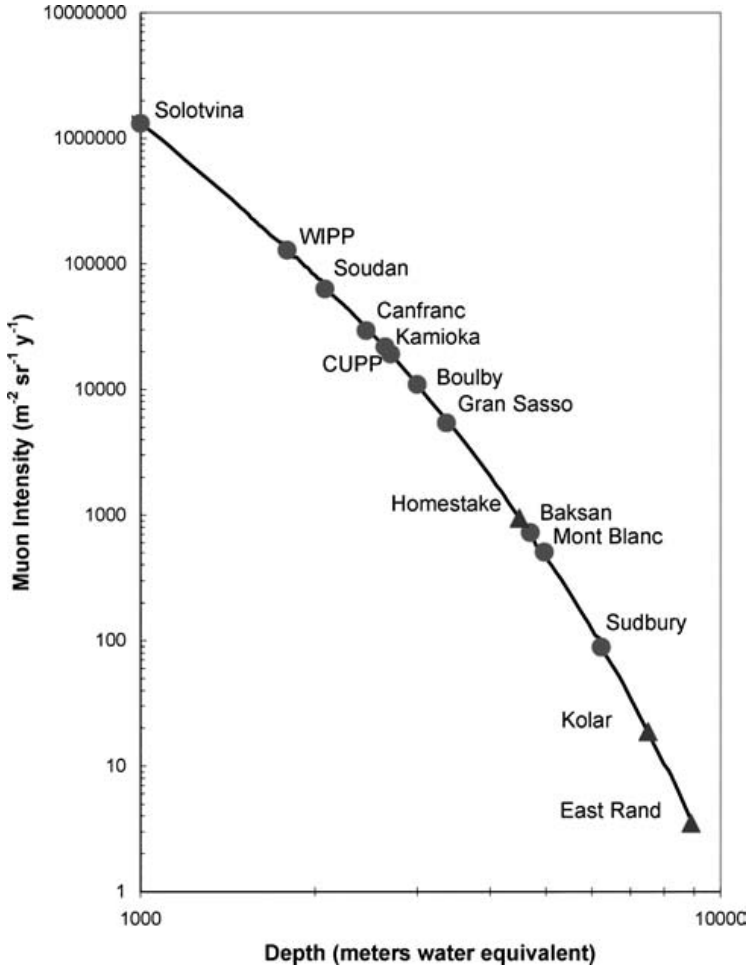

Figure 1.5: Vertical muon flux as a function of depth, normalized to meter water equivalent(m.w.e.) [9].

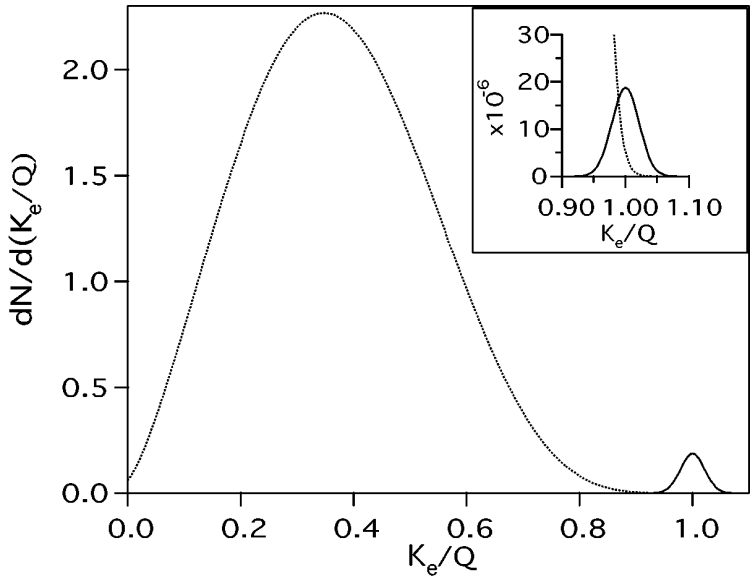

Figure 1.6: Spectral shapes of observable sum energy spectra of emitted electrons in $\beta\beta$ decays. The $2\nu\beta\beta$ spectrum (dotted) is normalized to 1. The $0\nu\beta\beta$ spectrum (solid) is normalized to 10^{-2} (10^{-6} in the inset, which is similar to experimental ratio). All spectra are convolved with an energy resolution of 5 %. [7].

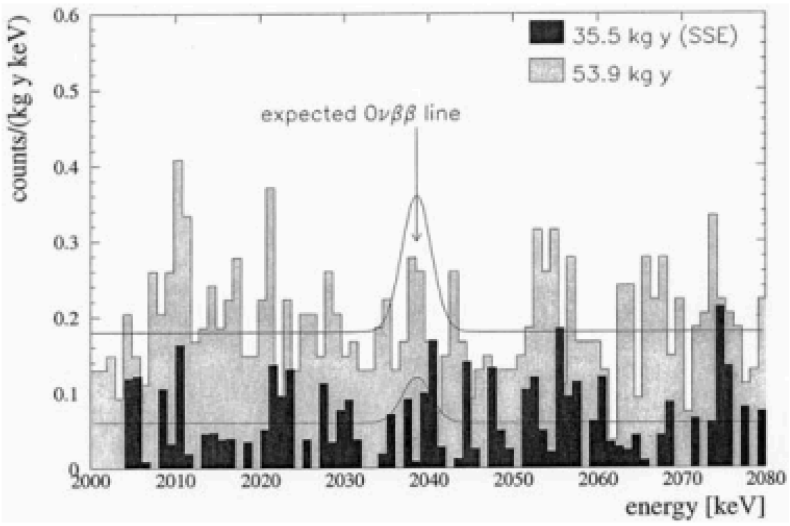

Figure 1.7: Observed spectrum around the expected $0\nu\beta\beta$ peak of the Heidelberg-Moscow collaboration. [10]

The Heidelberg-Moscow Experiment [10]

The experiment in the Gran Sasso Laboratory used 11kg of Ge enriched to about 86 % in ^{76}Ge in the form of five High Purity Ge (HPGe) active detectors. With the exposure of 53.9 kg $\cdot$ yr, the evidence for $0\nu\beta\beta$ decays was reported by a few members of the collaboration and this is still a matter of controversy (well known as KKDC claim. See Fig. 1.7). If it is true, the $0\nu\beta\beta$ half life and the resulting mass are

$$T^{0\nu}_{1/2}(^{76}\mathrm{Ge}) \sim 1.9 \times 10^{25}\ \mathrm{yr}\ (90\ \%\ \mathrm{C.L.}). \tag{1.13}$$

$$\langle m_{\beta\beta} \rangle \sim 0.35\ \mathrm{eV}. \tag{1.14}$$

The method of analysis had been discussed, and to examine this claim is the first goal of the other groups.

GERDA [11]

A first phase of the GERDA experiment at Gran Sasso used the germanium (^{76}Ge) detectors of Heidelberg-Moscow and IGEX (total mass 13kg). The detectors are supported by a minimal amount of material with low radioactivity in a 4mϕ cryostat filled with liquid argon as active shield and cooling material.

GERDA collected the data between November 2011 and May 2013 as first phase with total exposure of 21.6 kg $\cdot$ yr. Then a lower limit for $0\nu\beta\beta$ of ^{76}Ge is derived as

$$T^{0\nu}_{1/2}(^{76}\mathrm{Ge}) > 3.0 \times 10^{25}\ \mathrm{yr}\ (90\ \%\ \mathrm{C.L.}), \tag{1.15}$$

which is one of the most stringent limits for $0\nu\beta\beta$. GERDA started a second phase with additional 18kg of ^{76}Ge detectors in 2013.

KamLAND-Zen [12]

The KamLAND-Zen experiment is performed at Kamioka Underground Observatry. A balloon of 1.54 m radius made out of 25 μm thick nylon is inserted into the KamLAND detector and filled with xenon loaded scintillator ($\sim$ 290 kg ^{136}Xe). The project started collecting data in 2011. The results using data of 62 kg $\cdot$ yr exposure are below,

$$T^{2\nu}_{1/2}(^{136}\mathrm{Xe}) = 2.38 \pm 0.14 \times 10^{21}\ \mathrm{yr} \tag{1.16}$$

$$T^{0\nu}_{1/2}(^{136}\mathrm{Xe}) > 1.9 \times 10^{25}\ \mathrm{yr}\ (90\ \%\ \mathrm{C.L.}). \tag{1.17}$$

Meanwhile, unexpected backgrounds from $^{110\mathrm{m}}$Ag were observed in the Q-value region. Additional 700 kg of Xe with 90 % enrichment and a cleaner balloon are set in the near future. Therefore, KamLAND-Zen will be the first observation with ton scale isotope masses.

EXO(EXO-200) [13]

EXO-200 at Waste Isolation Pilot Plant (WIPP) focuses on ^{136}Xe. The experiment includes a liquid xenon TPC of 40 cm $\phi \times$ 40 cm (175 kg liquid Xe, 100 kg fiducial mass). The group has recently published results on the $2\nu\beta\beta$ half life and limit on the $0\nu\beta\beta$ half life with 32.5 kg $\cdot$ yr exposure as

$$T^{2\nu}_{1/2}(^{136}\mathrm{Xe}) = 2.1 \pm 0.2 \times 10^{21}\ \mathrm{yr} \tag{1.18}$$

$$T^{0\nu}_{1/2}(^{136}\mathrm{Xe}) > 1.6 \times 10^{25}\ \mathrm{yr}\ (90\ \%\ \mathrm{C.L.}). \tag{1.19}$$

This experiment is scheduled to run for 4 more years. In addition, next expansions with multi-ton LXe detectors are planned.

ELEGANT VI and CANDLES [16, 17, 18, 19, 20]

Calcium 48 (^{48}Ca) has the highest $Q_{\beta\beta}$(4.27 MeV) in $\beta\beta$ isotopes (see Fig. 1.8, [14]), but it has the exceedingly small natural abundance (0.187 %) [15]. We performed the ELEGANT experiment, the measurements of $0\nu\beta\beta$ with CaF_2(Eu) scintillators at Oto Cosmo Observatory. The ELEGANT VI detector consists of 23 CaF_2(Eu) crystals with dimensions of 4.5×4.5×4.5 cm^3 as sources (containing 7.7g of ^{48}Ca), CaF_2(pure) bars as light guides, and CsI(Tl) scintillators as active veto (Fig. 1.9). ELEGANT VI with exposures of 4947 kg · day (about 2 years measurement) achieved zero background measurement and obtained the most stringent experimental limit for $0\nu\beta\beta$ of ^{48}Ca,

$$T_{1/2}^{0\nu}(^{48}\mathrm{Ca}) > 5.8 \times 10^{22}\mathrm{yr}\ (90\ \%\mathrm{C.L.}) \tag{1.20}$$

We continues the measurement focused on ^{48}Ca $0\nu\beta\beta$ with the CANDLES experiment. 40 times targets in weight are prepared and impurities of crystals are reduced to less than one order. Details of CANDLES are described in Chapter 2.

Observation of $0\nu\beta\beta$ must be performed with multiple isotopes complementary. The CANDLES experiment is expected to perform an important role in $0\nu\beta\beta$ physics.

1.4 Purpose of the study

Our group have operated the CANDLES experiment. On $0\nu\beta\beta$ experiments, background reduction is important to improve the sensitivity. Expected backgrounds around $Q_{\beta\beta}$ are $\beta + \gamma$ emission from ^{208}Tl (Q_β= 5.0 MeV) and sequential decay of ^{212}Bi-^{212}Po (max visible energy of $\beta + \alpha$ is around 5 MeV). Those events can be discriminated by offline data analysis (See Chapter 3,4). However, in a long-term measurement (97 days as live time), we found the unexpected backgrounds in the high energy region above $Q_{\beta\beta}$ and peak structure is found in 7∼8 MeV. To improve the detector sensitivity, it is necessary to eliminate the origin of backgrounds. The purpose of this study is to identify these unknown backgrounds and to study the method of background reduction.

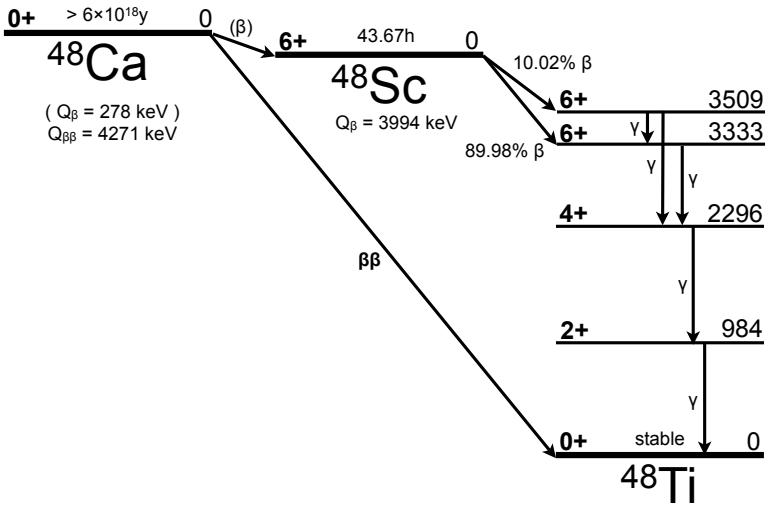

Figure 1.8: Decay Scheme from ^{48}Ca to ^{48}Ti [14]. Single β decay of ^{48} Ca is strongly suppressed by spin.

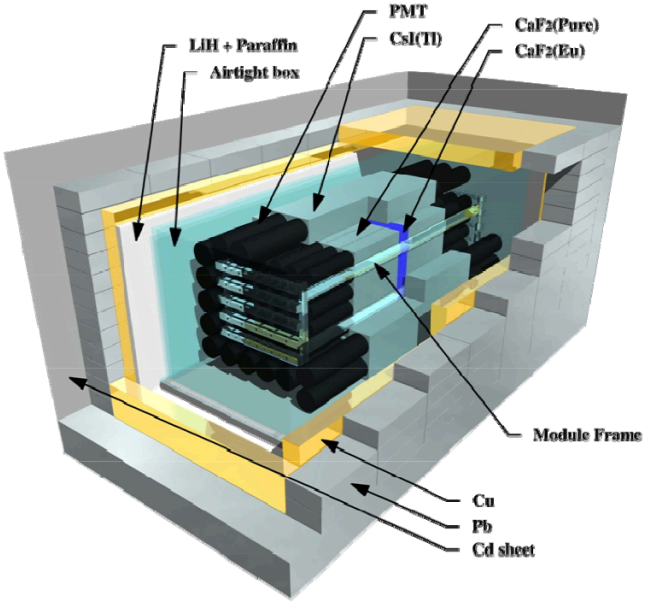

Figure 1.9: A schematic drawing of ELEGANT VI. [16]

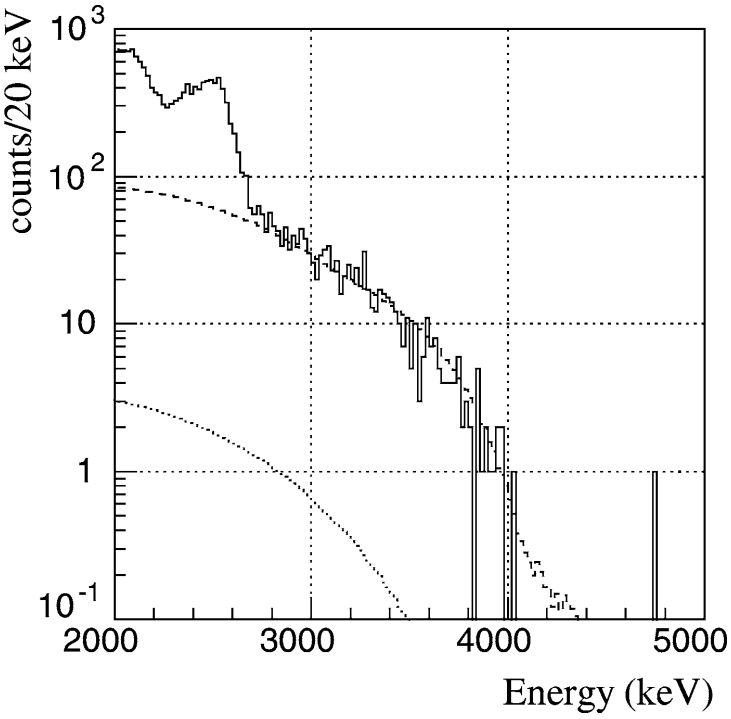

Figure 1.10: A comparison of the experimental data of live time of 232 days in the ELEGANT VI experiment (solid line) with Monte Carlo simulations from the internal radioactives (dashed line) and the $2\nu\beta\beta$ of ^{48}Ca (dotted line) [16]

Chapter 2

The CANDLES Experiment

2.1 ^{48}Ca $\beta\beta$ experiment

About three dozens of $\beta\beta$ isotopes exist, but those which can be examined are limited because high $Q_{\beta\beta}$ are required in order to reduce the natural radioactivity in environment. About a dozen isotopes are studied with $\beta\beta$ physics currently. Table 1.2 shows the typical examined $\beta\beta$ isotopes and their Q-values. The CANDLES Experiment focuses on ^{48}Ca as the target $\beta\beta$ isotope.

A merit of ^{48}Ca is the highest $Q_{\beta\beta}$ value among all the $\beta\beta$ isotopes ($Q_{\beta\beta}$ = 4274 keV), which makes it possible to perform measurement in very low background environment. The highest energy of natural background single γ-ray is 2.6 MeV from ^{208}Tl decay. Therefore, we can search $\beta\beta$ events of ^{48}Ca without natural radiation. In addition, higher $Q_{\beta\beta}$ makes better energy resolution at the energy of $0\nu\beta\beta$, which is necessary to separate $0\nu\beta\beta$ signals from $2\nu\beta\beta$ ones.

On the other hand, ^{48}Ca also has weakness in natural abundance which is extremely small (0.187 %) [15]. ^{48}Ca cannot be enriched with centrifugation method because gas compound of calcium does not exist. To enlarge experimental exposure, new approach for ^{48}Ca enrichment should be developed. Currently, enrichment method by laser excitation and another method using resin-treated crown ether are studied.

2.2 Property of CANDLES

The concept of CANDLES (Fig. 2.1) is a solid large detector with 4π active shielding system. The number of 10cm cubic CaF_2(pure) crystal scintillators are immersed in liquid scintillator (LS) which works as active veto shield. These scintillators are placed in a transparent acrylic tank, and large PMTs, which are installed in pure water, observe scintillation lights from both scintillators and LS simultaneously. $0\nu\beta\beta$ events cause a scintillation light from only each of CaF_2 crystal that the event occurs, not from the other crystals and LS. An external background (γ rays from outer detector and environment, cosmic rays) interacts with LS and crystals, which causes lights from both scintillators. Each decay constant of scintillator is considerably different; that of CaF_2 is 1 μsec and that of LS is about 10 nsec (Fig. 2.2). Therefore, scintillation lights from different materials can be separeted analytically.

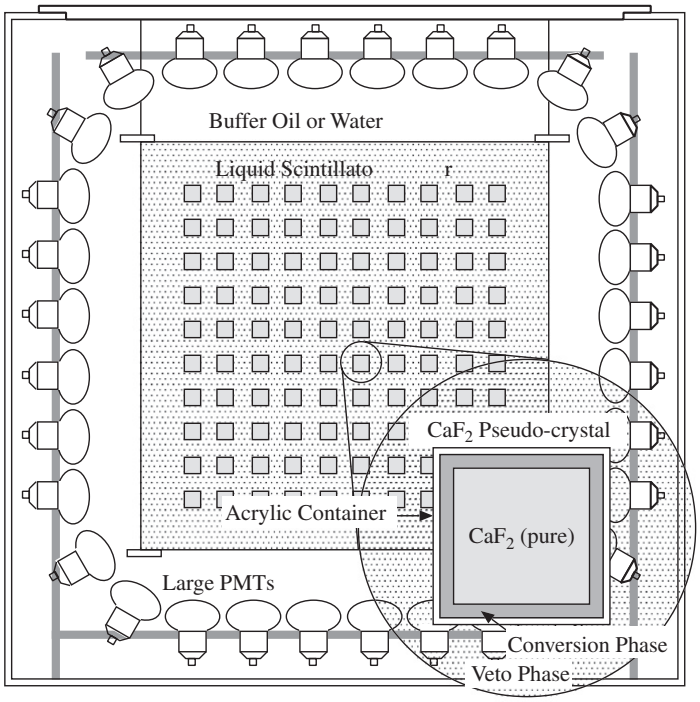

Figure 2.1: A conceptual design of the CANDLES detector and crystal module [19].

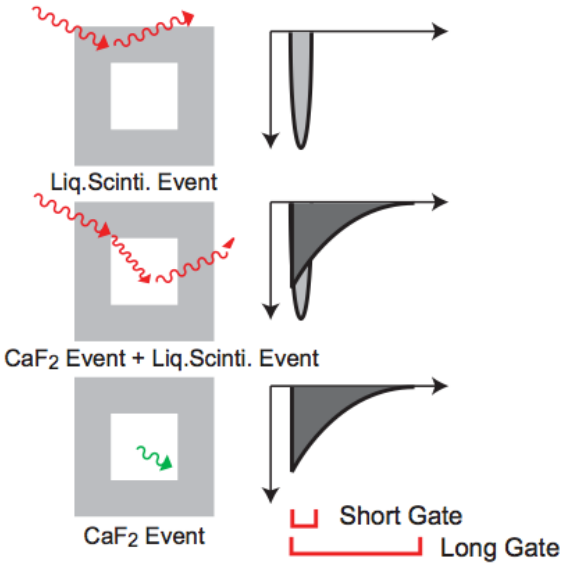

Figure 2.2: Illustration of scintillation pulse waveforms [20]. The CaF_2 signal has long decay constant (1 μs) and the LS signal has short constant (10ns).

CaF_2 crystal module

A CaF_2(pure) scintillator has an advantage of longer attenuation length (10m) than CaF_2(Eu), which is suitable for three-dimensional expansion of detector. On the other hand, it has demerits of lower photon production which is nearly half of CaF_2(Eu) and the UV-region scintillation lights (Fig. 2.3) which are out of sensitive region of PMTs. Light collection with PMT light guides should be composed for the former problem, and both of problems can be solved with wave length shifter(WLS) phase. In the detector design, a large number of CaF_2 crystals in the form of 10 cm cubes are immersed in the LS.

WLS phase

In order to collect more scintillation photons, WLS has to absorb UV-region lights and convert it into visible-region lights. In addition, a refractive index of WLS must be close to that of CaF_2 crystal ($n_{CaF_2} = 1.43$). The thickness is limited as mm order because WLS is dead volume for the LS active veto phase. A kind of paraffin oil (Showa Shell Sekiyu K.K., Paraol) is selected for the solvent of WLS. It does not absorb UV light and has a refractive index which is close to that of crystals. Bis-MSB is selected for the solute, because it

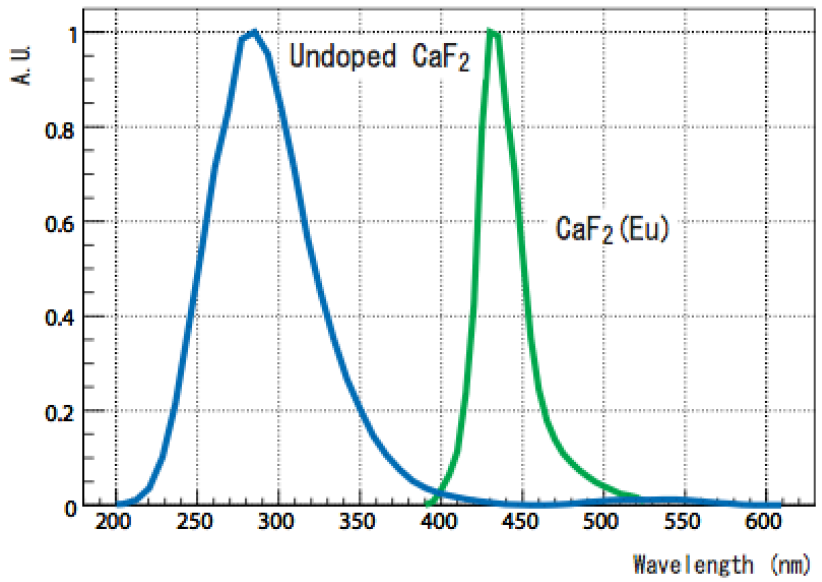

Figure 2.3: Emission wavelength of undoped(pure) CaF_2 (blue) and CaF_2(Eu) (green) taken from [20].

absorbs lights with wevelength around 360nm and converts it to that of 420nm wavelength(Fig. 2.4). Then bis-MSB with paraffin oil is used for WLS in 5mm thickness phase around CaF_2 crystal.

LS as active veto phase

Active veto phase should have similar refractive index to crystal module with WLS phase. Additionally, it is required to have a large light output, high light transparency. Furthermore, a large quantity with reasonable costs is needed. Pseudocumene(PC) is used as solvants because it has large light output and long attenuation length. PC should be diluted in order to avoid dissolving the acryl which is used for materials of CaF_2 module cases and LS vessel. Then paraffin oil is also used as solvant. As solutes of LS, Bis-MSB and PPO are selected.

Table2.1 is the components of WLS and LS used by CANDLES. LS is confined into transparent acrylic vessels.

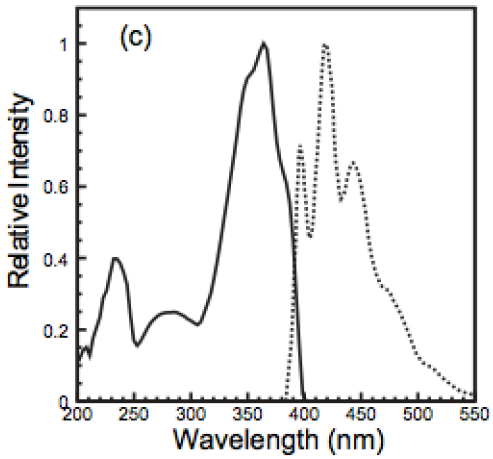

Figure 2.4: Wavelength spectra of Bis-MSB. (solid) absorption lights, (dashed) emmision. This figure is taken from [20].

	WLS phase	LS phase
Solvant	paraffin oil	paraffin oil (80 %) + pseudocumene (20 %)
Solute	bis-MSB(0.1g/l)	bis-MSB(0.1g/l) + PPO(1.0g/l)

Table 2.1: Components of WLS phase and active veto phase which is used as CANDLES's setup

PMTs and passive veto phase

Pure water phase is used as passive shield for environmental neutrons. Large PMTs surrounding the LS tank observe scintillation light from CaF_2 and LS. light pipes are installed in front of PMTs in order to improve their light collection efficiency. PMTs and pipes are fixed on hard stainless steel tank.

2.3 Setup of the CANDLES III(U.G.) Detector

2.3.1 Detector setup

Current setup of the CANDLES experiment (CANDLES III(U.G.), Fig. 2.5) is introduced. The detector is constructed in Kamioka Underground Observatory.

As Introduced Chapter 1.3 (Fig. 1.5), Kamioka Observatory reduces muon intensity to negligible. Some of the other low background experiments are held in Kamioka. [9]

Geometry

The detector is ϕ 3 m $\times$ 4 m stainless steel tank including 96 cubes of CaF_2 crystal (300 kg in total), 2,000 L of LS and 28,000 L of pure water. Crystal modules with 10 cm $\times$ 10 cm $\times$ 10 cm CaF_2 crystals, WLS phase of 5mm in thickness and acrylic cases are positioned at equal intervals of 10cm. These module arrangements are shown in Fig. 2.6. Scintillator tank (ϕ 1.4 m $\times$ 1.4 m) including CaF_2 crystal modules are observed by 14 of 20-inches PMTs and 48 of 13-inches PMTs with mirror light pipes. Figure 2.7 shows the installed position of PMTs. Each crystal module has different energy scales from the others since it has individuality in WLS phase and photon number difference from its location. This requires precise crystal identification and energy calibration for each module. These parameters are calculated by the offline analysis which is described in the next chapter.

Purification

Even if the $\beta\beta$ emitter with high $Q_{\beta\beta}$ is used, the detector should not be contaminated by radioactive impurities (U,Th series). Therefore, purification processes are performed to crystals, active(LS) and passive(water) veto phase.

- On the stage of the crystal production, the impurities are removed from CaF_2 compounds by chemical approach. we select ingredient powder of CaF_2 compounds based on concentration of U,Th series impurities that are measured by the Germanium detector.

- As a countermeasure against LS contaminations, there are the LS reserving tanks and purification equipment next to the detector tank. When the detector is not during observation, LS is preserved into the reserving tanks and purified by the system.

- Passive veto phase with pure water is cleaned by the pure water level maintenance system during observation. Furthermore, N_2 gas is flowed into the tank in order to remove the radioactive gas (radon etc.) and combustible oxygen from the internal gas of the detector.

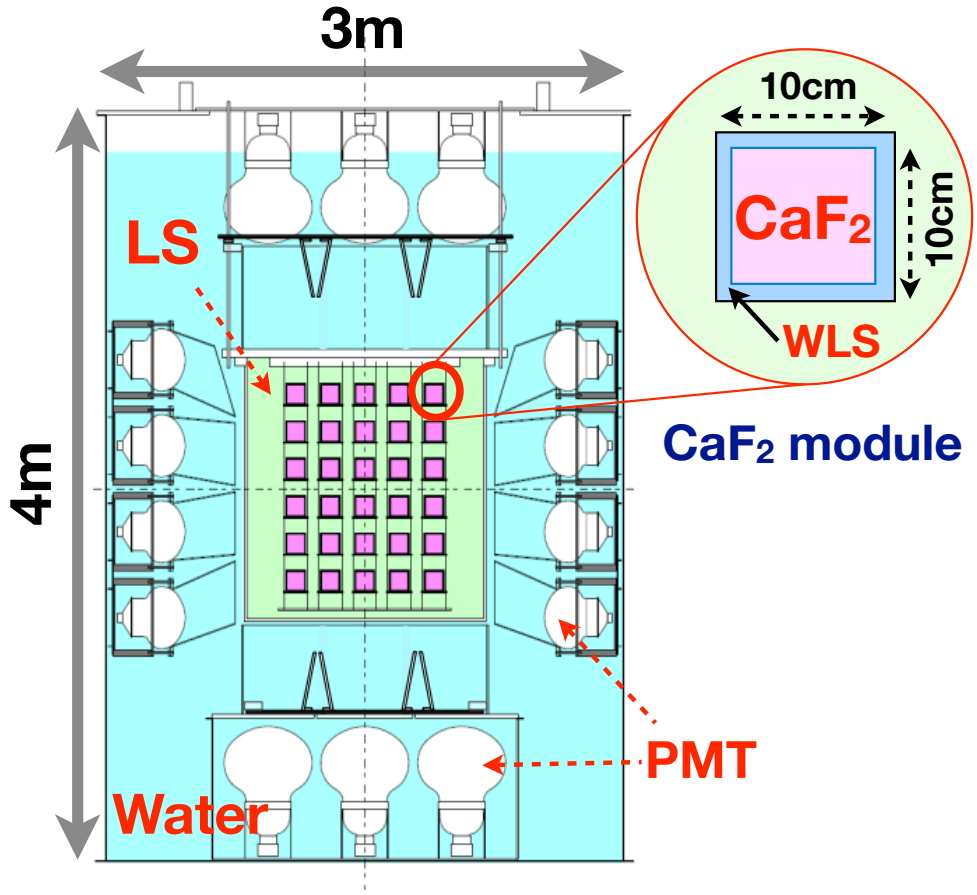

Figure 2.5: Setup of the CANDLES III(U.G.) Detector

Energy calibration system

Energy scales must be determined precisely for the detector. Good energy resolution is necessary to distinguish $0\nu\beta\beta$ events from high-energy tail of $2\nu\beta\beta$ events in the vicinity of $Q_{\beta\beta}$. We must consider that each crystal module has different energy scales from the others.

In order to estimate the scale of each crystal, we had to develop characteristic energy calibration system. We planned to operate the standard γ-ray source nearby crystals into the LS tank. Then the system should gain access to flammable LS phase, and therefore O_2 contamination must be prevented in a safety requirement. In addition, in order to avoid electric speaks, source installation and operation must be performed without the use of mechanics. Considering requirements as above, the system was developed as the 30cm $\times$ 20cm $\times$

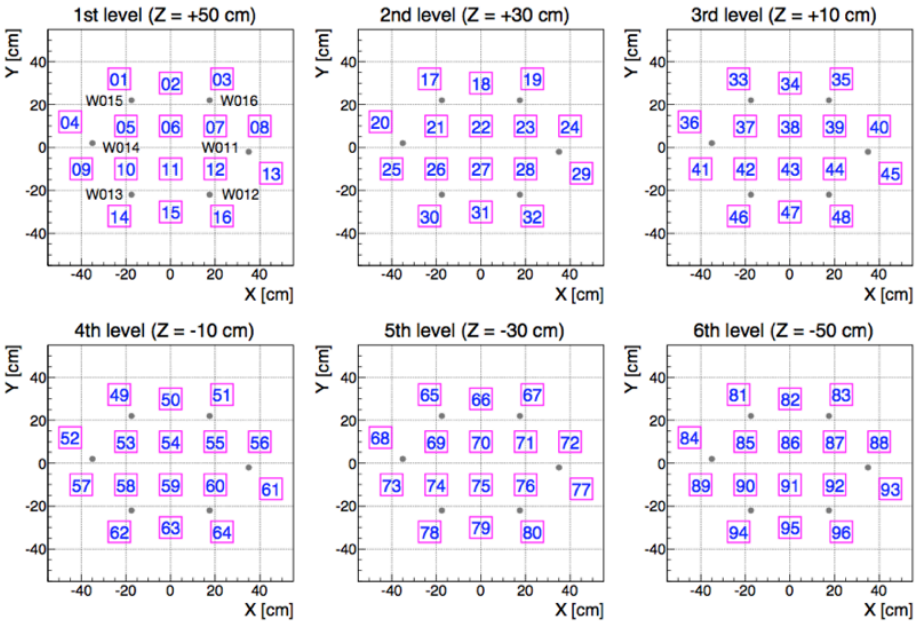

Figure 2.6: Crystal layouts of the CANDLES III(U.G.) Detector

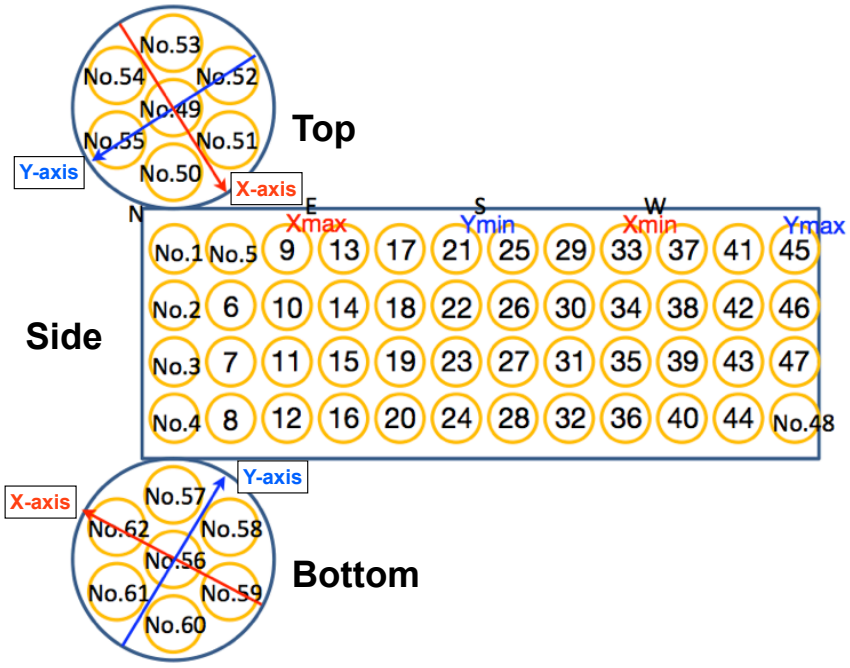

Figure 2.7: PMT layouts of the CANDLES III(U.G.) Detector

20cm stainless steel box(Fig. 2.8). We can attach this box to the detector tank when we perform energy calibration run, and at first, the inner part of the box is purged by flowing N_2 gas. The tank has six apertures to connect to the calibration system since crystals are distributed widely. These apertures are closed by equipped valves usually and opened in the case of calibration. A stainless wire and a reel are attached to the box, and the ϕ1cm $\times$ 2cm capsule is suspended by this wire. The cupsule is the jacket of small ^{88}Y (γ ray of E_γ = 898 keV, 1836 keV) RI source (Fig. 2.10 shows the decay scheme of ^{88}Y). Figure 2.9 shows both shapes of the source and the jacket. The reel has a vernier scale and a handle, and the source is installed nearby the crystal modules using this handle.

2.3.2 Electronics

DAQ system

The data acquisition system (DAQ system) is designed to take signals from CaF_2 scintillators. Figure 2.11 shows the circuit diagram of current system. The scintillation lights from CaF_2 scintillator and LS are viewed by 62 PMTs simultaneously. Raw signals are amplified to 10 times by amplifier modules. Each module has two output ports, one of which is used to input pulse shape into FADC (Flash A/D Converter) modules to record pulse shapes. Analog signals from 62 ports are summed up, also sent into FADC and used to make triggers of data taking.

Trigger

Triggers of data taking are made by dual gate trigger system (DGT). This system selects CaF_2 events immediately using decay constant that is different between CaF_2 and LS(Fig. 2.2). DGT handles two types of digital pulse, gate S1 and gate S2 (Table 2.2). Digital pulse is integrated for S1 and S2 gate indivisually. Trigger is issued if integrated values are both above thresholds. In other words, S1 and S2 are risen when a CaF_2 signal is caught, and only S1 is risen when a LS one or the other odd pulse comes. Trigger signal is sent due to timing of S2. Figure 2.12 shows the expression of dual gates against pulse shape and Figure 2.13 shows the trigger efficiency. Here energy threshold for β-ray is about 880 keV.

In addition, pulse shape discrimination (PSD) in offline analysis is also necessary to sweep the remaining LS or odd signal and to assess the type of event,

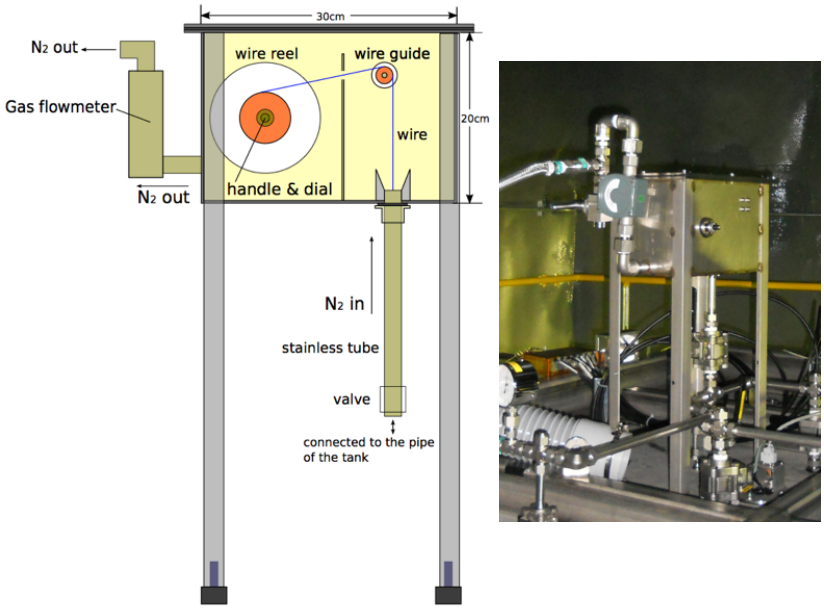

Figure 2.8: (Left) Design of the energy calibration system. This is made of stainless. (Right) The system attached to the detector.

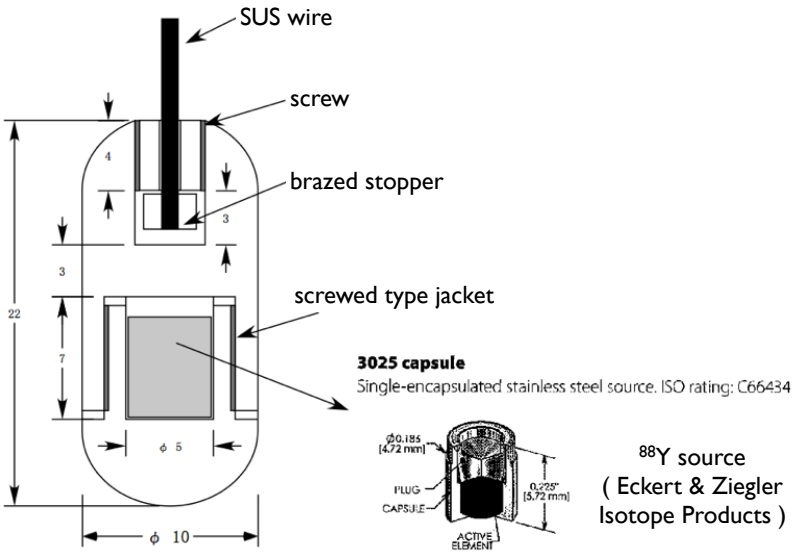

Figure 2.9: (Left) Design of the ^{88}Y and the jacket of the source.

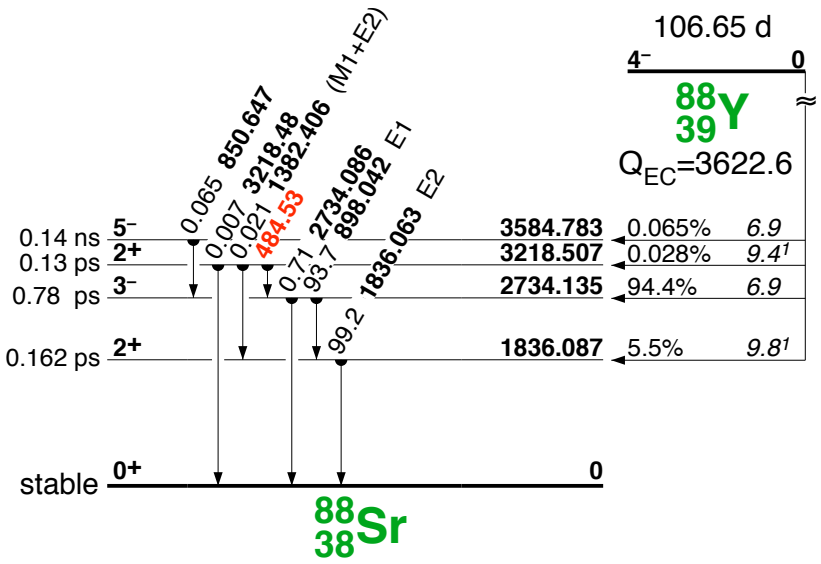

Figure 2.10: Decay Scheme of ^{88}Y [14].

Table 2.2: Settings of Double Gate Trigger

Gate	Time Width (ns)	Threshold (ADC Counts)	Delay Time (ns)
S1	128	1073	384
S1	168	3443	0

α or β. FADC modules are used to record and analyze the pulse shape. Waveforms of 62 PMTs are converted into digital form by FADC modules and are stored as raw data (Fig. 2.14). This form is expression of 384 channels. Pulse heights of first 512 ns, including about 130 ns pedestal in front of pulse rizing, is recorded as pulse height by 2 ns using 256 channels. Shape of next 8.2 μs is recorded as pulse height by 64 ns using 128 channels. Coarse recording of latter pulse shape causes reduction of data size. Details of PSD is presented in next chapter.

2.3.3 Comparison to the ELEGANT VI detector

The CANDLES experiment and the ELEGANT VI experiment focus on $0\nu\beta\beta$ of ^{48}Ca. CaF_2(Pure) has longer attenuation length than CaF_2(Eu) and allows us to expand the detector in three-dimension. Table 2.3 shows the detector comparison of two detectors. In the target mass, the CANDLES III detector has exposure which is about 45 times as large as that of the ELEGANT VI detector. In addition, with expansion of crystal cubes from 4.5 cm to 10 cm on each side, the higher detection efficiency for $\beta\beta$ events is expected. The surface of crystal is inefficient to detect $0\nu\beta\beta$, because β-rays emitted in this area escape to the outside of the crystal without full energy deposit. The ratio of this inefficient area to total scintillator can be reduced by enlarging crystal volume.

ELEGANT VI performed zero background measurement in 2 years and obtained the most stringent limit for $0\nu\beta\beta$ of ^{48}Ca. If CANDLES III also performs zero background experiment, It can achieve the sensitivity of ELEGANT VI in less than 2 weeks experiment.

Table 2.3: The comparison between ELEGANT VI and CANDLES III

	ELEGANT VI	CANDLES III
Material	CaF_2(Eu)	CaF_2(Pure)
Crystal size	$4.5 \times 4.5 \times 4.5$ cm^2	$10 \times 10 \times 10$ cm^2
# of crystals	23	96
Target mass in total	6.7 kg	305 kg

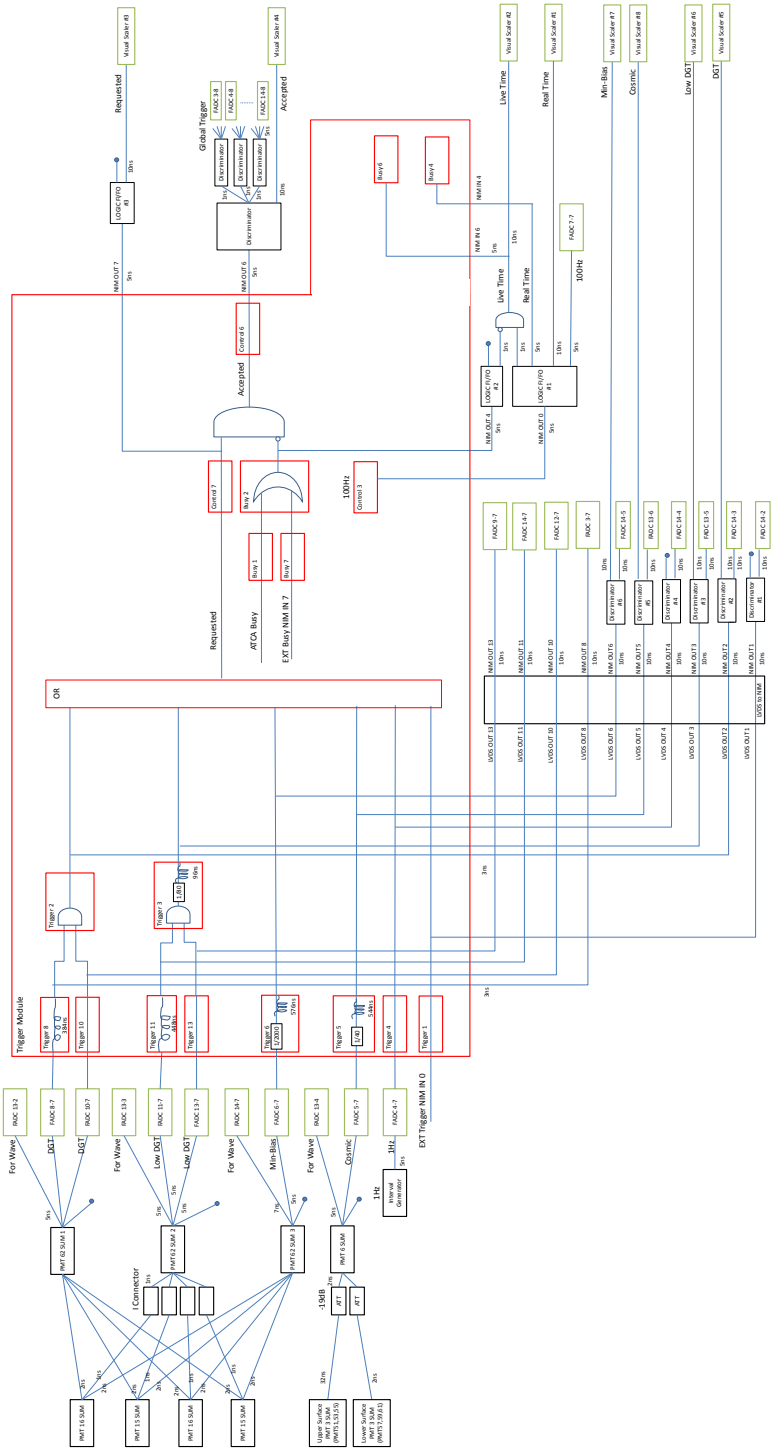

Figure 2.11: Circuit Diagram of CANDLES III(U.G.).

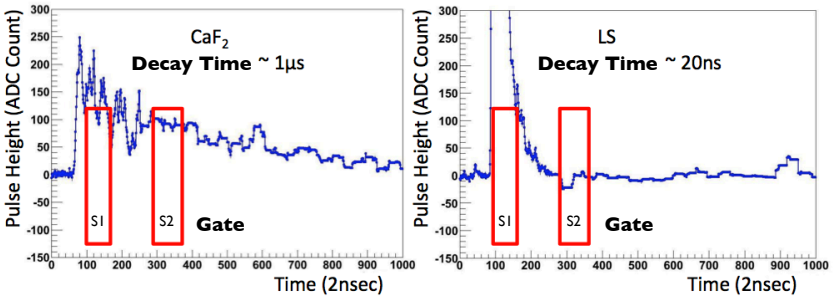

Figure 2.12: Double gate (S1 and S2) position against input pulse shape. (Left) CaF_2 pulse. (Right) LS pulse.

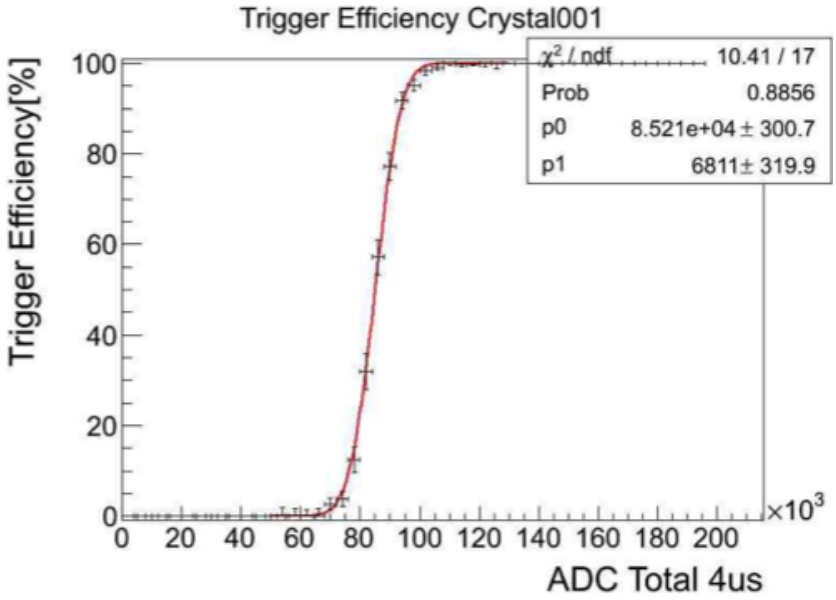

Figure 2.13: Trigger efficiency against crystal #1 [23]. Red curve is the fitting function $\mathrm{err}(x) = 100/2 \times \{1 + \mathrm{erf}(x - p_0/\sqrt{2}p_1)\}$. The edge of efficiency is on 81412 as integrated ADC values by 4 μs. This corresponds to 880keV of CaF_2 energy.

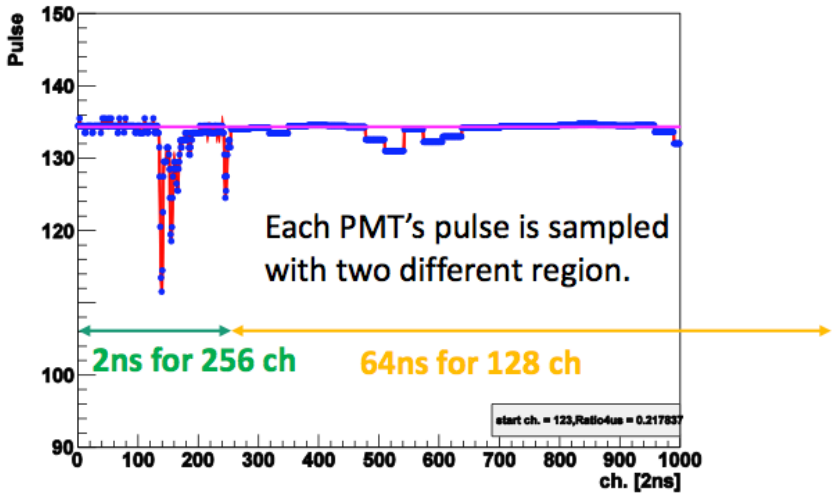

Figure 2.14: An example of digitized pulse shape. Pulse of First 512 ns is recorded by 2ns, and latter 8 μs is coarsely recorded.

Chapter 3

Analysis

3.1 Event Reconstruction

In order to distinguish $0\nu\beta\beta$ events from backgrounds, we take several steps in offline analysis. Methods of event reconstruction and event selection are described in this section.

3.1.1 Informations from Pulse

We get important information from a pulse shape in each event: energy deposition in scintillator, event position, a scintillator type (CaF_2 or LS) and particle type (β or α).

Light from scintillators are caught by 62 PMTs and recorded in "the raw data" as a voltage on each bin (first 256 bins per 2 ns and latter 128 bins per 64 ns) and time stamp by Flash ADC. The raw data is analyzed by "Pre-Analyzer" program (see Fig. 3.1). At first, analyzer tags bad quality events. Next, integrated charge for 4 μs from pulse-starting channel for each PMT is calculated. Pedestal is calculated using non-pulse events that are taken by 1 Hz clock trigger. Integrated charge for each PMT is used for position reconstruction. The number of photons entering into each PMT is used for energy reconstruction. Meanwhile, one-photon events are used for measuring a conversion factor from charge to photoelectron for each PMT. Next, 62 pulses are summed up after aligning pulse-starting timing. From this summed pulse shape, scintillator type and particle type are distinguished by pulse shape discrimination (PSD). Energy, position and PSD parameters are calculated by "Main Analyzer" program.

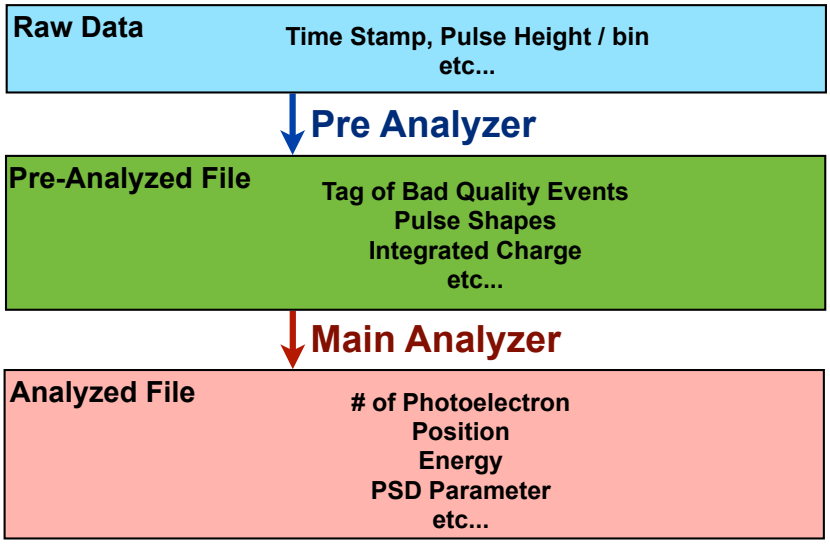

Figure 3.1: Flowchart of analysis.

3.1.2 Bad Quality Events

In the CANDLES system, occasionally bad quality events are recorded in the data. These bad events are categorized as below.

1. Events with saturated PMT signal. The main cause of saturation is large pulse shape of LS emission.

2. Start channel errors. These are the cases that the start channel cannot be recognized in the region of first 512 ns.

3. Events with overshoot PMT signal. These are cases that kickstart pulses are higher than pedestal.

Pulse shapes of these bad quality events are shown in Fig. 3.2. These are tagged separately by Pre-Analyzer, and can be removed as necesarry. In $0\nu\beta\beta$ study, we reject start channel errors and overshoot signals, but accept saturation signals not to remove events in $Q_{\beta\beta}$ region unjustly. Influence of saturation appears as lower shift of energy scale in high energy region described in section 3.1.5.

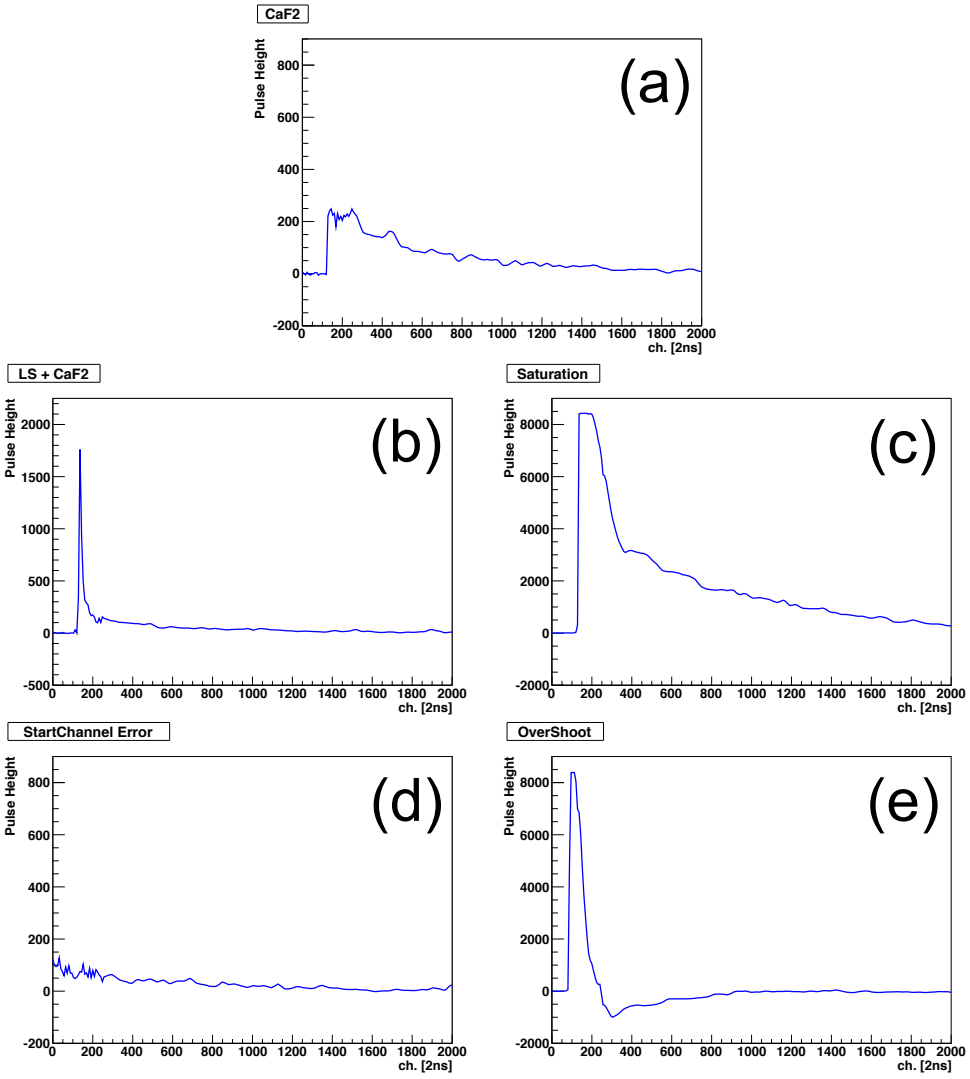

Figure 3.2: Good and bad types of pulse shape. (a) A normal CaF_2 pulse shape. (b) A normal LS+CaF_2 pulse shape. (c) A saturated signal. (d) Start channel error. (e) Overshoot.

3.1.3 Pulse Shape Discrimination

Chisquare values

Our primary concern is β decay in CaF_2 crystals and we must consider a reduction of α signal. we need to discriminate between β and α pulses in CaF_2, and LS scintillation pulses. Events without CaF_2 scintillation (only LS scintillation) are rejected by online dual gate trigger; still, CaF_2 events with small energy deposit in LS are left. These CaF_2 + LS emission events can be discriminated using pulse shape information taking advantage of large difference in decay constant (See Fig. 2.12). In addition, α-ray signal in CaF_2 has a little bit shorter decay constant than that of β-ray signal (See Fig. 3.3), which makes decay type discrimination possible using pulse shape.

Fine pulse shape discrimination (PSD) is performed in order to pick up β decay events. At first, reference pulses are generated from an avarage of about 10,000 events for each event types (β, α or β + LS) from data. Then each event pulse is fit to reference pulses, and chisquare values (χ^2_β,χ^2_α,$\chi^2_{\beta+\mathrm{LS}}$) are obtained. Chisquare value is defined as

$$\chi^2 = \frac{1}{d}\sum_i \left(\frac{f_i - e_{r,\,i}}{\sigma_i}\right)^2 \tag{3.1}$$

where d is the degree of freedom, i is the number of bin, f_i is the observed pulse voltage on each bin, $e_{r,\,i}$ is the pulse voltage of each reference pulse (r corresponds to the type of events; α, β, or β + LS) and σ_i is the error of observed f_i. In latter 128 bins (64 ns sampling) region, one photoelectron is normally observed in only one bin, which means that the observed voltage is simply proportional to the number of observed photoelectron and σ_i is equivalent to the voltage conversion value of the photoelectron fluctuation. On the other hand, in first 256 bins (2 ns sampling) region, one photoelectron is observed across several bins because of $\sim$ 7 ns width of the photoelectron signal. Therefore, the shape of the photoelectron signal is assumed as gaussian to calculate σ_i.

We use these values as pulse shape parameters. For example, imposing a upper limit on χ^2_β, other α-like and CaF_2 + LS signals can be rejected. Figure 3.4 shows distributions of two parameters, χ^2_α and χ^2_β. In addition, the cut inefficiencies by χ^2_β cut are shown in Fig. 3.5. The inefficiency of β selection by $\chi^2_\beta < 1.5$ is 93.7 %.

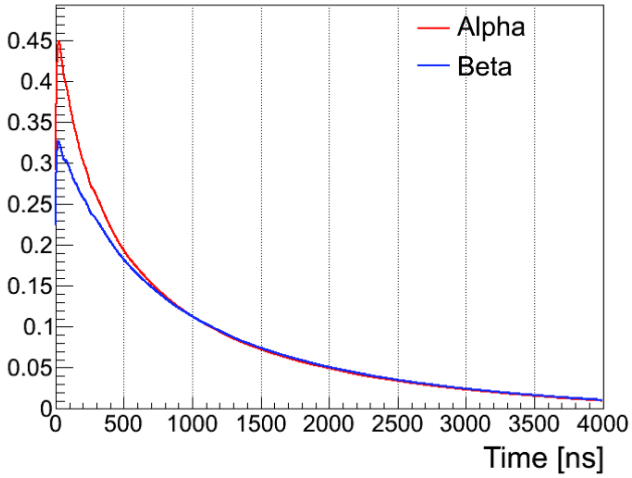

Figure 3.3: α (red line) and β (blue line) pulse shapes. A slight difference in decay constant makes a gap of pulse shape, especially in first 500 ns region.

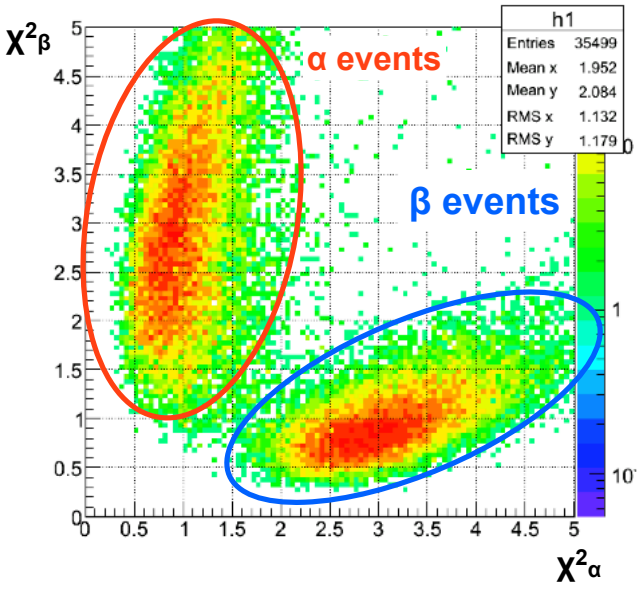

Figure 3.4: Example distributions of χ^2_α and χ^2_β. α events and β events can be separated with these parameters.

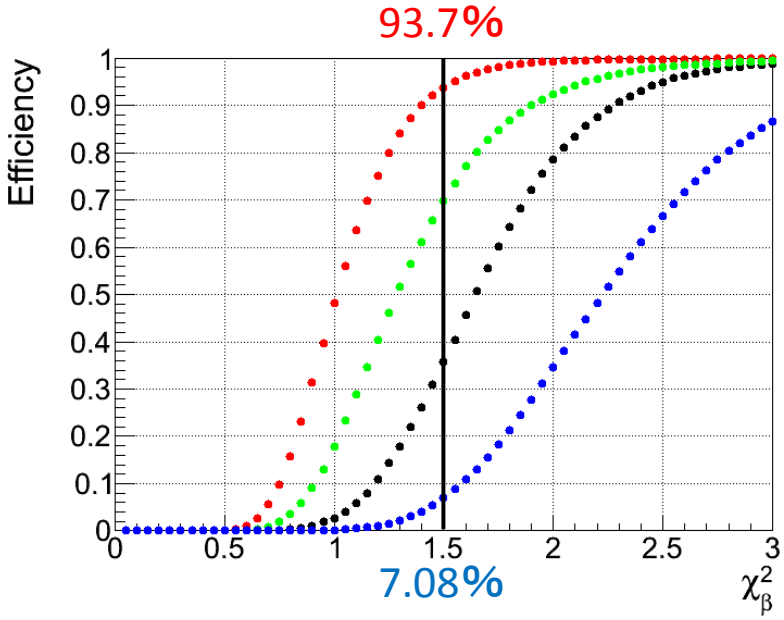

Figure 3.5: Cut inefficiencies for β, α, β+LS events by χ^2_β cut at 2.6 MeV. Red points correspond to β events, black points to α events, green points to β events + LS 30 $\sim$ 50 keV and blue points to β events + LS 90 $\sim$ 110 keV.

Shape Indicator

We also use "Shape indicator (SI)" [24] based on the Gatti parameter [25] as an additional pulse shape parameter. This value is calculated from the equation below,

$$SI \propto \sum_i \frac{e_{\alpha,\,i} - e_{\beta,\,i}}{e_{\alpha,\,i} + e_{\beta,\,i}} f_i \tag{3.2}$$

where i is the number of bin, f_i is the observed pulse voltage on each bin and $e_{r,\,i}$ is the pulse voltage of each reference pulse (r corresponds to the type of events; α, β). Shape indecator performs particle identification between α and $\gamma(\beta)$ rays (See Fig. 3.6). This value is mainly used in order to discriminate α signals of backgrounds from Th-chain impurities in crystals.

3.1.4 Position Reconstruction

Each crystal module has different energy scales from the others. For this reason, we should identify a crystal module in which a radiation ray deposits energy.

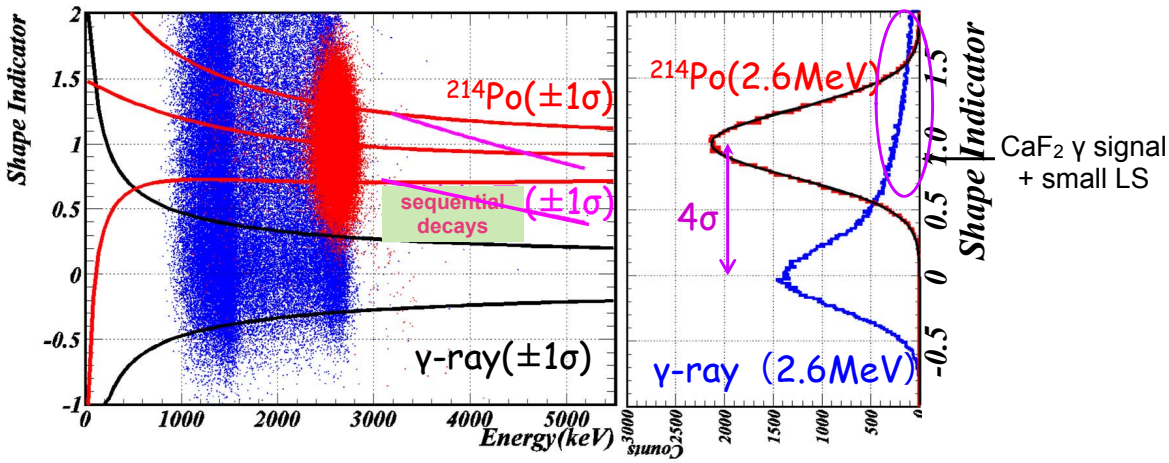

Figure 3.6: Example distributions of Shape Indicator (SI) using ^{214}Po α signal (visible E_α = 2.6 MeV, red points) and ^{208}Tl γ signal (E_γ = 2.6 MeV, blue points).

As a result, analyzing event position is essential. Here we use weighted mean method for event reconstruction discribed below,

$$\vec{r} = \frac{\sum_{m=1}^{62} I_m F_m \overrightarrow{\mathrm{PMT}_m}}{\sum_{m=1}^{62} I_m F_m}, \tag{3.3}$$

where $\vec{r}$ is a position vector of event (x, y, z). m is PMT number(1~62), I_m is the integral of pulse charge for each PMT, F_m is photoelectron number factor which is given for each PMT, then $I_m F_m$ corresponds to an amount of photoelectrons which PMT(number m) observes. In addition, $\overrightarrow{\mathrm{PMT}_m}$ is a position vector of each PMT.

Figure 3.7 shows distributions of reconstructed position. Then rough β events selection ($\chi^2_\beta < 3$) is performed. The distortion of position is seen especially in z-axis, which is caused by worse photoelectron collection efficiency of PMTs set on upper of the detector (see Section 5.2). Nevertheless, comparing with Fig. 2.6, position reconstruction reproduces crystal distribution and identification.

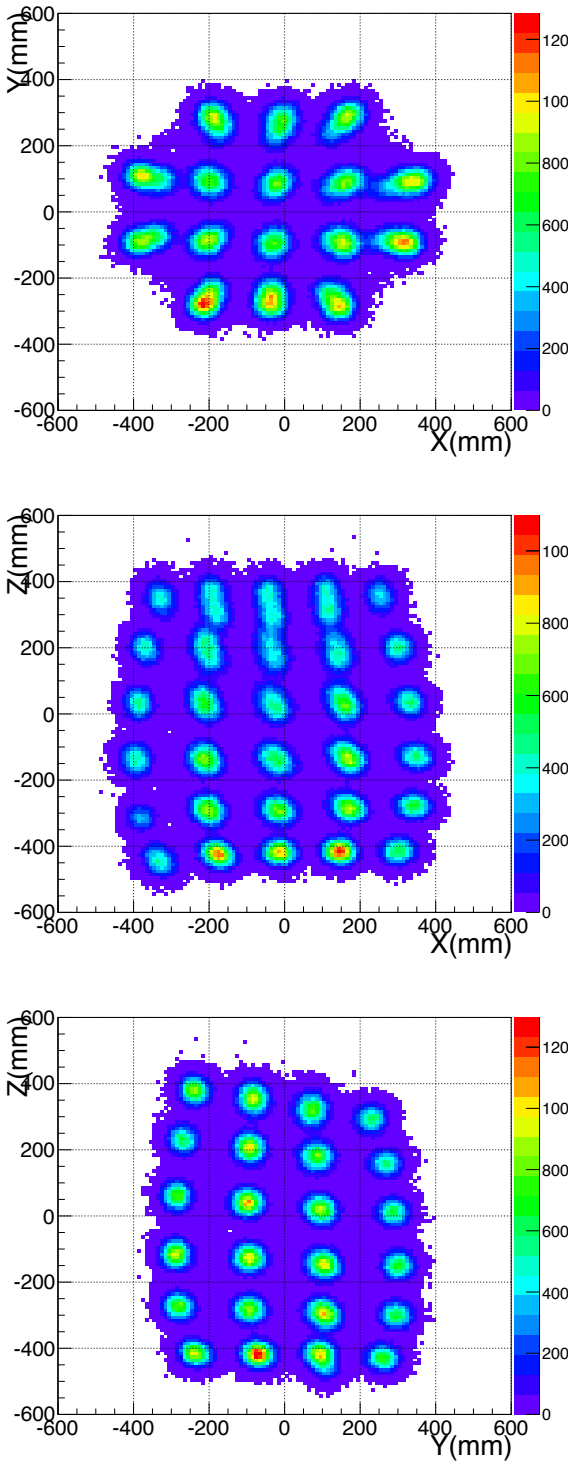

Figure 3.7: Position reconstruction. (Top) Top view (x-y axis). (Middle) Side view (x-z axis). (Bottom) Side view (y-z axis).

3.1.5 Energy Reconstruction

Energy information is given as integrated value of the 4 μsec waveform. Energy E is simply calculated below,

$$E = T_{\mathrm{date}} f_n \sum_{m=1}^{62} I_m F_m \tag{3.4}$$

where T_{date} is a correction factor which is obtained by temperature of the detector per day (See Fig. 3.8), n is crystal number(1~96), and m is PMT number(1~62). In addition, f_n is energy scale factor which is given for each crystal. f_n is given by energy calibration measurement with standard γ-ray source. This value must be determined precisely, because good energy resolution is necessary to distinguish $0\nu\beta\beta$ events from high-energy tail of $2\nu\beta\beta$ events. In addition, each crystal module has different energy scales from the others. For this reason, f_n of each module must be measured individually.

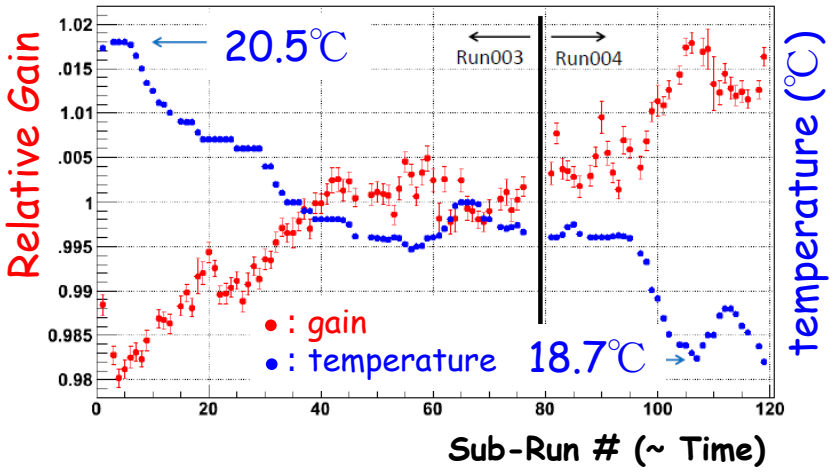

Figure 3.8: Detector temperature (blue) and ralative energy scale (red). Horizontal axis shows the sub-run number corresponding to the number of days. This figure shows that energy scale has negative correlation to detector temperature.

Energy Calibration with ^{88}Y RI source

Energy scale of each module must be measured with points of energy as close as $Q_{\beta\beta}$. The standard source ^{88}Y which usually emits 898 keV and 1836 keV γ-

rays in single electron capture reaction is used for energy calibration (Fig. 2.10). 1836 keV is the highest energy (the closest to 4.27 MeV of $Q_{\beta\beta}(^{48}\mathrm{Ca})$) in standard RI source.

Small ^{88}Y source is hanged on and put on positions among crystals in LS tank. Factors of crystals can be measured at a certain position of the source. We can measure energy scales at 1836 keV of all crystals by changing source position. Figure 3.9 shows an energy spectrum of this calibration measurement. The highest peak corresponds to 1836 keV γ-ray, and sum peak of 898 keV and 1836 keV γ-rays can be seen. 898 keV events are usually lower than energy threshold. We calculate the energy scale f_n using a charge value of 1836 keV. Figure 3.10 shows a center value of 1836 keV peak at each crystal. The variation of the energy scales for each crystal is 14 %. Energy spectrum of total crystals is obtained by applying the energy factor for each crystal.

Energy Calibration with neutron source

In order to estimate energy scales in $Q_{\beta\beta}$ region, calibration run with ^{252}Cf neutron source and Si, Ni blocks were performed. No isotope emits γ-rays with energy of 3 MeV or higher spontaneously. On the other hand, when a nucleus captures a single neutron, it is excited and quickly decays to a ground state with emission of γ-rays (called (n,γ) reactions). Several nuclei can emit high energy γ-rays with (n,γ), which are useful for high energy calibration of the detector. Therefore, calibration run with ^{252}Cf neutron source and absorbers were performed. Here silicon (Si) and nickel (Ni) were selected as neutron absorbers. Energy of γ-rays from (n,γ) is shown in Fig. 3.11. The silicon absorber was the form of blocks with the size of 30 cm $\times$ 30 cm $\times$ 40 cm including 63 % of silicon. The nickel absorber was the form of a polyet ball with 18 cm in diameter including 35 % of nickel oxide. Information about ^{252}Cf source is presented in Chapter 4. Both scematic views are shown in Fig. 3.12. Especially Si has γ-ray emission at 3.5 MeV and 5 MeV which can be used to check energy linearity in $Q_{\beta\beta}$ region.

By calibration runs with two absorbers, (n, γ) spectra were obtained (shown in Fig 3.13). Energy peaks of high energy γ-rays could be observed. In addition, an energy peak in 7.6 MeV could be seen. This peak was observed even in background measurement (meaning observation with ^{252}Cf source without absorbers). This was caused by (n,γ) reactions of iron (Fe) included in the stainless steel tank. With these energy peaks, linearity of energy was studied as shown in

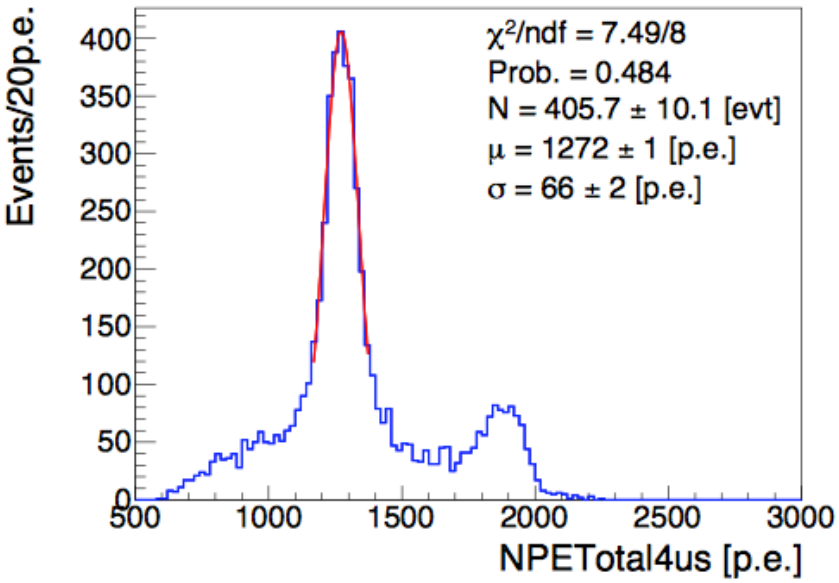

Figure 3.9: Example of energy spectrum in ^{88}Y calibration run. Events in crystal No.1 are extracted using position reconstruction. Horizontal axis shows the sum of the number of photoelectrons (p.e.). The highest peak at 1272 p.e. corresponds to 1836 keV γ-ray events.

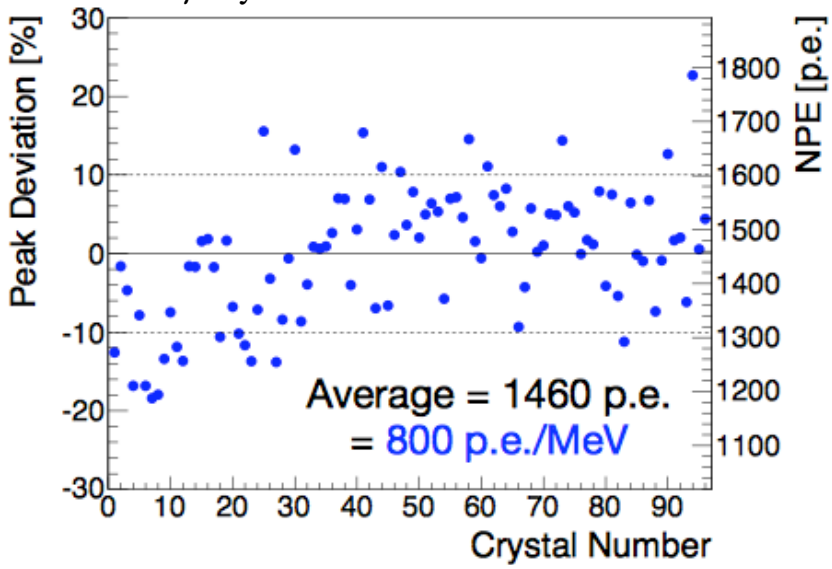

Figure 3.10: Energy scale as a center value of 1836 keV peak at each crystal. Holizontal axis shows crystal number.

next section.

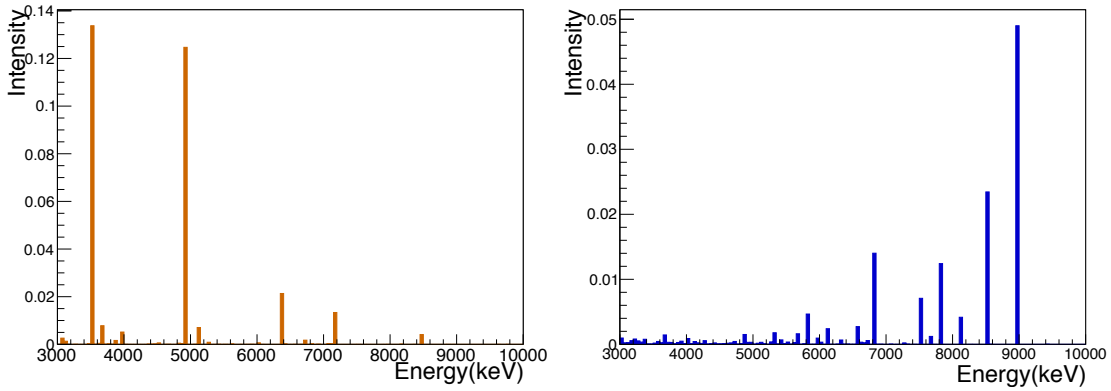

Figure 3.11: A calculated γ-ray spectrum from (n,γ) reaction in silicon (Si, left) and nickel (Ni, right) absorbers. Energy and cross section of each γ-ray are from [22].

Energy Scale around $Q_{\beta\beta}$

Energy calibration with ^{88}Y only enables to estimate calibration factors in the energy region at 1836 keV. One of our primary demand for $0\nu\beta\beta$ search is precise energy reconstruction in the region around $Q_{\beta\beta}$ of ^{48}Ca (4.27 MeV). Meanwhile, current energy resolution of $Q_{\beta\beta}$ is estimated as $\sigma/\mu \sim 3$ % (See Fig. 3.16), and therefore uncertainty of energy determination should be enough smaller than this value. Here we must confirm that energy factor estimation on lower energy ($\sim$ 2 MeV) can be applied on the region around $Q_{\beta\beta}$. Thus, we performed linearity check using 3.5 $\sim$ 9 MeV γ rays from neutron capture (n,γ) reactions. These measurement were performed with ^{252}Cf neutron source. We examined the linearity of the whole detector using energy peaks below:

- γ-ray peaks of environmental ^{40}K (1.4 MeV) and ^{208}Tl (2.6 MeV),
- 3.5 MeV and 5 MeV γ-rays from (n,γ) at silicon (Si),
- 7.6 MeV γ-ray from (n,γ) at iron,
- 8.5 MeV and 9 MeV γ-rays from (n,γ) at nickel (Ni).

Figure 3.12: Schematic views of Si (Left) and Ni (Right) absorbers.

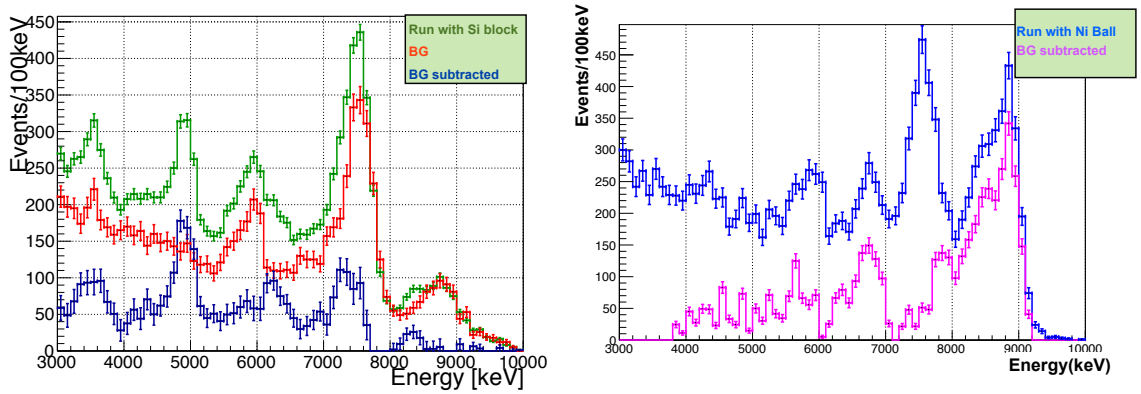

Figure 3.13: (Left) Observed energy spectra of ^{252}Cf source runs with Si block. The spectrum with background subtracted is shown in blue solid line. We see peaks at 5 MeV and 3.5 MeV in this spectrum. (Right) Observed energy spectra of ^{252}Cf source runs with Ni Ball. The spectrum with background subtracted is shown in purple solid line. We see peaks at 9 MeV, 8.5 MeV and 6.8 MeV are shown in this spectrum.

Figure 3.14 shows comparison between calculated energy and real energy. Calculated energy is getting lower than real value in the energy region above 3 MeV. These shifts of energy are from saturated signal of small LS deposit (see in FIg.3.15). In $Q_{\beta\beta}$ region, difference between calculated energy and real energy is estimated as about 0.4 %. We can calculate the energy value of events with better accuracy than energy resolution. Current energy resolution of CANDLES III is shown in Fig. 3.16. We estimate energy resolution in 4.27 MeV at ~ 6 % in FWHM.

3.2 Analysis of Physics Run

In this section, we show analysis of physics run for $0\nu\beta\beta$ search. We have performed some series of physics run continuously since 2012. In this thesis, one series of physics run (called "Run005") is used for the background and sensitivity investigation. This series was performed from June 2013 to October 2013 which has the live time of 61.0 days and exposure of 1.86×10^4 kg×day (96 crystals).

3.2.1 Conceivable Background Sources in $Q_{\beta\beta}$

When we search for $\beta\beta$ events in energy spectra, tight background reduction must be applied. In this observation, $0\nu\beta\beta$ events will be shown as signals of β-ray, in $Q_{\beta\beta}$ the energy region and position in crystal. $0\nu\beta\beta$ events are selected using the information from event reconstruction as explained in section 3.1 ; however, a part of backgrounds which cannot be rejected by this method, especially in the $Q_{\beta\beta}$ energy region, must be rejected using another analysis described below. Conceivable backgrounds in $Q_{\beta\beta}$ region are caused by ^{232}Th impurities in the detector, in other words, two decays in Th-chain (Fig. 3.17) can be backgrounds.

- ^{212}Bi-^{212}Po sequential decays

$$^{212}\mathrm{Bi} \rightarrow {}^{212}\mathrm{Po} \rightarrow {}^{208}\mathrm{Pb} \tag{3.5}$$

  Half-life of ^{212}Po is 0.3 μsec which means that total energy of these sequential decays is a problem. Q-value of ^{212}Bi β decay is 2.248 MeV.

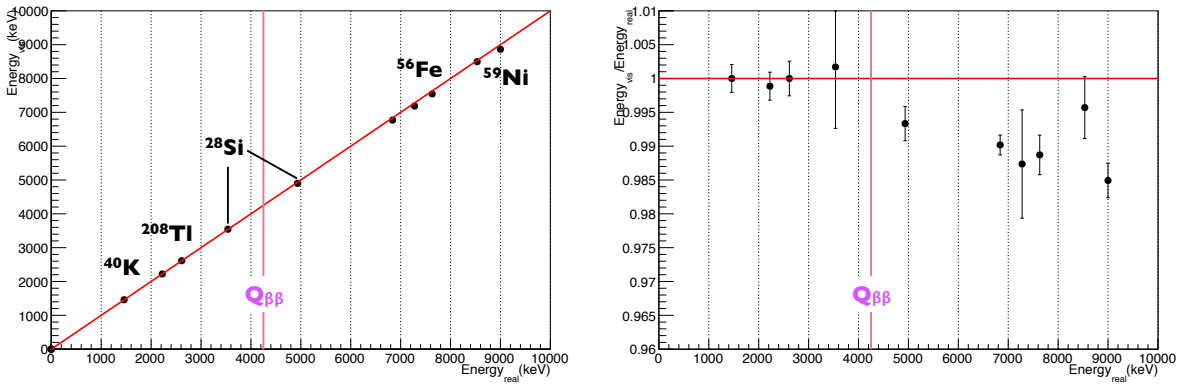

Figure 3.14: (Left) Calculated energy using factors (vertical axis) for each observed peak having known energy (horizontal axis). (Right) Linearity expression with rate of calculated energy to real value.

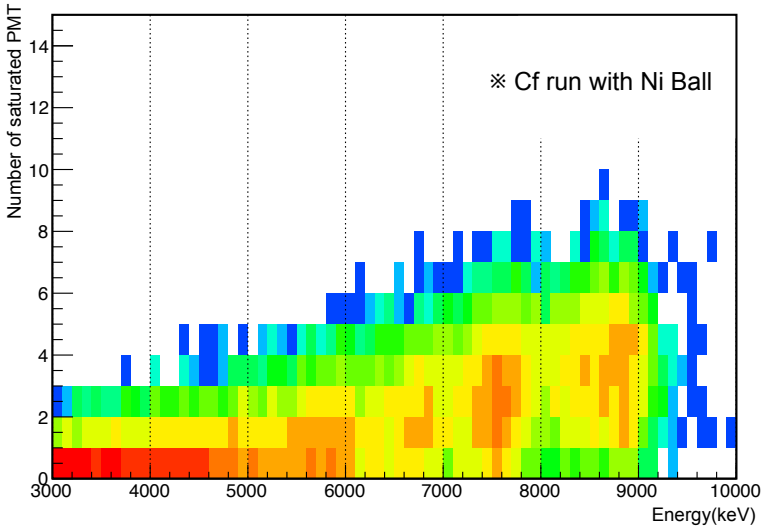

Figure 3.15: Number of saturated PMT versus for calculated energy in Cf run with Ni Ball. Above 5 MeV, the central value of number increases as energy increases.

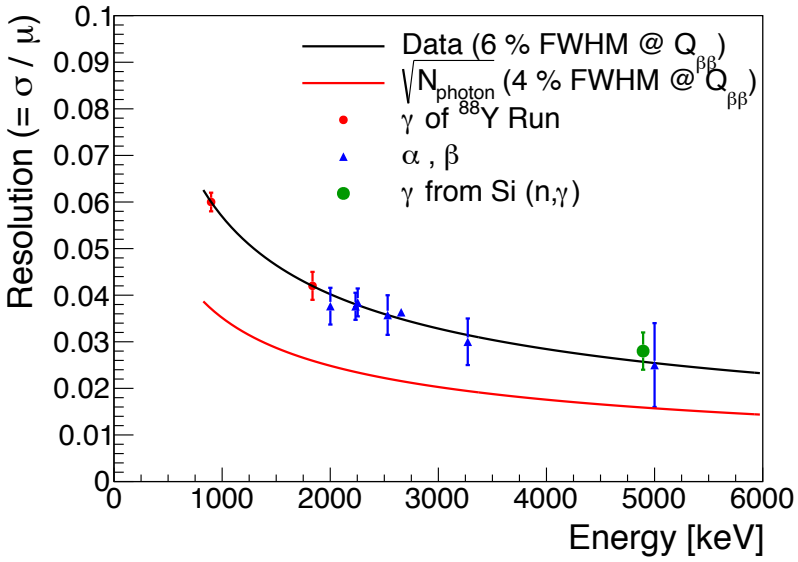

Figure 3.16: Energy resolution of the CANDLES III detector. Black line shows observed resolution, and red line shows estimated resolution from photon statistics.

Q_α of ^{212}Po α decay is 8.785 MeV but CaF_2(Pure) scintillator quenches α-ray in a factor of about 0.3. This makes visible Q_α about 3 MeV. In total, visible energy of ^{212}Bi-^{212}Po sequential decays are distributed up to 5 MeV region, as a result, these decays can be backgrounds. Figure 3.18 shows two cases of pulse shapes in ^{212}Bi-^{212}Po sequential decays.

In order to exclude these events, two method are performed. In the case long sequential time lag in which a kickstart of ^{212}Bi β decay and that of ^{212}Po α decay are separated clearly, we perform a time difference discrimination to find these kickstarts. More than 95 % of ^{212}Bi-^{212}Po decays can be discriminated and excluded. in the case of short interval event In the case of shorter interval event, a time difference discrimination method may not work well. We use SI as an additional pulse shape parameter in this case. To regard a summed pulse with short interval as an "α-like" pulse, we can exclude sequential decay backgrounds using SI. Figure 3.19 shows SI distributions of sequential decays in energy region near $Q_{\beta\beta}$. For $0\nu\beta\beta$ search, events in purple box ($0\nu\beta\beta$ window) is established as SI limit in -3σ ~ +1σ and ΔT < 10ns. Finally, reduction efficiency of

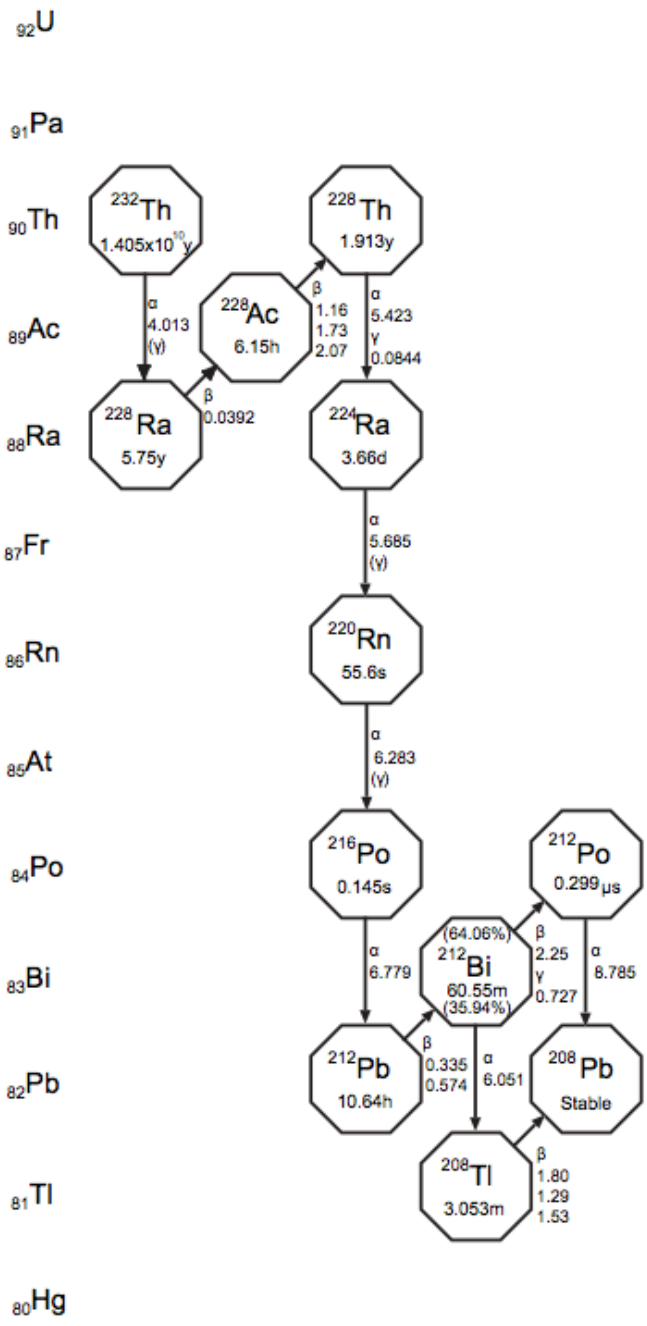

Figure 3.17: Th-chain.

^{212}Bi-^{212}Po sequential decays backgrounds at 4.27 MeV attains more than 99 %. The detection efficiency for $0\nu\beta\beta$ of this selection corresponds to 84 %. This efficiency is calculated from the number of data in 2.6 MeV ($\pm$ 1 σ) ^{208}Tl γ peak which decreases when the selection is applied.

- ^{208}Tl β decays

$$^{212}\mathrm{Bi} \rightarrow {}^{208}\mathrm{Tl} \rightarrow {}^{208}\mathrm{Pb} \tag{3.6}$$

Q_{β^-} of ^{208}Tl β decay is 5.0 MeV (shown in Fig. 3.20). Although we can ignore 2.61 MeV γ emission from ^{208}Tl, $\beta + \gamma$ events can be background. In order to remove ^{208}Tl events, we must focus on ^{212} Bi α decays that are previous events of ^{208}Tl β decays. Q_α of ^{212}Bi α decay is 6.05 MeV, corresponding to visible Q_α of about 1.7 MeV. Half-life of ^{208}Tl is 3.0 min.

Reduction of ^{208}Tl β signals is performed using time coincidence method between parent ^{212}Bi α signals and daughter ^{208}Tl β signals. α signals in 1.7 MeV region ($\pm$ 3 σ) are selected using χ^2_α and SI. These are regarded as ^{212}Bi α signals. Then, all events within 12 minutes (four times of ^{208}Tl half-life) from timing of each ^{212}Bi α signal in same crystals are excluded (see Fig 3.21). In this method, reduction efficiency of ^{208}Tl β decays attained about 60 %, and data acceptance rate is estimated as 66 %.

3.2.2 Event Selection

When we search for $0\nu\beta\beta$ events in energy spectra, we perform event selection with event reconstruction parameter and background reduction. We must study β events which occur in CaF_2 crystals. In addition, backgrounds of known causes (^{212}Bi-^{212}Po sequential decays and ^{208}Tl β decays) must be rejected. From above mentioned requirements, we set limits to event reconstruction parameters (named "$0\nu\beta\beta$ selection") :

- Reduction of bad quality events.
- $\chi^2_\beta < 1.5$ to remove LS + CaF_2 events.
- SI selection ($-3\sigma <$ SI $< 1\sigma$) and double pulse cut to remove ^{212}Bi-^{212}Po sequntial decays.

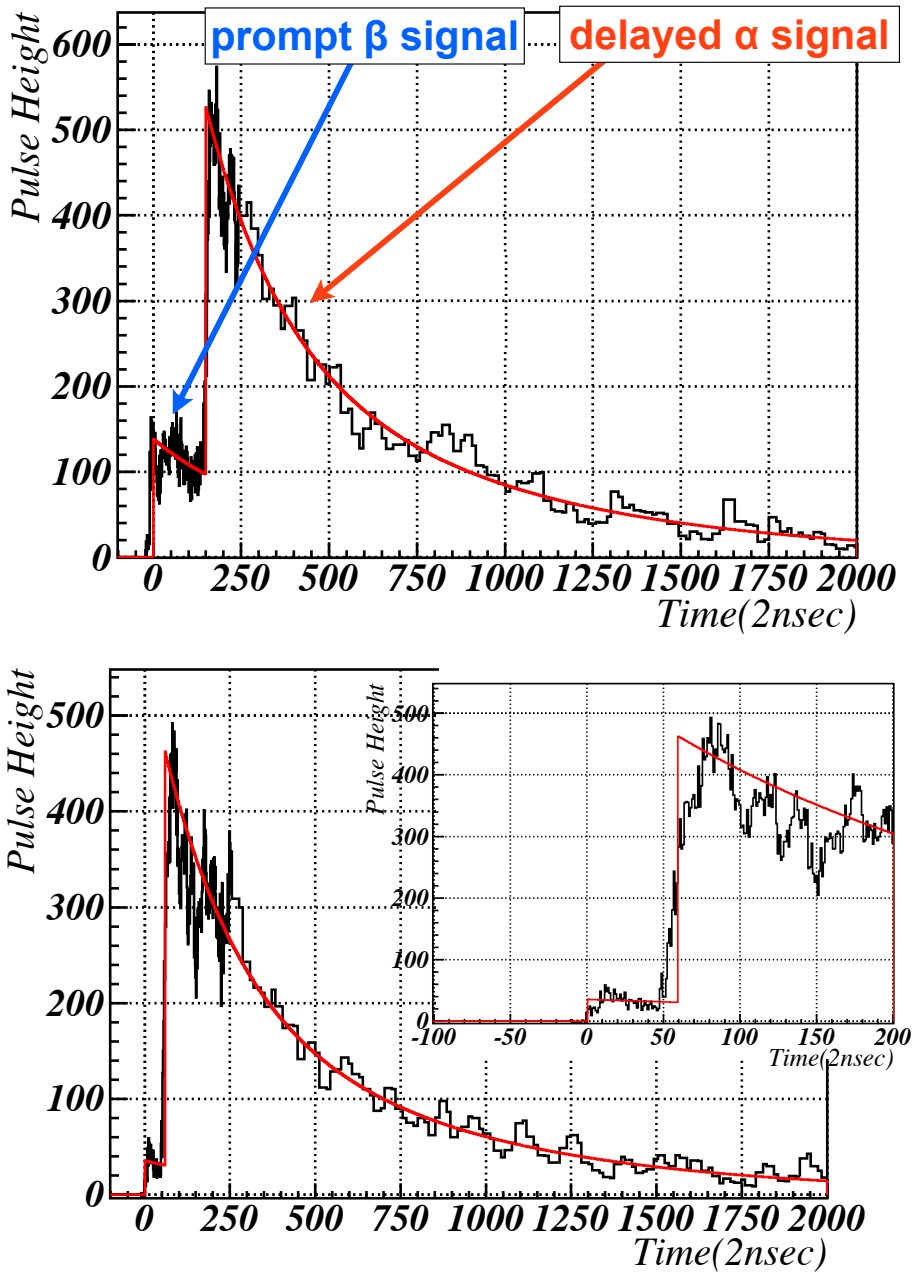

Figure 3.18: pulse shapes in ^{212}Bi-^{212}Po sequential decays. (Top) A typical case (time interval $\Delta T \sim 300$ ns). (Bottom) A case of short interval ($\Delta T \sim 120$ ns).

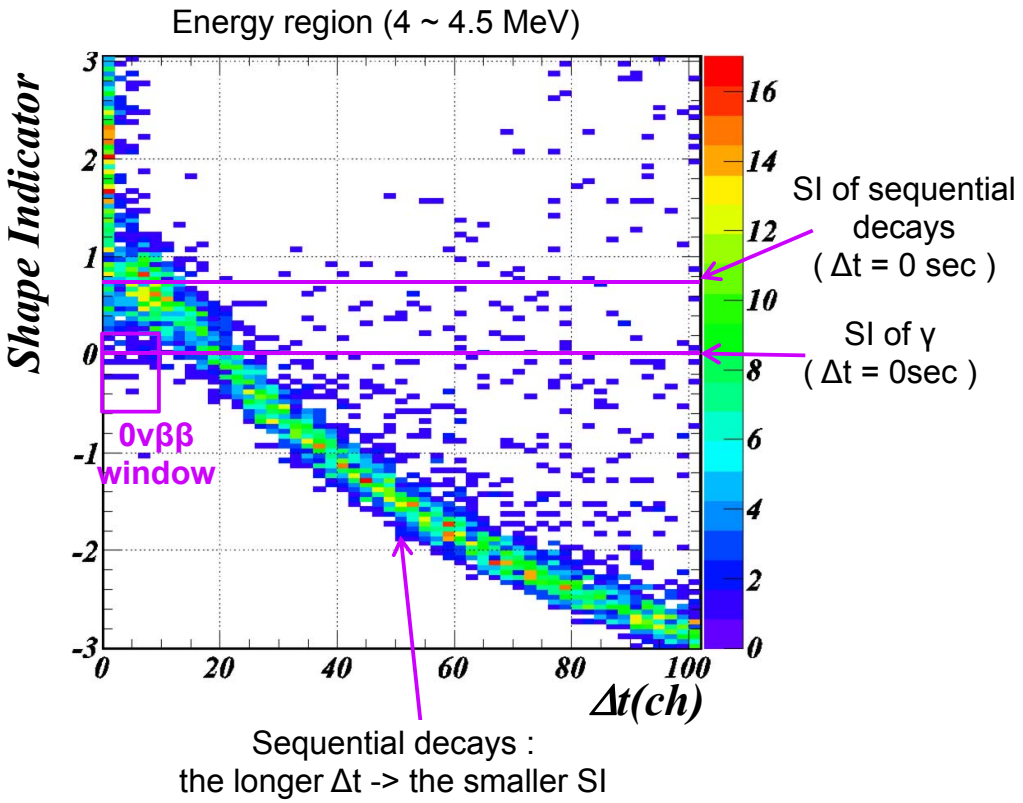

Figure 3.19: Distributions of time interval of ^{212}Bi-^{212}Po sequential decays (ΔT) and SI in energy region of 4 ~ 4.5 MeV. $0\nu\beta\beta$ window is figured by purple box.

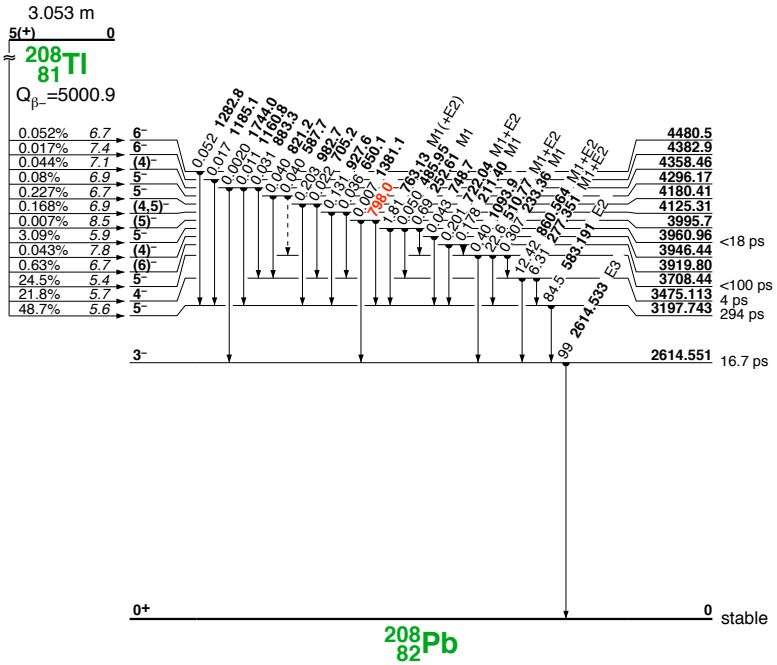

Figure 3.20: Decay Scheme of ^{208}Tl [14].

- Rejection of events after 12 minutes from the timing of each ^{212}Bi α signal.
- Selection of 26 of best purified crystals that are contaminations of ^{232}Tl < 10 μBq/kg. Events in ± 3 σ region from center position of these crystals (for each x, y, z axis) are selected.

Additionally, in order to study shapes of energy spectra, we also use loose "CaF_2 selection" very often:

- Reduction of bad quality events.
- $\chi^2_\beta < 3.0$.
- Selection of all 96 crystals. Events in 3 σ region from center position of these crystals (using the Gaussian fit) are selected.

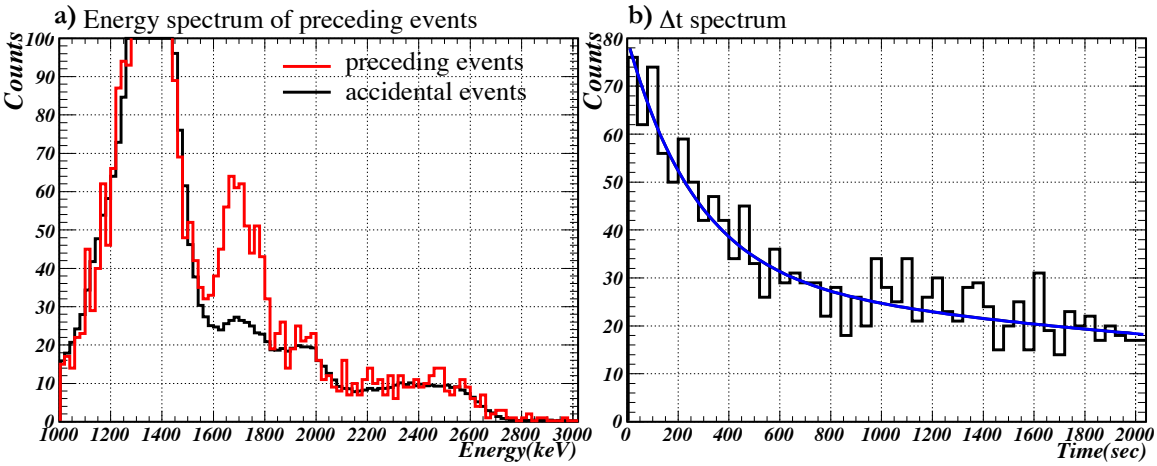

Figure 3.21: Figures of ^{212}Bi-^{208}Tl coincidence [26]. a) The energy spectra of the preceding events of ^{208}Tl. Red line corresponds to the preceding and black line to accidental events. The peak at 1.7 MeV is due to the prompt ^{212}Bi decay. b) δt distribution between the preceding and delayed events. This exponential curve (with accidental events) shows the half-life of 187 ± 56 sec.

3.2.3 Energy Spectra

Here we show observed energy spectra in 61.0 days live time. Figure 3.22 shows spectra with CaF_2 and $0\nu\beta\beta$ event selection. Structure in 3.5 ~ 5 MeV region of the blue spectrum mainly consists of ^{208}Tl β decay events, and we can see that this structure cannot be seen in red line. On the other hand, we can see 6 events in energy region of 4.16 ~ 4.48 MeV (according to energy resolution, $Q_{\beta\beta}$ - $1\sigma \sim Q_{\beta\beta} + 2\sigma$). The events are more than estimated the number of ^{208}Tl backgrounds (~ 1 events / 26 crystals / 61 days). This indicates that unexpected backgrounds exist. Focusing on the high energy region of the blue spectrum, there are a structure with two peaks. Peaks shows around 7.5 MeV and 9 MeV. These peaks will make low energy structure and influence as backgrounds in $Q_{\beta\beta}$ region. We must identify the origin of these unexpected backgrounds. The study of these high energy events is shown in the next chapter.

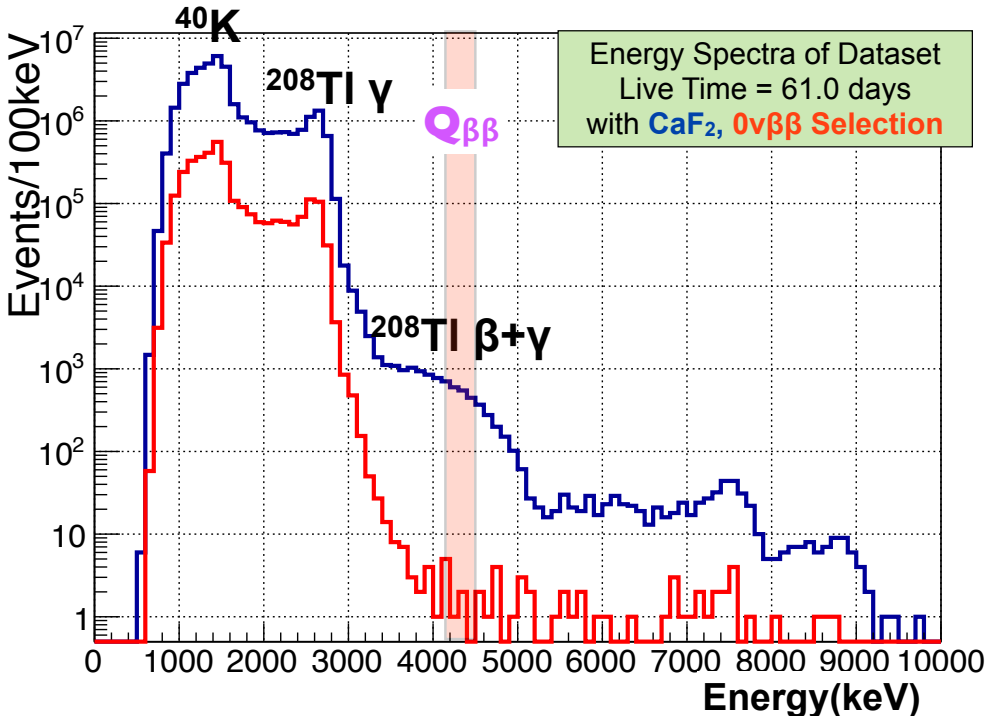

Figure 3.22: Energy spectra of 61.0days physics observation. Blue line corresponds to the spectrum with loose CaF_2 selection and red line corresponds to the spectrum with $0\nu\beta\beta$ selection.

3.2.4 Current Sensitivity

The sensitivity of $0\nu\beta\beta$ is calculated as below,

$$T_{1/2}^{0\nu} > \ln 2 \frac{MTaN_{\mathrm{A}}\epsilon}{\mu W}, \tag{3.7}$$

where M is the target mass, T is the measurement time, with following the Feldman-Cousins method [29], W is the morecular weight of the molecule, a is the abundance of $\beta\beta$ candidate per molecule, N_{A} is Avogadro's constant ($= 6.02 \times 10^{23}$ atom/mol [30]), ϵ is the detector efficiency, and μ is the highest Poisson signal mean which is derived from observed events and background events. Here μ is calculated using a number of observed background events. According to this formula, the sensitivity is proportional to the mass of the target, the isotopic abundance, the detector efficiency and approximately inverted proportional to the event rate (N_{event}/T).

Current sensitivity of CANDLES as limit for $0\nu\beta\beta$ half life of ^{48}Ca is calculated as

$$T_{1/2}^{0\nu}(^{48}\mathrm{Ca}) > 0.8 \times 10^{22}\mathrm{yr}. \tag{3.8}$$

The value of each parameter is listed in Table 3.1. Here, the detector efficiency $\epsilon \sim 0.3$ is estimated as the total efficiencies shown below;

- Detection efficiency for $0\nu\beta\beta$ events based on size of crystals and energy resolution. The efficiency is estimated by Monte Carlo simulation with the energy resolution of 6 % (FWHM) at $Q_{\beta\beta}$ to be 62 % (See Fig. 3.23).
- Bad quality cut efficiency ($\sim$ 100 %).
- Position selection efficiency (99 %).
- β selection efficiency (χ^2 and SI) (94 % and 84 %) which are calculated from the number of data in 2.6 MeV ($\pm$ 1 σ) ^{208}Tl γ peak which decrease when the selection is applied.
- Acceptance in reduction of ^{208}Tl decays (66 %).

Current sensitivity has not reached the level of ELEGANT VI even though exposure is limited on this analysis (96 $\rightarrow$ 26 crystals). The key of sensitivity improvement is surely low background observation.

Table 3.1: Parameter for $0\nu\beta\beta$ sensitivity of the current CANDLES III detector.

M	T	a	N_{A}	ϵ	W	μ
82.68 kg	0.167 yr	1.87×10^{-3}	6.02×10^{23} /mol	0.3	0.07807 kg/mol	5.47

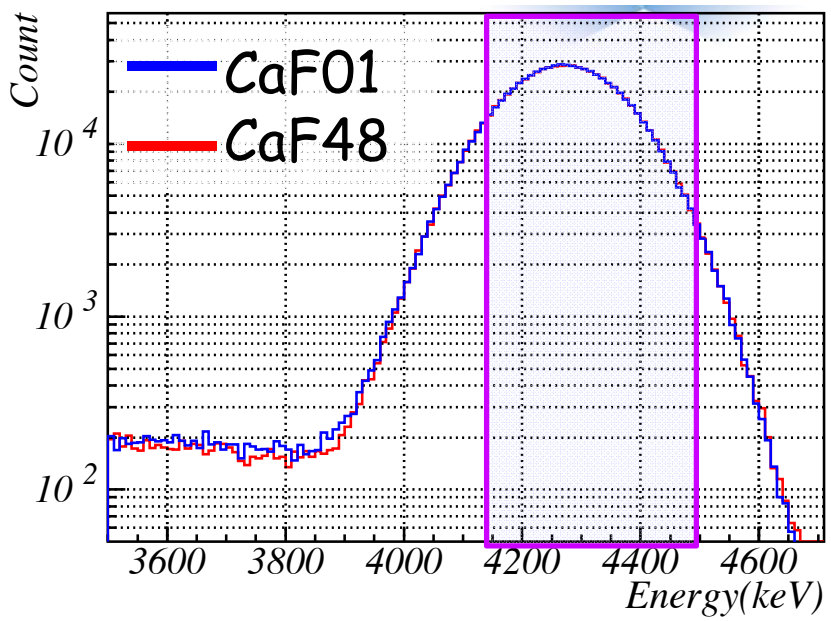

Figure 3.23: Simulated energy spectra of $0\nu\beta\beta$ events with energy resolution FWHM = 6 % at 4.27 MeV. Blue line corresponds to the spectrum of crystal #1 and red line to crystal #48. In energy region of $Q_{\beta\beta}$ - $1\sigma \sim Q_{\beta\beta}$ + 2σ (purple box), detection efficiency is estimated to be 62 %.

Chapter 4

High Energy Background Study

4.1 Background Candidate

As discussed in Chapter 3, we tried to find $0\nu\beta\beta$ signals in physics run with event selection using energy, position reconstruction and pulse shape discrimination, while we found more backgrounds than expectation in the energy region above $Q_{\beta\beta}$. We studied the origin of these backgrounds in high energy region. In Fig. 3.22, the characteristic structure of two peaks is shown. There is a clear peak around 7.5 MeV and this is the key to understand these high energy backgrounds.

Neutron capture, a nuclear reaction in which an atomic nucleus and neutrons collide and merge to form a heavier nucleus, is one of the main possibilities of high energy events. Neutron capture is accompanied by γ-ray emissions ((n,γ) reaction). There are various energies and intensities of emitted γ-rays in these reactions. Especially, iron (Fe) emits remarkable 7.631 MeV and 7.646 MeV γ-rays from (n,γ) reactions. In fact, Fe is contained in materials around the CANDLES detector. Mainly two materials can be candidates of (n,γ) background origins; a detector tank which is made of "SUS304", a type of stainless steel, and rock wall surraunding the experimental tank. Each elemental composition is given in Table 4.1.

Figure 4.1 and Figure 4.2 show the schematic views of neutron capture reaction around the detector and expected γ-ray spectra of each material considering its elemental composition. These spectra are calculated from the photon intensity of γ-rays as seen in (n,γ) reactions based on cross section [22] and chemical composition of the material. The stainless steel of the tank contains about 70 %

of Fe, 8.0 ~ 10.5 % of nickel (Ni) and 18.0 ~ 20.0 % of chromium (Cr). In the energy region above 7 MeV, Fe γ-ray emission with energy around 7.6 MeV is considered to be the main component of (n,γ) reaction. This emission can be the source of the 7.5 MeV peak. In addition, both Ni and Cr components emit high energy γ-rays (especially, 8.998 MeV of Ni and 8.884 MeV of Cr) from (n,γ) reactions. They are origins of the 9 MeV peak in energy spectra of physics runs. The wall material is solid rock of Kamioka and its chemical composition is given in [27]. As for the rock material, Fe γ-ray emission with energy around 7.6 MeV is dominant.

In conclusion, we assumed that γ-ray from (n,γ) reactions of the detector tank and the rock wall could be the origin of high energy backgrounds.

Here we have to make reference to the neutron flux in physics run. In previous research with the ^{3}He proportional counter [31], flux of thermal neutrons (with energy $E_n = 0.025$ eV), non-thermal neutrons (0.5 eV $\leq E_n \leq$ 10 MeV) and fast neutrons (0.5 MeV $\leq E_n \leq$ 10 MeV) were estimated as below,

$$\Phi_{\text{thermal}} = 8.26 \pm 0.58 \times 10^{-6} \text{ neutrons/cm}^2\text{/sec} \tag{4.1}$$

$$\Phi_{\text{non-thermal}} = 1.15 \pm 0.12 \times 10^{-5} \text{ neutrons/cm}^2\text{/sec} \tag{4.2}$$

$$\Phi_{\text{fast}} = 2.06 \pm 0.21 \times 10^{-6} \text{ neutrons/cm}^2\text{/sec.} \tag{4.3}$$

Considering that the detector tank has the surface area of 51.8 m^2, number of thermal and non-thermal neutrons incident on the tank are calculated as

$$n_{\text{thermal}} = 4.28 \pm 0.30 \text{ neutrons/sec} \tag{4.4}$$

$$n_{\text{non-thermal}} = 5.96 \pm 0.62 \text{ neutrons/sec} \tag{4.5}$$

$$n_{\text{total}} = n_{\text{thermal}} + n_{\text{non-thermal}} = 10.3 \pm 1.3 \text{ neutrons/sec.} \tag{4.6}$$

In addition, By assuming that the laboratory has a simple cylinder shape with 6 m in the floor diameter and 6 m in height, the the surface area of the rock wall is estimated to be 170 m^2. As a result, number of thermal and non-thermal neutrons incident on the rock are calculated as

$$n_{\text{thermal}} = 14 \pm 1 \text{ neutrons/sec} \tag{4.7}$$

$$n_{\text{non-thermal}} = 20 \pm 2 \text{ neutrons/sec} \tag{4.8}$$

$$n_{\text{total}} = n_{\text{thermal}} + n_{\text{non-thermal}} = 34 \pm 3 \text{ neutrons/sec.} \tag{4.9}$$

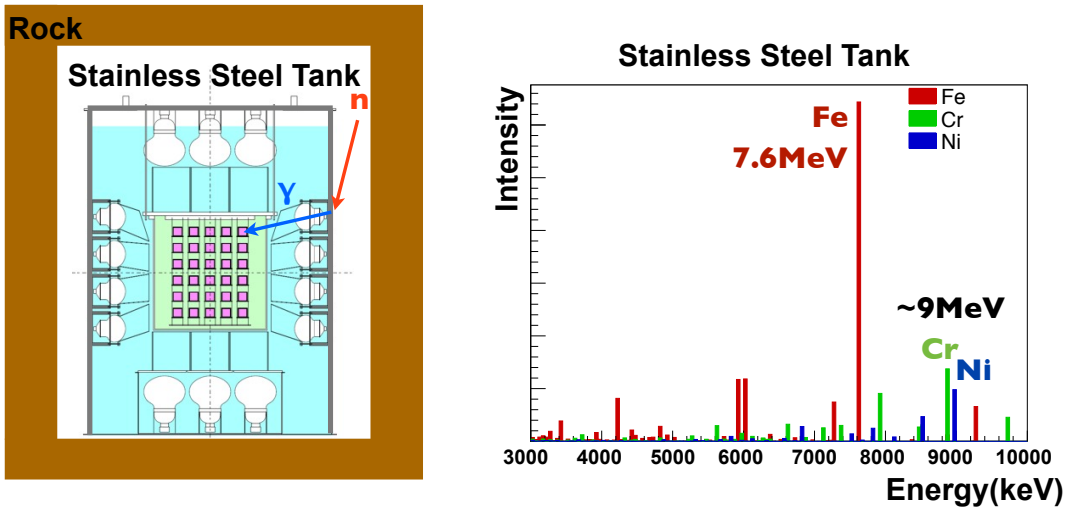

Figure 4.1: (Left) Schematic view of neutron capture at stainless steel tank. (Right) A calculated γ-ray spectrum from (n,γ) reaction in stainless steel. Cross section of each γ-ray energy is from [22] and the element composition is from [28].

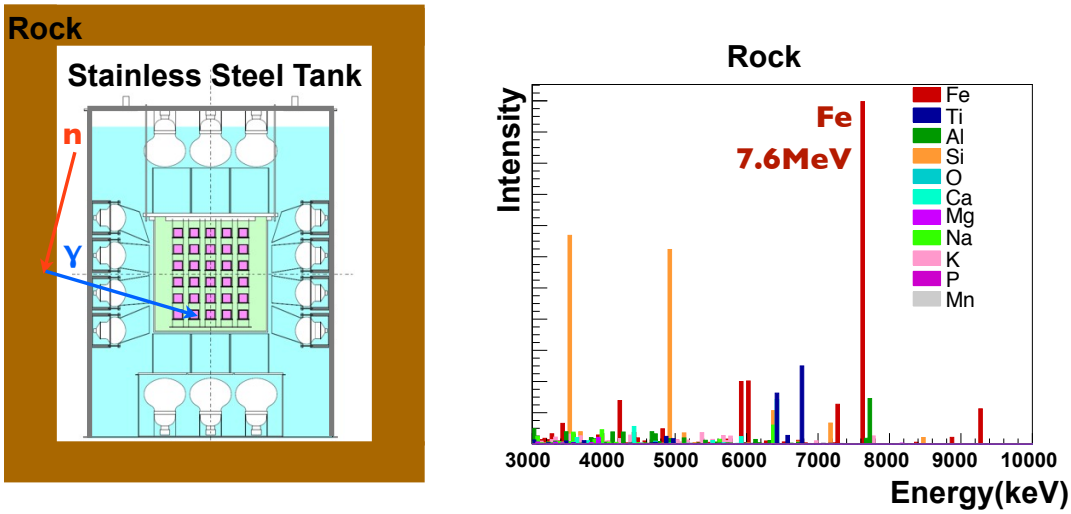

Figure 4.2: (Left) Schematic view of neutron capture at rock wall. (Right) A calculated γ-ray spectrum from (n,γ) reaction in rock wall. Cross section of each γ-ray energy is from [22] and the element composition is from [27].

Table 4.1: The elemental composition of rock in Kamioka [27] and stainless steel tank (SUS 304, [28]). Neutron capture cross section and energy for principal γ-rays from (n,γ) reaction in each element [22] are also shown in the table.

Element	Rock (%)	Tank (%)	Cross section (barns)	Energy for principal γ-rays (keV)
O	60.67		1.9×10^{-4}	
Si	18.47	< 1.00	0.172	3539, 4934
Al	10.58		0.231	1779
Na	3.90		0.530	1369, 2754
K	2.11		2.06	30, 770
Ca	1.82		0.431	1943, 6420
Fe	1.04	(66.3 - 74.0)	2.56	7631, 7646
H	0.58		0.3326	2223
C	0.29	< 0.08	3.5×10^{-3}	4945, 1262
Mg	0.28		6.7×10^{-2}	3917, 585
P	0.11	< 0.045	0.172	513
Tl	0.09		3.44	140
Mn	0.04	< 2.00	13.36	847
S	0.01	< 0.030	0.534	841, 5421
Cr		18.00 - 20.00	3.07	835, 8884
Ni		8.00 - 10.50	4.39	8998, 465, 8534

4.2 Experimental Run with ^{252}Cf Neutron Source

In order to verify the hypothesis that (n,γ) reaction is the source of backgrounds, we must understand how events appear in experimental energy spectra. In addition, we need to determine the fraction of (n,γ) origin which is necessary for designing additional background shielding. To study them, we performed neutron source run in order to generate (n,γ) reaction artificially.

4.2.1 Setup of Neutron Source Run

We used californium 252 (^{252}Cf) neutron source in order to obtain sufficient statistics of (n,γ) events in limited time scale. Figure 4.3 shows setup and photos of neutron source run. In contrast to energy calibration with the ^{88}Y source, the neutron source was set outside of the detector, between the detector tank and the rock. For comparison with energy spectra of γ-rays from the tank and the rock, the source was placed near the tank and near the rock wall with observation performed depending on the source position.

The neutron source ^{252}Cf emits a number of neutrons and γ-rays in its spontaneous fission reactions. Average energy of emitted neutrons is about 2 MeV. Prepared ^{252}Cf source had its radioactive intensity of 0.4 MBq. Three percents of decays in ^{252}Cf is spontaneous fission and 3.8 neutrons in average are emitted in the fission, which corresponded to neutron emissions as

$$n_{\text{source}} = 4.56 \times 10^4 \text{ neutrons/sec} \tag{4.10}$$

at the time of this experiment. When the neutron source was set near the rock wall, almost all of these neutrons enter the rock. Simple estimation with neutrons incident in comparison to environmental neutrons incident on the tank (4.9) indicated that neutron source run for about 6 hours would provide a statistic of neutron-induced events in one-year physics run. In order to shield unnecessary γ-rays, lead (Pb) blocks with 5 cm thickness were used.

Table 4.2 shows run list of neutron source run series.

Table 4.2: List of each neutron source run and physics run.

Run Name	Date	Run Time	Live Time
Cf run (Tank)	31st August 2014	21899 sec	20920 sec (5.8 h)
Cf run (Rock)	31st August 2014	41994 sec	40567 sec (11.3 h)
Physics Run	June ~ October 2013	5.39×10^6 sec	5.27×10^6 sec (61.0 days)

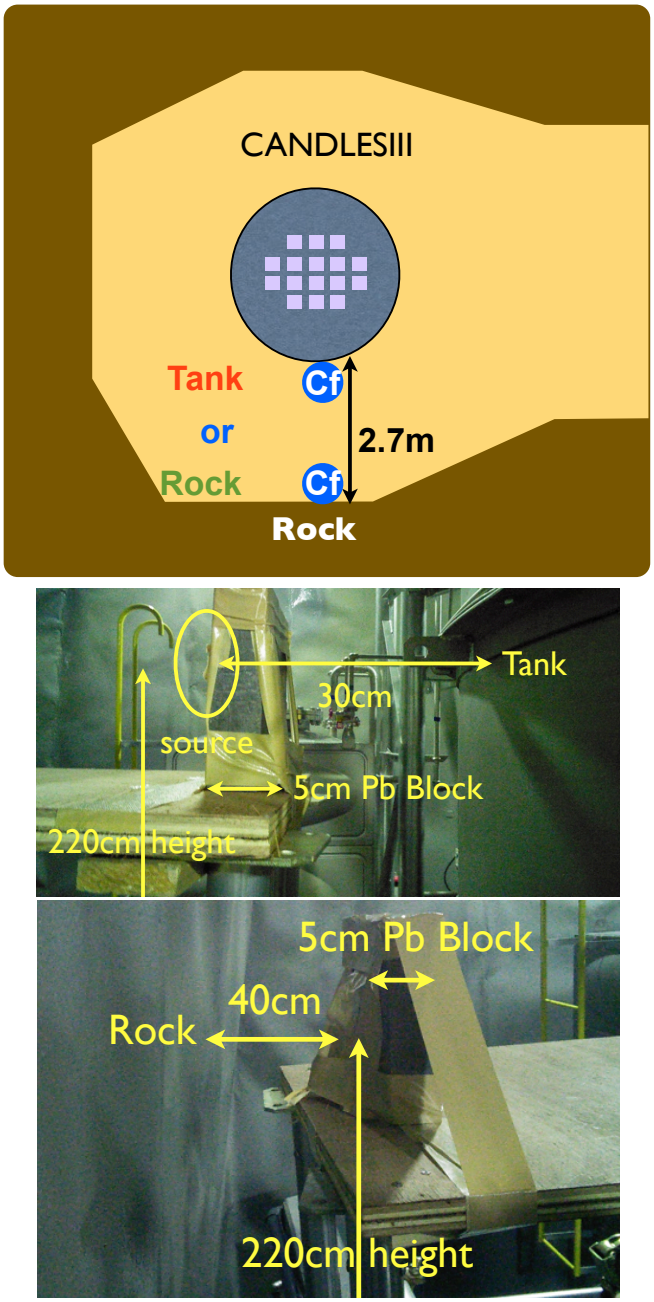

Figure 4.3: (Up) Top view of the experimental site and the layout of the setup of the Cf runs. Observation of Cf run (Rock) and Cf run (Tank) were performed individually. (Middle) A photo of the source setting near the tank. (Bottom) A photo of the source setting near the rock.

4.2.2 Energy spectra of Neutron Source Runs

Spectrum of Cf run (Tank) and that of Cf run (Rock) without normalization are shown in Fig. 4.4 and Fig. 4.5. Loose CaF_2 selection was applied in order to compare spectral shapes with physics run in this region. In addition, each source run was normalized with the number of events in the energy region above 5.5 MeV in Fig. 4.6. This figure shows energy spectrum of 61.0 days physics run in blue plots, that of Cf run (Tank) in red and that of Cf run (Rock) in green. There are lots of events in physics run in the region below 5 MeV because loose selection was also applied to physics run and ^{208}Tl β events are not rejected. We should focus on the energy region above 5.5 MeV.

We found that 7.6 MeV peak (Fe) and 9 MeV (Fe, Cr, Ni) structure from (n,γ) reactions are observed experimentally. In addition, an energy peak in 6 MeV region were found in every spectrum, which corresponded to γ-rays of 5.920 MeV and 6.019 MeV from (n,γ) reactions from Fe. From the above, spectra of neutron source runs reproduced the spectrum of physics run above 5.5 MeV.

We considered that high energy backgrounds come from γ-rays originating in (n,γ) reactions; however, in spite of different source position, there were not many gaps between two spectra of neutron source run. The tank captures more neutrons than estimated, because neutrons from the source were reflected by the rock and distributed uniformly in the laboratory. In addition, Silicon component which is shown in Fig. 4.2 could not be observed because the rock shielded 3.5 MeV and 5 MeV γ-rays. Statistics in 7.6 MeV peaks (shown in Table 4.3 as item A) shows that Cf run (rock) for about 4.3 hours could provided a statistic of neutron-induced events in one-year physics run. This result was consistent with estimation using neutron flux.

4.2.3 Components of (n,γ) Backgrounds

In the following discussion, we assume that γ-ray spectra in energy region above 7 MeV consist of two components; one is from the rock and another is from the tank. Components of (n,γ) backgrounds were estimated from the shape of each Cf run spectrum. Figure 4.7 shows calculated γ-ray spectra from (n,γ) reactions in both materials with energy resolution FWHM = 6 % at 4.27 MeV. Same data with Fig. 4.1 and 4.2 [22] are used in these spectra. Ratio of total number of events in 8 $\sim$ 10 MeV (area B) to that in 7 $\sim$ 8 MeV (area A) are used for

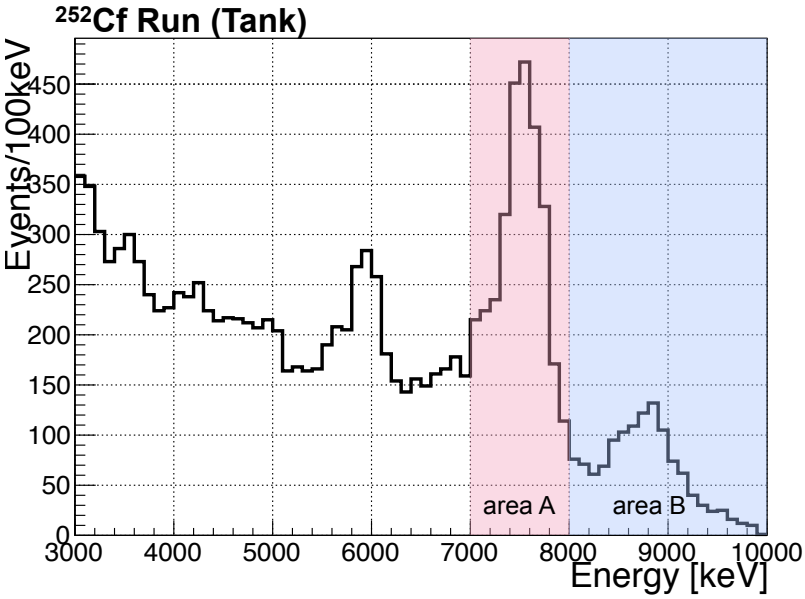

Figure 4.4: Energy spectra of Cf run (Tank) in 20920 sec observation. CaF_2 selection (see Section 3.2.2) is performed in this spectrum.

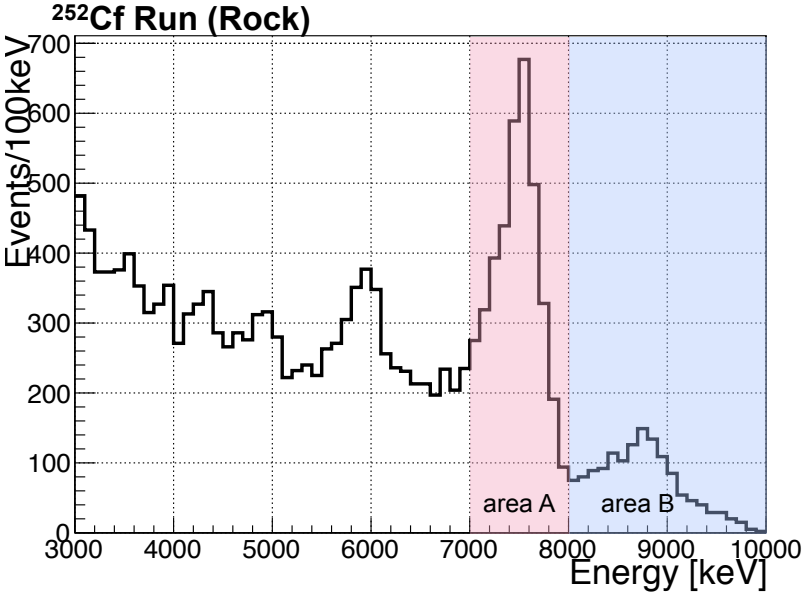

Figure 4.5: Energy spectra of Cf run (Rock) in 40567 sec observation. CaF_2 selection (see Section 3.2.2) is performed in this spectrum.

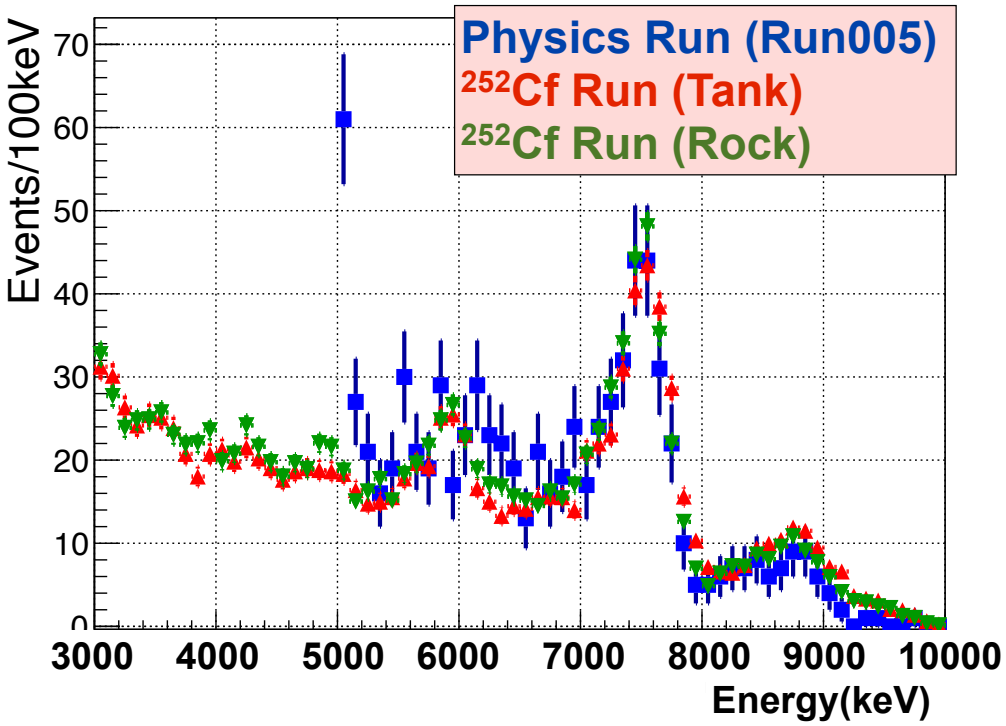

Figure 4.6: Energy spectra of physics observation (blue points) and neutron source run (red points show Cf run (Tank) and green points show Cf run (Rock)). CaF_2 selection (see Section 3.2.2) is performed in all spectra. Each source run is normalized with the number of events in the energy region above 5.5 MeV.

this calculation, because the structure of 8 $\sim$ 10 MeV is feature of the tank conponent. This ratio is named "the B/A ratio". From Fig. 4.7, the B/A ratio of (n,γ) backgrounds from the tank is 0.77, and that from the rock is 0.10.

Components of (n,γ) events of physics run and two neutron source runs are calculated by comparing their B/A ratio with values calculated from Fig. 4.7. This is shown in the equation below;

$$R = 0.77t + 0.10(1 - t),$$

$$t = \frac{R - 0.10}{0.67}, \tag{4.11}$$

where R is the observed B/A ratio and t is the component of (n,γ) backgrounds from the tank in area A. The B/A ratios and the components of backgrounds in 7.6 MeV peaks are shown in Table 4.3. We performed two Cf runs of different

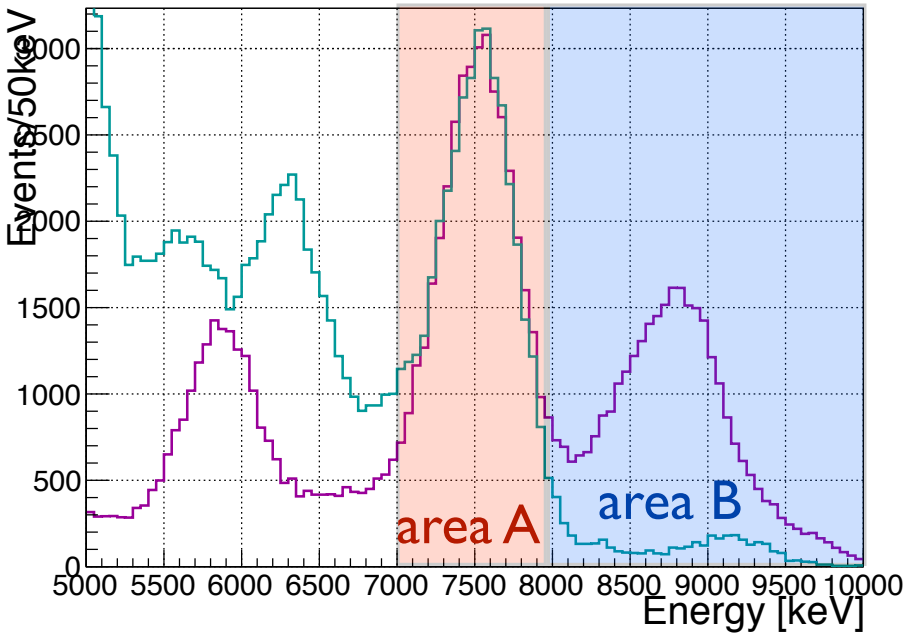

Figure 4.7: Calculated γ-ray spectra from (n,γ) reaction with energy resolution FWHM = 6 % at 4.27 MeV. neutron capture information with γ-ray energy is from [22]. Purple line shows γ-rays spectrum from (n,γ) reaction of the tank. Blue line shows γ-rays spectrum from (n,γ) of the rock.

source positions, resulting in a small difference of (n,γ) components. In physics run, about 70 % of (n,γ) backgrounds are from the rock wall, and we have to consider about shielding against γ-rays from both materials. In next section, we estimate number of (n,γ) background in CANDLES using the results of these source runs.

4.3 Simulation

By the measurement with neutron source, we found that γ-rays from neutron capture reactions were main events above $Q_{\beta\beta}$ region. Component ratios of (n,γ) reaction in 7.6 MeV, from rock or tank, were estimated from the γ-ray spectrum using database, but more accurately these should be calculated from the experimental γ-ray spectrum of only the rock component and only the tank component. However, to obtain such spectra, neutron source must be set into a mass of rock or tank with thickness of a few meter because of neutron trans-

Table 4.3: The B/A ratio and the components of backgrounds in 7.6 MeV peaks. The components in the 'database' column are estimated from B/A ratio of γ-ray spectra shown in Figure 4.7. The components in the 'γ MC' column (a) are estimated from spectra fitting with simulated spectra shown in Figure 4.10 and those in (b) are from B/A ratio of simulated spectra.

Run Name	A	B	B/A Ratio	Tank : Rock (%)		
				(database)	(γ MC (a))	(γ MC (b))
Fit range (MeV)				7 - 10	5.5 - 10	7 - 10
Cf run (Tank)	2937	1237	0.42±0.01	48±2 : 52±2	74±1 : 26±1	62±2 : 48±2
Cf run (Rock)	3803	1396	0.37±0.01	41±2 : 59±2	62±1 : 38±1	53±2 : 47±2
Physics run	243	73	0.30±0.04	31±5 : 69±5	33±2 : 67±2	41±5 : 59±5

parency. It is difficult to perform such measurement in the CANDLES laboratory.

For further understanding of (n,γ) backgrounds, we performed Monte Carlo simulation [32] instead of additional experiments. In addition, we needed information about neutron distribution in the CANDLES laboratory and in the rock wall. This was the key to understand the component ratio of (n,γ) backgrounds in physics run. Two types of simulation were needed; γ-ray simulation to obtain energy spectrum of each component and neutron generation to investigate neutron distribution.

Geometry in Monte Carlo simulation is shown in Fig. 4.8. Simulation for γ-rays was performed using database shown in Fig. 4.1 and Fig. 4.2, uniformly in rock or tank. Energy deposition in each crystal was recorded and total energy deposit in CaF_2 and in LS was obtained.

We generated the spectra correponding to the rock component and the tank component. By fitting these two simulated spectra to the experimental spectrum, the ratio of component was estimated. Energy spectrum of physics run with two simulated spectra is shown in Fig 4.9. It is noted that data in 88.1 days live time were used in this spectrum and simulated spectra were fit to the experimental spectrum in the energy range from 5.5 MeV to 10 MeV.

These estimation was performed also for ^{252}Cf source runs which are shown

in Fig. 4.10. The ratio of the components in 7.6 MeV of each run are shown in (γ MC a) column of Table 4.3. With γ-ray Monte Carlo estimation, the rock component has a tendency to be estimated lower than database estimation. This was because the number of events in 9 MeV region in the tank component with simulation was estimated fewer than those with database. In addition, fit range of simulated spectrum covered the structure of 6 MeV. The spectrum of the tank component had clear single peak in 6 MeV, and the experimental spectra of ^{252}Cf runs also had the clear peak. Therefore, the ratio of the component was estimated with simulation more correctly, and especially in Cf runs, the tank component seemed to be remarkably stronger than estimation with databese. On the other hand, both of estimation show that the rock component in physics run is higher than that in neutron source run with setting the source near the rock wall. In order to confirm the difference between fit range, calculation using the B/A ratios of simulated spectra was performed and shown in (γ MC b) column of Table 4.3. Although the rock component was estimated lower than database, the difference between Cf runs and physics run was reduced.

The calculated ratio of the two components Tank / Total in 7.6 MeV was calculated as $0.33^{+0.13}_{-0.05}$. The ratio of the components in $Q_{\beta\beta}$ region ($\pm$ 1 σ) was calculated as $0.20^{+0.15}_{-0.05}$. As estimated above, γ-rays from the rock wall are considered as the main component of backgrounds.

Next we performed neutron generation for understanding neutron capture and γ-ray distribution. Geometry in this simulation was same as γ-ray simulation. In this study, three types of neutrons were generated uniformly in thr rock wall. The types were thermal (0.025 eV), non-thermal (0.1 eV $\sim$ 10 MeV) and fast neutrons (0.1 MeV $\sim$ 10 MeV). For every type, 10^6 of perticles were generated. Then numbers of neutron captures in the rock and in the tank were recorded. As a result, neutron captures were calculated as (1.21 $\pm$ 0.10) $\times$ 10^7 /day in the rock and (2.53 $\pm$ 0.21) $\times$ 10^5 /day in the tank. That correspond to numbers of γ-rays emission as (2.45 $\pm$ 0.20) $\times$ 10^7 /day in the rock and (4.30 $\pm$ 0.35) $\times$ 10^5 /day in the tank, calculated from number of γ-rays per one (n, γ) reactions is 2.04 in the rock and 1.66 in the tank. These show that the rock wall was higher level γ-ray emitter than the tank in physics run. By contrast, considering energy deposition in crystals and event cut condition, the ratio of components Tank : Rock in 5.5 MeV $\sim$ 10 MeV region calculated from this neutron simulation was 4.4 : 5.6, which showed that the rock component was smaller than the other estimation. This might come from the small thickness settings of the rock wall in this study (1 m). Several meters of the rock wall will

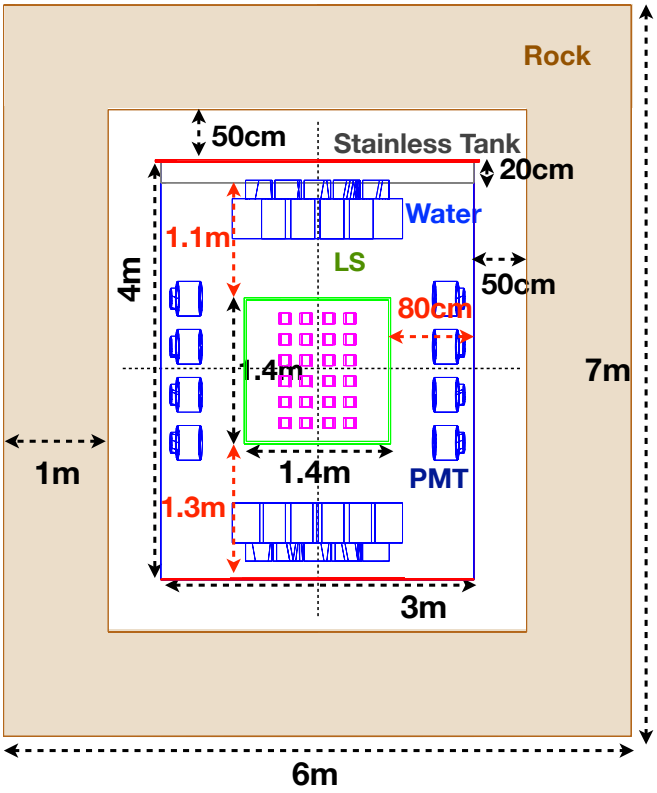

Figure 4.8: Geometry in Monte Carlo simulation.

be suitable for real geometry and enlarge the rock component.

4.4 Background Estimation

We found that γ-rays from (n,γ) reactions in materials around the detector are the main origin of $Q_{\beta\beta}$ backgrounds. We focus on energy spectrum with $0\nu\beta\beta$ selection. It is noted that ^{212}Bi-^{212}Po cut and ^{208}Tl cut are performed in this selection but ^{208}Tl and (n, γ) background still remain. Figure 4.11 shows energy spectrum of physics run in blue line and that of Cf run (Rock) in green line with CaF_2 selection in order to study current amounts of background. Cf run is normalized with number of events in the energy region above 5.5 MeV. Table 4.4 shows background estimation of the run in the $Q_{\beta\beta}$ energy region. Six events were observed in physics run. In this region, normalized spectrum of ^{252}Cf source run, corresponding to current (n,γ) backgrounds, were estimated

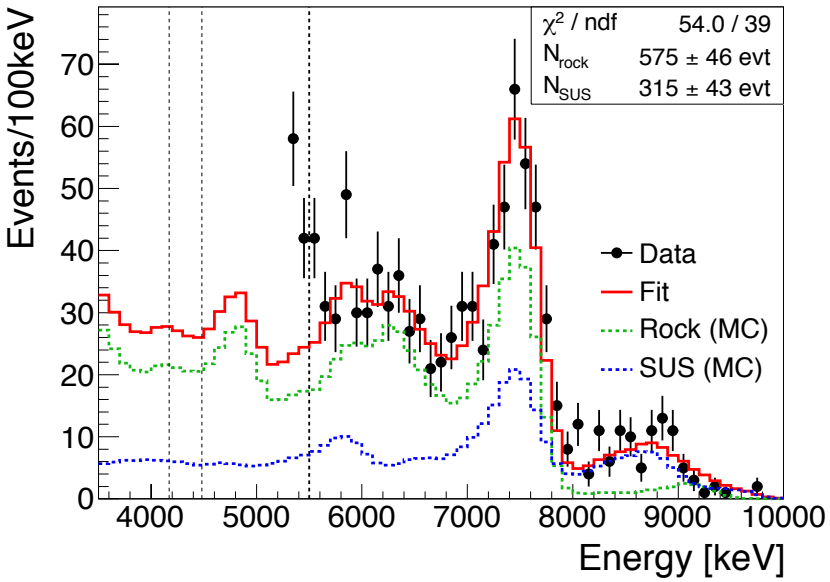

Figure 4.9: Energy spectrum of physics run in 88.1 days live time (black circle) with the most suitable simulated spectrum fitting (red solid line). Blue dotted line shows the stainless steel tank component in fitting spectrum and green dotted line shows the rock component.

as 3 ± 1 events. Number of ^{208}Tl background was estimated as about 1. This shows that (n,γ) reactions of the rock and the tank could be major origins of current background in $Q_{\beta\beta}$ region. However, studying contribution of (n,γ) backgrounds with high statistics is necessary. Next we focus on energy spectrum of physics run with loose CaF_2 selection in order to confirm the consistency of background rate.

Physics events with loose cut include backgrounds from ^{212}Bi-^{212}Po sequential decays, ^{208}Tl $\beta + \gamma$ and (n,γ) reactions. Number of sequential decays and that of ^{208}Tl decays were estimated to pick up events with pulse shape discrimination and timing analysis as shown in Section 3.2. We should consider present low ^{208}Tl reduction (selection) efficiency (60%). In order to count ^{208}Tl events after the corresponding selection, spectrum with ^{208}Tl selection and spectrum without ^{208}Tl selection were compared and ^{208}Tl spectrum was obtained (shown in Fig. 4.12(Down)). This spectrum should correspond to 60% of all ^{208}Tl events. Therefore, number of remaining 40% was estimated from this spectrum. In addition, number of (n, γ) backgrounds was estimated from energy spectrum of ^{252}Cf source run normalized with the number of events in the

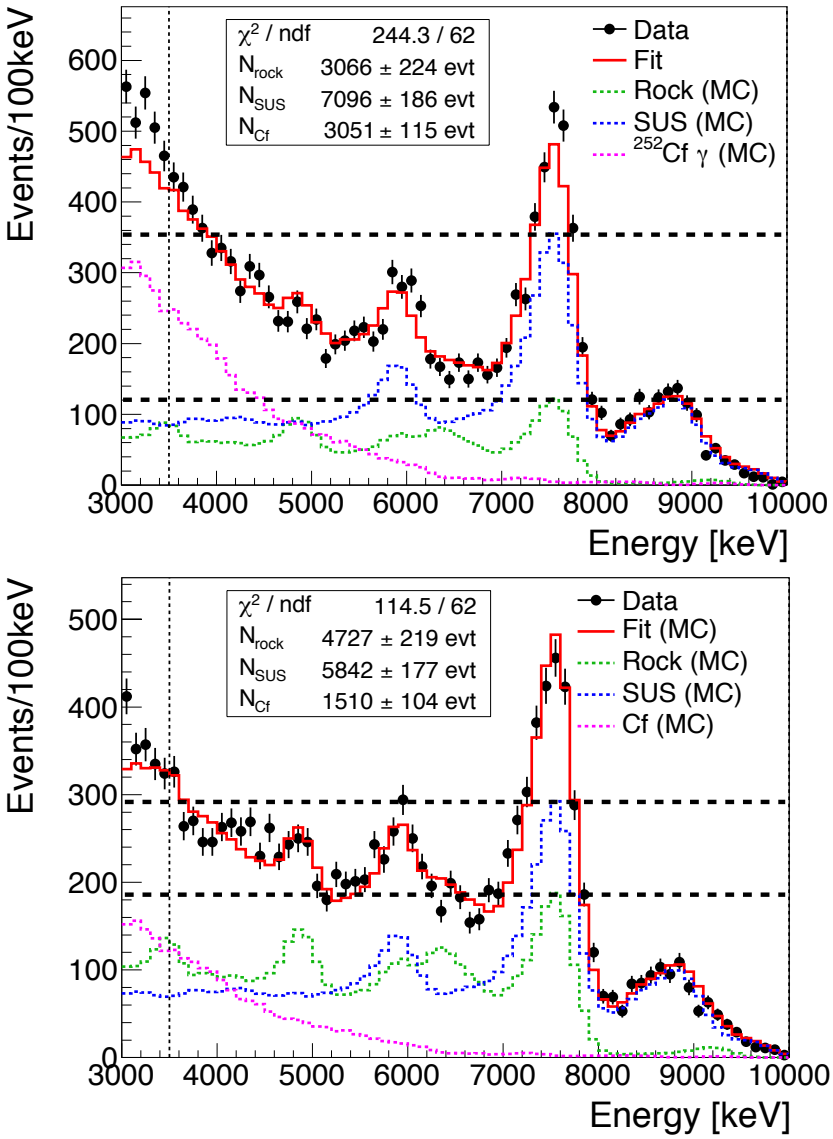

Figure 4.10: Energy spectrum of ^{252}Cf source runs in same format with Fig. 4.9, with additional simulated spectrum of γ-rays from ^{252}Cf source. (purple dotted line). (Up) Cf run (Tank). (Down) Cf run (Rock).

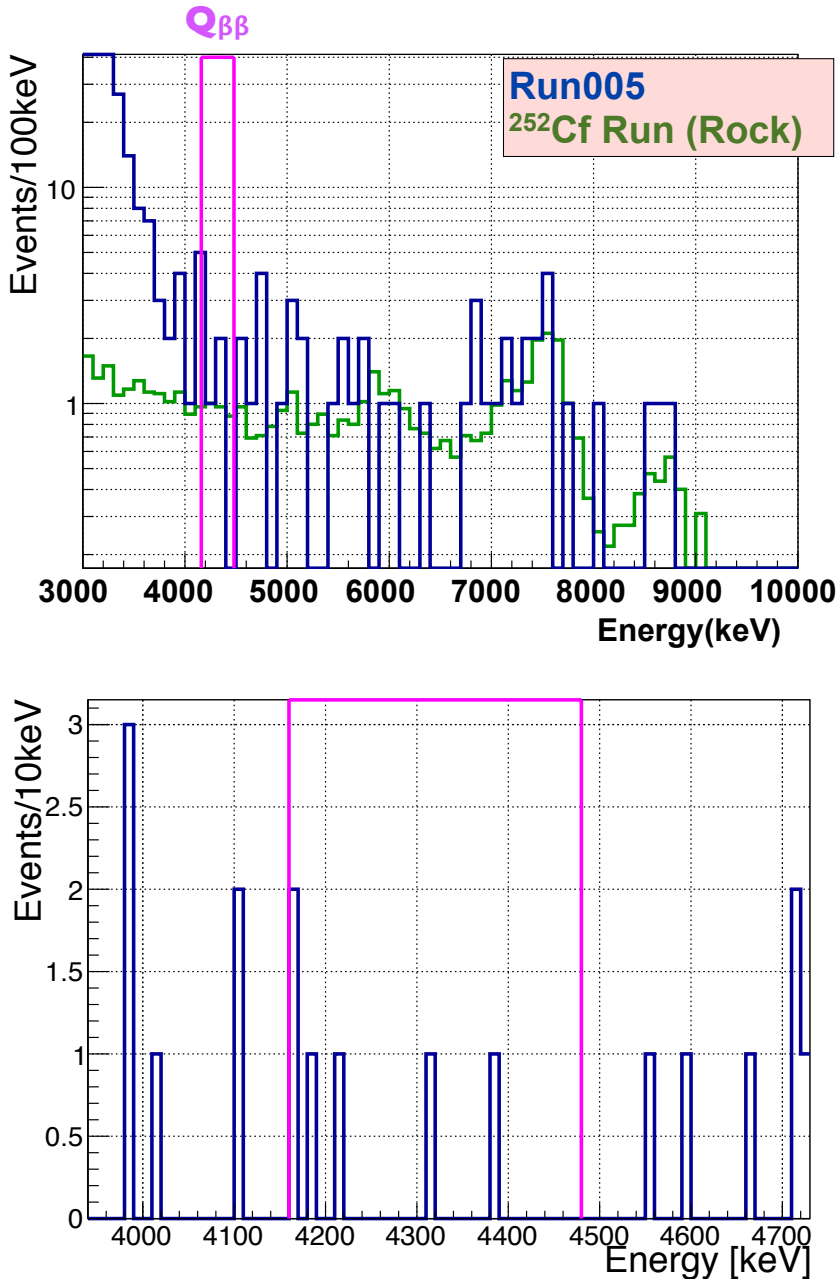

Figure 4.11: (Up) Energy spectra of the physics observation (blue line) and Cf run (Rock) (green line), with performing $0\nu\beta\beta$ selection (see Section 3.2.2) in both spectra. Cf run is normalized with the number of events in the energy region above 5.5 MeV. (Down) Zoomed energy spectra of the physics observation in $Q_{\beta\beta}$ region. Pink box shows the energy region $Q_{\beta\beta}(^{48}\mathrm{Ca})$.

Table 4.4: Background estimation of physics run in $Q_{\beta\beta}$ energy region.

Live time	61.0 days
Mass of target	82.68 kg (26 crystals)
Energy window	4.16 - 4.48 MeV (-1 $\sigma \sim 2\ \sigma$)
Observed events	6
^{208}Tl estimated backgrounds	$\sim$1
(n,γ) estimated backgrounds	3 ± 0.6

energy region above 5.5 MeV. All background estimation are shown in Table 4.5 and corresponding energy spectra are shown in Fig. 4.12. All number of events in $Q_{\beta\beta}$ region with loose CaF_2 selection, Bi-Po cut and ^{208}Tl cut were 149 ± 12 events / 96 crystals / 61.0 days. On the other hand, events of remaining backgrounds were estimated as 132 ± 10 events / 96 crystals / 61.0 days, including these two types of backgrounds which cannot be removed analytically, 62 ± 10 events of remaining ^{208}Tl backgrounds and 70 ± 3 events of (n,γ) backgrounds. The number of remaining ^{208}Tl backgrounds were estimated from energy spectra with Bi-Po cut and "Tl selection" which figures events that are removed by Tl cut. Removed ^{208}Tl events were calculated as 103 ± 16 events in $Q_{\beta\beta}$ region with subtracting energy spectrum before applying Tl selection (normalized with the number of 2.6 MeV events) from the spectrum after Tl selection. Here we estimated that the number of remaining events were about 0.6 times as much as the number of removed events, which was calculated as 62 ± 10 events. The number of (n,γ) backgrounds were estimated as 70 ± 3 events from energy spectrum of Cf run (Rock) normalized with the number of events in the energy region above 5.5 MeV. In this study, events in $Q_{\beta\beta}$ were found to be consistent with assumed backgrounds.

This study shows that main backgrounds in $Q_{\beta\beta}$ region are γ-rays from neutron capture reactions at surrounding materials of the detector. These are the forms of γ-rays that is difficult to remove analytically. On the other hand, these background are from outside of the detector. Therefore, sufficient shieldings against γ-rays and neutrons is expected to be effective for background reduction.

Table 4.5: Contribution of remaining backgrounds (^{212}Bi-^{212}Po, ^{208}Tl, neutron capture) in physics run in $Q_{\beta\beta}$ energy region (4.16 ~ 4.48 MeV).

Cut condition	counts / 96 crystals / 61 days
LS cut	1791 ± 42
+ Bi-Po cut	369 ± 19
+ Tl cut	149 ± 12
Remaining ^{208}Tl estimated	62 ± 10
(n,γ) estimated	70 ± 3
Total estimated background	132 ± 10

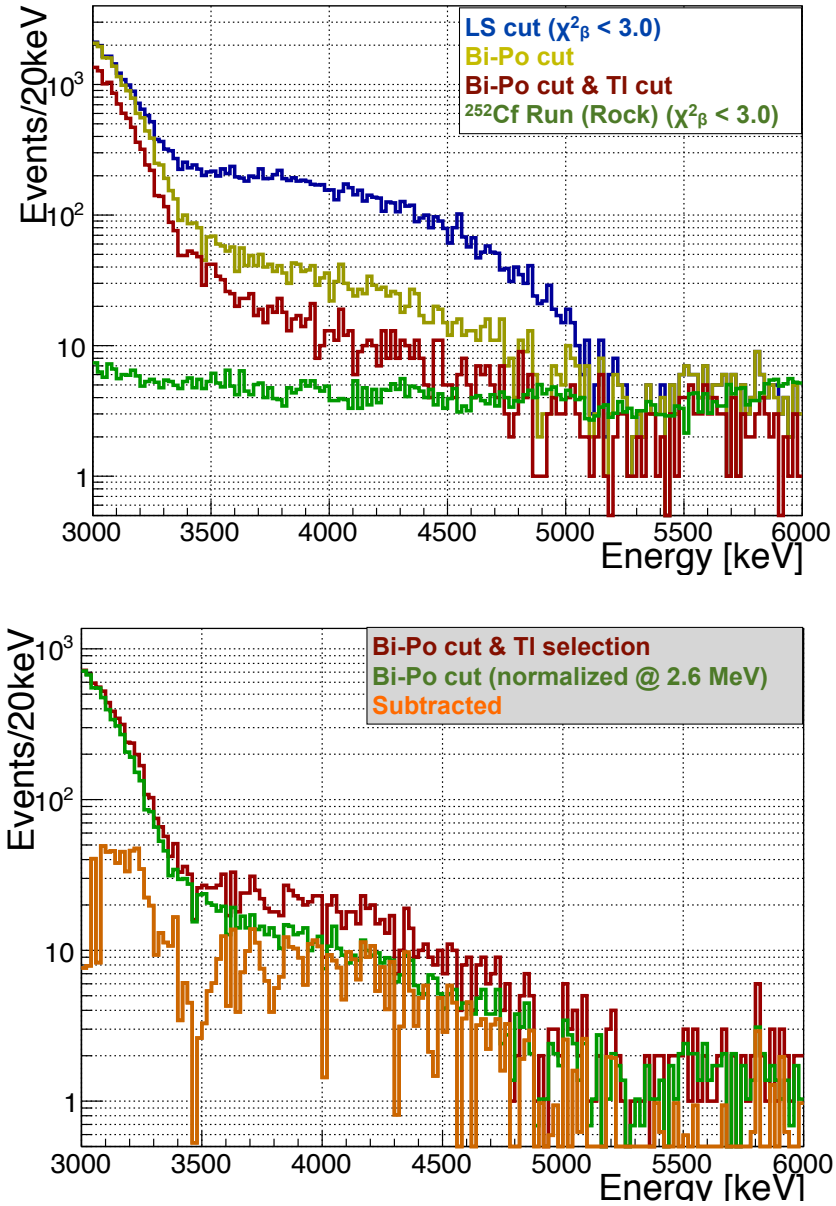

Figure 4.12: (Up) Energy spectra of physics observation and backgrounds reduction (^{212}Bi-^{212}Po, ^{208}Tl) with performing CaF_2 selection (see Section 3.2.2) in every spectrum. (Down) Energy spectra for calculating contribution of ^{208}Tl backgrounds remaining after ^{208}Tl cut.

Chapter 5

Prospect

5.1 Background Reduction

Additional passive shieldings

As the results so far, main background above $Q_{\beta\beta}$ region was found to be γ-rays from neutron capture reactions at the rock and tank materials, whose event rate was estimated to be 3 ± 0.6 events / 61 days / 26 crystals. This rate corresponds to 66 ± 12 events/year in all 96 crystals. Monte Carlo simulation gives the ratio of (n,γ) backgrounds from the tank to that from total in $Q_{\beta\beta}$ region as about $0.20^{+0.15}_{-0.05}$ (see Sec. 4.3).

As described in Sec. 1.3, the most effective strategy to improve sensitive for $0\nu\beta\beta$ search is to perform zero background measurement. Therefore, we aim to reduce total backgrounds rate to be 0 events/year level. The realistic target of (n,γ) background rate is set to be about 0.5 events/year in both the rock component and the tank component, 1 events/year in total. The rock component and the tank component must be reduced to 0.01 and 0.03 of current level, respectively.

The rock component of (n,γ) background can be reduced by using lead (Pb) shielding. Required thickness of Pb to achieve 0.5 events/year background level can be estimated from the mass attenuation coefficient shown in Fig. 5.1 [33]. For example, the coefficient for γ-rays at 4 MeV is 4.2×10^2 cm^2/g, which corresponds to the attenuation length of 2.1 cm. This shows that the Pb shielding with the thickness of 10 cm attenuates the intensity of γ-rays with the energy around $Q_{\beta\beta}$ into about 0.009. In addition, γ-rays in the energy higher than $Q_{\beta\beta}$

(7.6 MeV from Fe, 9 MeV from Cr, Ni and more) can be attenuated by Pb better compared to 4 MeV, because attenuation coefficients are slightly larger than that of $Q_{\beta\beta}$. Therefore, Pb with 10 cm thickness can have desired performance for shielding (reduction of the rock component into 1 %).

Incidentally, Pb emits mainly 7.368 MeV γ-rays from (n,γ) reactions, but neutron capture cross section of Pb is 0.154 barns which is significantly smaller than that of Fe (2.6 barns) [22]. This cross section indicates that effects of neutron capture in Pb shields is much smaller than those in the tank. Table 5.1 shows values of attenuation length of 10 MeV γ-ray and neutron in Fe or Pb. Attenuation length of γ-ray is calculated as

$$L_G = \frac{1}{\mu\rho}, \tag{5.1}$$

where $\mu(\mathrm{cm}^2/\mathrm{g})$ in this equation is mass attenuation coefficient for γ-ray and $\rho(\mathrm{g/cm}^3)$ is mass density of material. On the other hand, attenuation length of neutron is calculated as

$$L_N = \frac{1}{\sigma_N n} = \frac{A}{\sigma_N N_A \rho}, \tag{5.2}$$

where $\sigma_N(\mathrm{barn}(10^{-24}\mathrm{cm}^2))$ is neutron capture cross section, and $n(\mathrm{atom/cm}^3) = \frac{N_A \times \rho}{A}$ is atomic density which is calculated from Avogadro constant $N_A(=6.02\times 10^{23}\mathrm{atom/mol})$, atomic number$A$(g/mol) and mass density $\rho(\mathrm{g/cm}^3)$. The Pb shielding and the tank emit γ-rays from (n,γ) reactions but attenuate these rays for themselves. Amounts of γ-rays from (n,γ) entering into the detector is proportional to R = $\frac{L_G}{L_N}$. When the detector is simply assumed as a spherical object and other constructs have uniform thickness, this background problem is simplified as a one-dimensional problem. Intensity factor of γ-rays from the tank into the detector is calculated as

$$P_{\mathrm{tank}} = \int_0^{x_0} R_{\mathrm{tank}} e^{-x} dx = R_{\mathrm{tank}}(1-e^{-x_0}) = 0.932\times(1-0.91) = 0.0839, \tag{5.3}$$

where x_0 correspnds to the thickness of the tank (as 4 mm) with a unit of L_G, which is calculated as $x_0 = \frac{0.4}{4.242} = 0.0943$. On the other hand, intensity factor of γ-rays from the Pb shieldings into the detector is calculated as

$$P_{\mathrm{Pb}} = \int_{x_0}^{\infty} R_{\mathrm{Pb}} e^{-x} dx = R_{\mathrm{Pb}} e^{-x_0} = 0.009 \times 0.91 = 0.0082, \tag{5.4}$$

when shielding has sufficiently thick enough to absorb γ-rays from outside. From calculation above, effects of neutron capture in Pb shields is about 10% of those in the tank at most.

Table 5.1: Attenuation length of γ-ray with high energy and neutron in material (Fe, Pb and rock)

	Fe	Pb	Ikenoyama [27]	Ref.
Mass attenuation coefficient for 10 MeV γ-rays [μ(cm^2/g)]	0.02994	0.04972	0.0223	[33]
Density [ρ(g/cm^3)]	7.874	11.35	2.70	[30]
Neutron capture cross section [σ_N(barn(10^{-24}cm^2))]	2.59	0.154	0.165	[22]
Atomic weight [A(g/mol)]	55.845	207.2	20.42	[30]
Avogadro constant [N_A(atom/mol)]	6.02×10^{23}			[30]
Attenuation length of 10 MeV γ-rays [L_G(cm)]	4.242	1.772	16.6	
Attenuation length of neutron [L_N(cm)]	4.549	196.9	76.1	
$R = L_G/L_N$	0.932	0.009	0.218	

From the point of strength of the concrete foundation and hardness of Pb, the top part of the Pb shielding should be designed as light as minimum necessary. Furthermore, γ-rays which enter crystal modules horizontally should be the major component because the water thickness distribution on the side of the LS tank (0.4 $\sim$ 0.8 m) is thinner than that of the top and the bottom (0.6 $\sim$ 1.3 m) as shown in Fig. 5.2. Attenuation length for γ-rays of water (H_2O), calculated from the mass attenuation coefficient (Fig. 5.1(bottom)), is 29 cm at 4 MeV and 45 cm at 10 MeV.

In order to design shielding in detail, we examined which surface of the tank (top, bottom and side) γ-rays pass through into the detector with Monte Carlo simulation [34]. As a result, the ratio of γ-rays passage is Top : Bottom : Side = 1 : 1 : 16, which shows that the side component of γ-rays is large compared to the actual surface area ratio of tank (Top : Bottom : Side = 1 : 1 : 5.3).

Consequently, a part of the side covering, the height of 1 m $\sim$ 3 m which is the same height as the internal LS tank, should be designed thicker in order to improve the shield efficiency. From discussion above, we determined each thickness of Pb as below: 7 cm for a top part (5.6 t), 10 cm for a bottom part (8.0 t) and 10 cm for a side part with 2 cm addition in the height of 1 m $\sim$ 3 m (50 t in total).

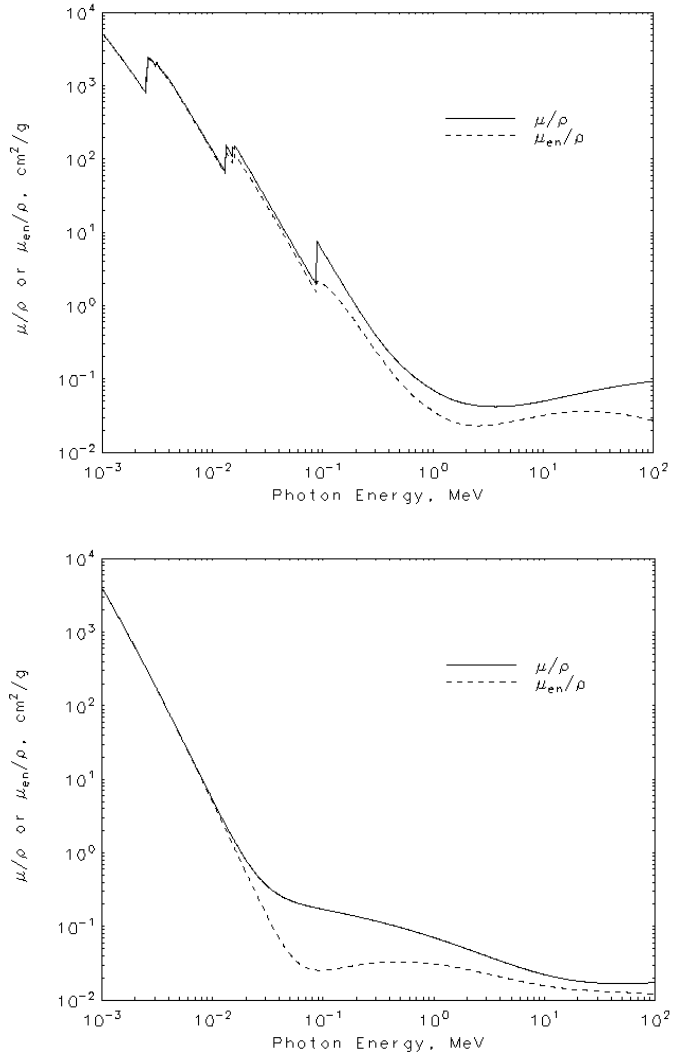

Figure 5.1: The mass attenuation coefficient (solid line) and the mass energy-absorption coefficient (dashed line) of Pb (top) and H_2O (bottom), as a function of γ-ray energy. [33]

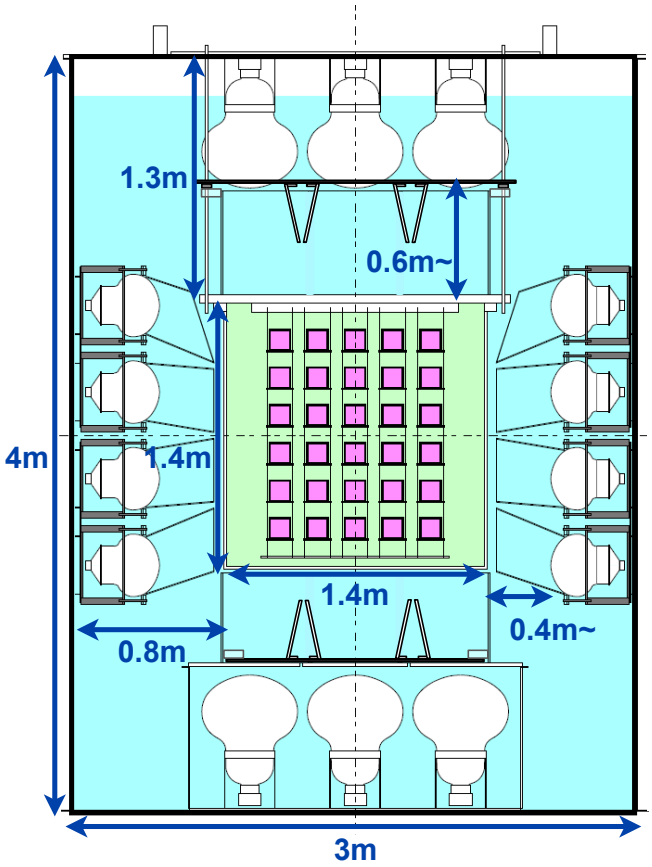

Figure 5.2: The size of the water tank, the LS tank and the water layer in CANDLES III.

Backgrounds from the tank can be reduced by shielding neutrons which enter into the tank material. The isotopes which have a high neutron capture cross section, for example, boron (^{10}B 19.9 % in natural abundance) and cadmium (^{113}Cd, 12.2 % in natural abundance), are often used to absorb neutrons. For the purpose of (n,γ) background reduction, using the isotopes with γ-ray emission is inadequate. By contrast, ^{10}B emits α-rays from (n,α) reactions with thermal neutron cross section of 3837 barns [35], which do not cause any problems. Therefore, boron neutron absorbers are suittable for our purpose. We select silicone rubber sheet containing 40 wt% of boron carbide (B_4C) as neutron absorber, which has the highest boron content of all materials commercially available. Besides thermal neutrons from the outside of the detector, non-thermal neutrons which are thermalized by water layer of the inner detector should be

reduced. This requirement can be satisfied to attach the sheets of the B absorber to both the outside and the inside of the detector so as to enclose the stainless steel and the Pb shielding.

Required thickness of the absorber to achieve 0.5 events/year background level was estimated by comparing the number of neutron captures in stainless steel with each thickness from Monte Carlo simulation. We found that the sheet with 4 mm thickness is sufficient for target background level. and a further thickness does not improve neutron reduction effect because of high transmission of non-thermal neutrons.

We designed additional passive shield (shown in Fig. 5.4) based on the discussion above. For the top and side surface of the detector, the B absorber sheet is attached on the inside of the stainless tank and the Pb block with B absorber is established on the outside. For the bottom of the detector, to avoid the process for lifting up the tank, the waterproofed Pb block is installed into the tank. Figure 5.3 shows expected (n,γ) background rate with additional shieldings. We expect that (n,γ) backgrounds are reduced to less than 1 events/year with additional shield. We plan to install the shield in 2015.

^{208}Tl reduction

Signals of ^{208}Tl β decays still remain after event selection around $Q_{\beta\beta}$. Some of ^{208}Tl events can be removed using time coincidence method between parent ^{212}Bi α decays and daughter ^{208}Tl β decays. Because of relatively high accidental coincidence, the rejection efficiency for ^{208}Tl is only 60 %. Two approaches are considered in order to decreace accidental events.

- Improvement of pulse shape discrimination is necessary. Better α discrimination with β + LS events will determine prompt ^{212}Bi signals accurately.
- Accidental events are caused by external backgrounds. Additional passive shieldings which are previously mentioned can reduce these backgrounds.

Reduction of accidental event rate can expand the coincidence time, which improves the ^{208}Tl reduction efficiency.

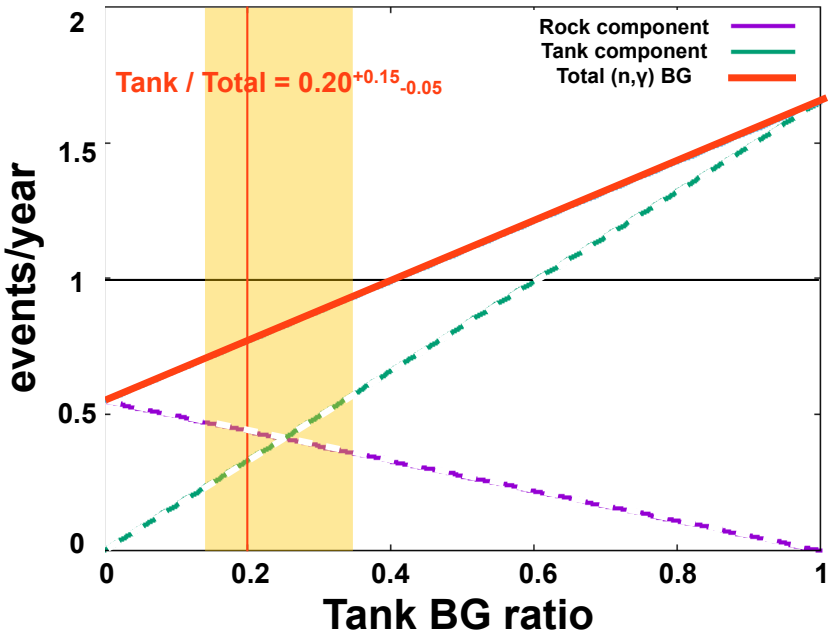

Figure 5.3: Expected background rate with additional shieldings. The horizontal axis means the ratio of (n,γ) backgrounds from the tank to that from total in $Q_{\beta\beta}$ region and orange area shows the current estimated ratio. A red thick line shows total background for each the tank component ratio. In the range of the estimated background ratio, the amount of background with 66 ± 12 events/year will be reduced to less than 0.95 events/year with additional shieldings.

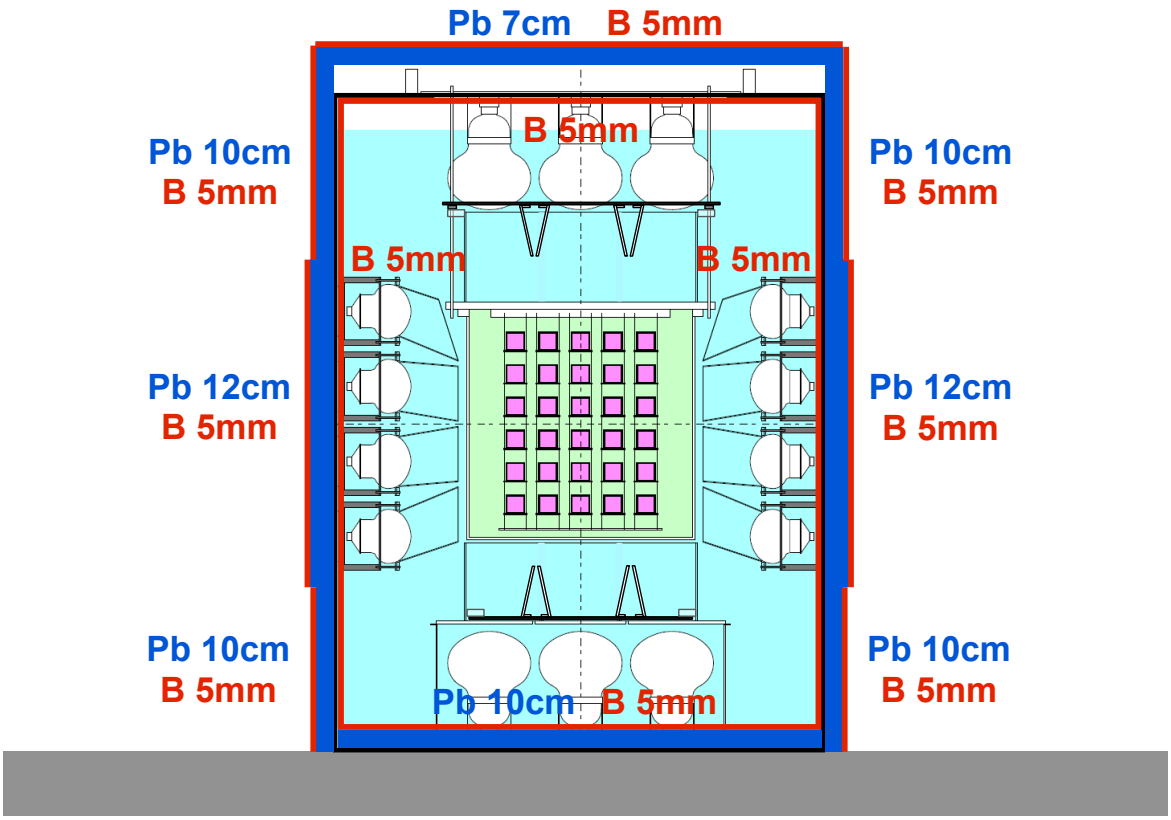

Figure 5.4: Outline of additional passive shield.

5.2 Improvement of energy resolution

Energy resolution mainly depends on photon counting statistics. In addition, large number of photoelectrons leads better pulse shape discrimination. Increasing the number of observed photoelectrons is an important key to improve resolution and pulse shape discrimination, and therefore upgrades of the detector are now being performed.

- Cooling system

  The light yield of CaF_2(Pure) scintillation increases as temperature decreases [36]. Temperature dependence of light yield were studied and we confirmed that light output of the scintillator increases about 2 % by lowering temperature by 1°C [37]. Temperature of the CANDLES III laboratory had been controled in around 18 ~ 20°C, and we installed cooling system in May 2014. We plan to cool down the detector by 2°C. If we achieve this, the light yield is expected to be improved by 30 %.

- Geomagnetic cancellation coil

  In CANDLES III, 62 large PMTs (13 inch's and 20 inch's) are used. These large phototubes are influenced by geomagnetism and their performance of photoelectron collection gets worse. The deterioration of photoelectron collection efficiency leads worse energy resolution. Geomagnetic cancellation coil have been installed and we confirmed that light collection was improved to increase by about 30 %. In addition, as shown in Fig. 5.5, improved PMT performance could suppress the distortion of position reconstruction.

The number of photon statistics can be improved by about 70 % in total using in these upgrades, which leads improvement of energy resolution from FWHM ~ 6 % to ~ 4.6 % at $Q_{\beta\beta}$.

5.3 Expected sensitivity

Currently 6 events are observed as backgrounds in 61 days physics run. With hardware improvement of shieldings, we aim for background reduction as less than 1 events per year. If we achieve one year measurement with less than 1

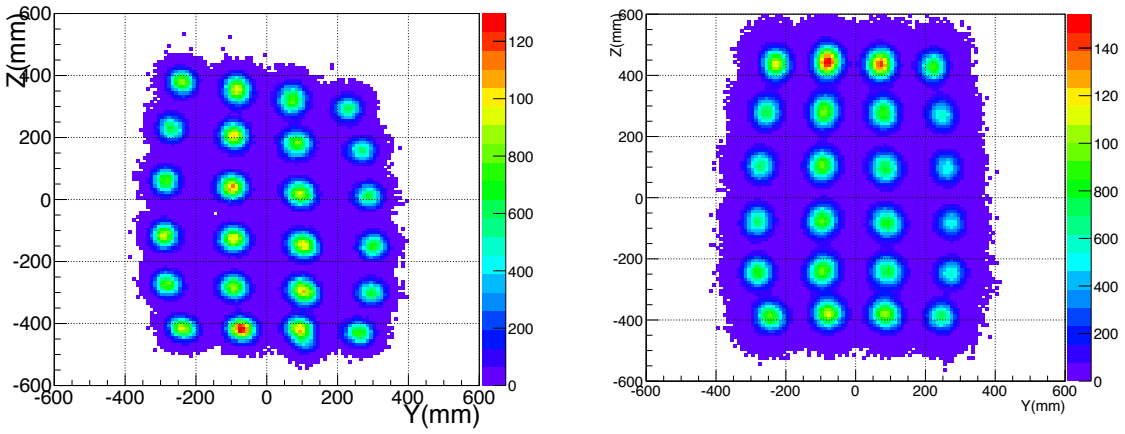

Figure 5.5: Position reconstruction in y-z axis without installing geomagnetic cancellation coil (left) and with the coil (right). Photoelectron collection efficiency of each PMT especially on the top was improved, which leads better position reconstruction.

event observation, half-life sensitivity of the detector is calculated using equation (3.5) using the Feldman-Cousins rule supposed that 1 event is expected as background, as below,

$$T^{0\nu}_{1/2}(^{48}\mathrm{Ca}) > 7.4 \times 10^{22}\ \mathrm{yr}\ (26\ \mathrm{crystals},\ 90\ \%\ \mathrm{C.L.}), \tag{5.5}$$

$$T^{0\nu}_{1/2}(^{48}\mathrm{Ca}) > 2.7 \times 10^{23}\ \mathrm{yr}\ (96\ \mathrm{crystals},\ 90\ \%\ \mathrm{C.L.}). \tag{5.6}$$

Sensitivity estimation about 0 background in one year measurement is calculated as,

$$T^{0\nu}_{1/2}(^{48}\mathrm{Ca}) > 1.0 \times 10^{23}\ \mathrm{yr}\ (26\ \mathrm{crystals},\ 90\ \%\ \mathrm{C.L.}), \tag{5.7}$$

$$T^{0\nu}_{1/2}(^{48}\mathrm{Ca}) > 3.8 \times 10^{23}\ \mathrm{yr}\ (96\ \mathrm{crystals},\ 90\ \%\ \mathrm{C.L.}). \tag{5.8}$$

In addition, multi-year measurement is shown in Fig. 5.6. For dashed lines in this figure, events are summed totally in measurement term assuming that event rate is 1 events / year (for example, 3 events are expected in 3-year measurement), and all these events are regarded as background. In the calculation,

the ditection efficiency ϵ is set to 0.3 as same value as estimated in chapter 3. This efficiency improvement in each factor is estimated as below.

- Better energy resolution leads expansion of energy window for $0\nu\beta\beta$ search. The efficiency based on crystal (calculated as 62 % in energy window of -1$\sigma \sim 2\sigma$) is estimated to be 74 % in the expanded window of -2$\sigma \sim 3\sigma$.

- Improvement of pulse shape discrimination and background reduction using the Pb shielding are expected to reduce accidental events in ^{212}Bi Q_α region on time coincidence method for ^{208}Tl background reduction. In addition, better energy resolution can make energy window for ^{212}Bi Q_α more shorter. This noise reduction shortens dead time, and thus data acceptance rate (= detection efficiency) is expected to be improved from 66 % to 95 %.

- Improvement of pulse shape discrimination will make total β selection efficiency (χ^2 and SI) as almost 95 %.

For applying these improvements, in coarse estimation, total detection efficiency ϵ is expected to be 0.7. Sensitivity estimation about 0 background measurement with this efficiency and 96 crystals using the parameter shown in Table 5.2 is calculated as

$$T^{0\nu}_{1/2}(^{48}\mathrm{Ca}) > 8.9 \times 10^{23} \text{ yr (90 \% C.L.)}, \tag{5.9}$$

which shows that sensitivity will achieve $\sim 10^{24}$ yr for $1 \sim 2$ years measurement.

As described above, CANDLES III will give the most stringent experimental limit for $0\nu\beta\beta$ of ^{48}Ca.

Table 5.2: Parameter for $0\nu\beta\beta$ sensitivity estimation with improved efficiency about 0 background measurement. The Feldman-Cousins rule [29] is used to calculate μ.

M	T	a	N_{A}	ϵ	W	μ
305.28 kg	1 yr	1.87×10^{-3}	6.02×10^{23} /mol	0.7	0.07807 kg/mol	2.44

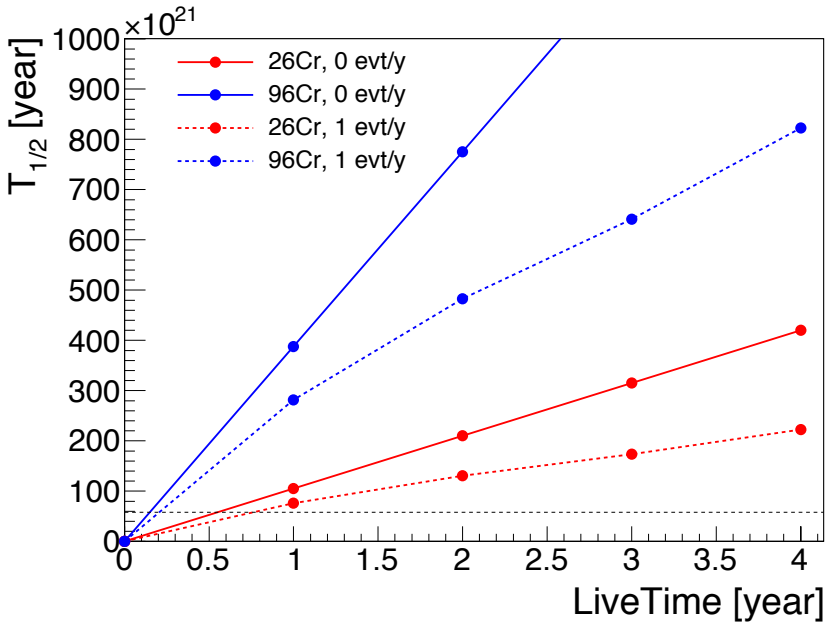

Figure 5.6: Expected sensitivity as upper limit of $T^{0\nu}_{1/2}(^{48}\mathrm{Ca})$. Two colored solid lines (red: 26 crystals, blue: 96 crystals) show estimated values on zero background measurement. Two colored dashed lines show values on 1 events / year measurement. Then the ditection efficiency ϵ is set to 0.3. Black dashed line shows ELEGANT VI sensitivity.

Chapter 6

Conclusion

Observation of neutrinoless double beta decay is an extremely interesting research because it demonstrates lepton number violation and Majorana nature. These theories are beyond the Standard Model and $0\nu\beta\beta$ will be a signal of new physics. We perform the CANDLES experiment to search for $0\nu\beta\beta$ of ^{48}Ca at the Kamioka underground laboratory.

The purpose of the study is to show origins of backgrounds in the energy region around $Q_{\beta\beta}$ (4.27 MeV) and to estimate the amount of backgrounds. In $Q_{\beta\beta}$ region, Th-chain backgrounds are expected and can be identified by analysis improvement. However, we observed unexpected backgrounds with a characteristic structure in the high energy region above $Q_{\beta\beta}$. The amount of total observed events in the energy region from 4.16 MeV to 4.48 MeV with total exposure of 5043 kg $\cdot$ days is 6 events. This corresponds to 0.8×10^{22} yr of the detector sensitivity as the lower limit on the half-life of ^{48}Ca $0\nu\beta\beta$. This result has not reached the world best sensitivity of ^{48}Ca $0\nu\beta\beta$ up to date due to backgrounds.

For improvement of the sensitivity, finding the origin of these unexpected backgrounds was necessary. From the characteristic structure of observed energy spectrum, we assumed that γ-ray from (n,γ) reactions of the detector tank and the rock wall could be the origin of high energy backgrounds. In order to verify the hypothesis, we performed neutron source run to generate (n,γ) reaction artificially. As a result, we found that main backgrounds in $Q_{\beta\beta}$ region are γ-rays from neutron capture reactions at surrounding materials of the detector. In addition, the ratio of the (n,γ) background components Rock : Tank in $Q_{\beta\beta}$ region was estimated as about 7 : 3, which means that we should consider about

shielding against γ-rays from both materials.

In conclusion, in order to achieve the best sensitivity, additional shields for neutron and γ-ray which are scheduled to be installed have been discussed. As a result, we have planned to install $\sim$ 10 cm Pb block and 5 mm B-containing sheet as additional shieldings and expected that (n,γ) backgrounds will be reduced to less than 1 events / year. We aim to reduce total background to less than 1 event / year at $Q_{\beta\beta}$ region and to achieve the most stringent experimental limit for $0\nu\beta\beta$ of ^{48}Ca with 1 $\sim$ 2 years measurement.

Acknowledgement

The author's deepest appreciation goes to Professor T. Kishimoto for his valuable discussions, suggestions for interpretations on observations and very kind encouragement. He has provided the author with knowledge on physics, scientific thinking and the others. His teachings have been very helpful for author's research.

The author would like to express his gratitude to Professor M. Nomachi for his piercing advice and powerful discussions especially for effect of additional shieldings. The author would also like to express his gratitude to Professor S. Yoshida for his powerful leading, discussions and helpful advice for writing and presentation. The author is also deeply grateful to Dr S. Umehara for permission to refer to her great works in data analysis and helpful advice. The author is also deeply grateful to Dr K. Nakajima for permission to refer to his great works especially in Monte-Carlo simulation, kind advice and helpful discussions. The author is also deeply grateful to Dr T. Iida for his collaborations in measurement and analysis, kind advice and encouragement. The author is also deeply greatful to Dr K. suzuki for his advice about handling the experimental system and kind encouragement. The author is also deeply greatful to Dr K. Ichimura in Tokyo Univ. for his great works in analysis and helpful collaboration.

The author also thanks Professor I. Ogawa in Univ. of Fukui, Professor K. Fushimi in Univ. of Tokushima and Professor R. Hazama in Osaka Sangyo Univ. for their kind advice and encouragement. The author also thanks K. Matsuoka and N. Nakatani in Osaka Sangyo Univ. for their technical advice about hardware and helpful collaborations.

The author is also deeply indebted to W. M. Chan, V. T. T. Trang, T. Ohata, K. Tetsuno, T. Maeda, T. Uehara, X. Li and B. Temuge for permission to refer to their outstanding works, reliable discussions, kind advice, analytical collaborations and being my delightful acquaintances. They has provided the author with

meaningful information for analysis, strong manpower and vitality for study! The auther is deeply indebted to grate achievement of graduates, G. Ito, K. Yasuda, M. Saka, M. Doihara, D. Tanaka, T. Ishikawa and M. Tanaka. The author is also deeply indebted to all other members of the CANDLES collaboration and the Kishimoto group.

The author would also like to express my gratitude to my family for their moral support and warm encouragements.

The author could accomplish his work with their supports and encouragement.

Bibliography

[1] Kai Zuber, *Neutrino Physics, Second Edition*. CRC Press.

[2] D.V.Forero, M.Tórtola, and J.W.F.Valle, *Global status of neutrino oscillation parameters after Neutrino-2012*. Phys. Rev. D 86, 073012.

[3] C. Aalseth et al., APS Neutrino Study (2004)

[4] *Fundamental Physics at the Intensity Frontier*, Report of the Workshop held December 2011 in Rockville, MD, ANL-HEP-TR-12-25 SLAC-R-991.

[5] M.Gell-Mann, P.Ramond, and R.Slansky, *Supergravity* ed. by D. Freedman and P. Van Nieuwenhuizen, North Holland, Amsterdam (1979), pp. 315-321.

[6] C.F. von Weizäcker, *Tur Theorie der Kernmassen*, Z. Phys. 96 (1935) 431-458.

[7] S.R.Elliot and P.Vogel, *DOUBLE BETA DECAY*. Ann. Rev. Nucl. Part. Sci. 52(2002)115.

[8] Bernhard Schwingenheuer, *Status and prospects of searches for neutrinoless double beta decay*. Annalen Phys. 525 (2013) 269-280.

[9] Joseph A. Formaggio and C.J. Martoff, *BACKGROUNDS TO SENSITIVE EXPERIMENTS UNDERGROUND*. Ann. Rev. Nucl. Part. Sci. 54(2004)361-412.

[10] H.V.Klapdor-Kleingrothaus and I.V.Krivosheina, *THE EVIDENCE FOR THE OBSERVATION OF* $0\nu\beta\beta$ *DECAY: THE IDENTIFICATION OF*

$0\nu\beta\beta$ *EVENTS FROM THE FULL SPECTRA*. Mod. Phys. Lett. A21(2006)1547-1566.

[11] M. Agostini et al., *Results on Neutrinoless Double-β Decay of ^{76}Ge from Phase I of the GERDA Experiment*. Phys. Rev. Lett. 111(2013)122503.

[12] A. Gando et al., *Measurement of the double-β decay half-life of ^{136}Xe with the KamLAND-Zen experiment*. Phys. Rev. C 85, 045504.

[13] M. Auger et al., *Search for Neutrinoless Double-Beta Decay in ^{136}Xe with EXO-200*. Phys. Rev. Lett. 109(2012)032505.

[14] Richard B. Firestone, Virginia S. Shirley et al., *Table of Isotopes, EIGHTS EDITION*. John Wiley & Sons, Inc., 1996.

[15] K. J. R. Rosman and P. D. P. Taylor, *Isotopic compositions of the elements 1997 (Technical Report)*. Pure & Appl. Chern. 71 No. 1(1998)217-235.

[16] I. Ogawa et al., *Search for neutrino-less double beta decay of ^{48}Ca by CaF_2 scintillator*. Nuclear Physics A730(2004)215-223.

[17] S. Umehara et al., *Neutrino-less double β decay of ^{48}Ca studied by CaF_2(Eu) scintillators*. Phys. Rev. C 78, 058501(2008).

[18] S. Umehara, Doctral thesis, Osaka University(2004).

[19] S. Yoshida et al., *Ultra-violet wavelength shift for undoped CaF_2 scintillation detector by two phase of liquid scintillator system in CANDLES*. NIMA 601(2009) 282.

[20] Y.Hirano, Doctral thesis, Osaka University(2008).

[21] M. J. Dolinski, Doctral thesis, University of California, Berkeley(2008).

[22] Database of Prompt Gamma Rays from Slow Neutron Capture for Elemental Analysis IAEA,VIENNA.

[23] T. Ishikawa, Master thesis, Osaka University(2014).

[24] *α activity of natural tungsten isotopes*. Phys. Rev. C 67, 014310(2003).

[25] E. Gatti and F. De Martini, *A new linear method of discrimination between elementary particles in scintillation counters, Nuclear Electronics* vol.2, pp. 265-276, IAEA Wien(1962).

[26] S. Umehara et al., *CANDLES -Search for neutrino-less double beta decay of* ^{48}Ca. EPJ Web of Conferences 66, 08008 (2014).

[27] Alfred Tang, Glenn Horton-Smith et al., *Muon simulations for Super-Kamiokande, KamLAND, AND CHOOZ*. Phys. Rev. D 74, 053007(2006).

[28] Japanese Industrial Standards., *Hot-rolled stainless steel plate, sheet and strip*. JIS G 4304:2012.

[29] Gary J. Feldman and Robert D. Cousins, *Unified approach to the classical statistical analysis of small signals*. Phys. Rev. D 57, 3873(1998).

[30] K.A. Olive et al. (Particle Data Group), Chin. Phys. C, 38, 090001 (2014).

[31] A. Minamino, Master thesis, Tokyo University(2004).

[32] K. Nakajima for the CANDLES Collaboration., Poster presentation at "DBD2014" (Oct. 2014).

[33] J. H. Hubbell and S. M. Seltzer, *Tables of X-Ray Mass Attenuation Coefficients and Mass Energy-Absorption Coefficients from 1 keV to 20 MeV for Elements Z = 1 to 92 and 48 Additional Substances of Dosimetric Interest*. NISTIR 5632 (http://www.nist.gov/).

[34] K. Nakajima, S. Yoshida for the CANDLES Collaboration., Oral presentation at JPS (Mar. 2015).

[35] K. Shibata, T. Kawano et al., *Japanese Evaluated Nuclear Data Library Version 3 Revision-3: JENDL-3.3*. J. Nucl. Sci. Technol. 39, 1125(2002).

[36] V. B. Mikhailik et al., Nucl. Instr. and Meth. A566 (2006) p522.

[37] M. Doihara, Master thesis, Osaka University(2014).